

UC San Diego

UC San Diego Electronic Theses and Dissertations

Title

Engineering and screening dynamic behaviors in microbial populations

Permalink

<https://escholarship.org/uc/item/02129404>

Author

Lezia, Andrew

Publication Date

2023

Supplemental Material

<https://escholarship.org/uc/item/02129404#supplemental>

Peer reviewed|Thesis/dissertation

UNIVERSITY OF CALIFORNIA SAN DIEGO

Engineering and screening dynamic behaviors in microbial populations

A dissertation submitted in partial satisfaction of the
requirements for the degree
Doctor of Philosophy

in

Bioengineering

by

Andrew Robert Lezia

Committee in charge:

Professor Jeff Hasty, Chair
Professor Stephanie Fraley
Professor Nan Hao
Professor Justin Meyer
Professor Kun Zhang

2023

Copyright
Andrew Robert Lezia, 2023
All rights reserved.

The dissertation of Andrew Robert Lezia is approved, and it is acceptable in quality and form for publication on microfilm and electronically.

University of California San Diego

2023

DEDICATION

To my parents who have always supported me.

EPIGRAPH

Somewhere, something incredible is waiting to be known.

—Carl Sagan

Unclose your mind. You are not a prisoner. You are a bird in flight, searching the skies for dreams.

—Haruki Murakami, Hard-Boiled Wonderland and the End of the World

TABLE OF CONTENTS

Dissertation Approval Page	iii
Dedication	iv
Epigraph	iv
Table of Contents	vi
List of Figures	x
List of Tables	xii
Acknowledgments	xiii
Vita	xv
Abstract of the Dissertation	xvi
Chapter 1	
Introduction	1
1.1 Synthetic Biology and Dissertation Overview	1
1.2 Dissertation Themes	4
1.2.1 Engineered Living Cell Therapies	4
1.2.2 Microfluidics for Studying Cellular Dynamics	7
1.2.3 Coordination of Microbial Populations	8
1.2.4 Host-Circuit Interactions	9
1.2.5 Improved Circuit Stability	9
1.2.6 Exploiting Cellular Heterogeneity	10
1.2.7 Library Creation and Screening for Genetic Circuits	11
1.2.8 Genetic Part Creation and Modular Cloning Toolkits	11
1.3 Acknowledgments	14
Chapter 2	
Design, mutate, screen: Multiplexed creation and arrayed screening of synchronized genetic clocks	15
2.1 Abstract	15
2.2 Introduction	16
2.3 Results	20
2.3.1 Overview of directed evolution approach for synthetic oscillator creation and tuning	20
2.3.2 Tuning the oscillatory dynamics of a synchronized lysis circuit by directed mutagenesis	21
2.3.3 Creation of a transcriptionally-regulated synchronized gene oscillator circuit via directed mutagenesis and screening	27

2.4	Discussion	34
2.5	Supplemental Figures	36
2.6	Materials and Methods	41
2.6.1	Cloning and library creation for SLC strains	41
2.6.2	Microfluidic device development and fabrication	42
2.6.3	Multi-strain Microfluidic experimental protocol	42
2.6.4	AHL induction protocol in SLC microfluidic experiments	43
2.6.5	Live-cell imaging and data extraction for SLC library experiments	44
2.6.6	Generation of lysis dose-response curves	46
2.6.7	Calculation of damping coefficients	46
2.6.8	Peak detection for comparison of P2N1-Tet strains	47
2.6.9	Data analysis of multi-strain microfluidic transmitted-light image stacks	47
2.6.10	Analysis of single strain microfluidic data	47
2.6.11	Theoretical RBS translation rate prediction with RBS Calculator 2.0	48
2.6.12	Experimental characterization of selected RBS sequences in constitutive GFP expressing circuit	48
2.6.13	Deterministic modeling of Synchronized Lysis Circuit dynamics	49
2.6.14	Deterministic modeling of tetR-GFP Synchronized Oscillator dynamics	50
2.7	Supplementary Videos	51
2.7.1	Supplementary Video 2.1 (related to Figure 2.4)	51
2.7.2	Supplementary Video 2.2 (related to Figure 2.4)	52
2.7.3	Supplementary Video 2.3 (related to Figure 2.6)	52
2.8	Acknowledgments	52
Chapter 3	Screening of therapeutic libraries for cancer cell toxicity using synchronized cell lysis and developing regulation to increase lysis circuit stability	53
3.1	Abstract	53
3.2	Introduction	54
3.3	Results	55
3.3.1	Construction of Therapy Library	55
3.3.2	Confirming lysis dynamics of different therapeutic strains	56
3.3.3	Establishing a 3D co-culture screening platform	59
3.3.4	Library screening results	61
3.3.5	Development of a repressible synchronized lysis circuit for improved growth stability in batch culture	62
3.4	Discussion	66
3.5	Materials and Methods	70
3.5.1	Construction of lysis circuit toxin library	70
3.5.2	Microfluidic culture of lysis circuit toxin library strains	70

	3.5.3	3D HeLa Cell Culture in Fibrin Matrix	70
	3.5.4	Bacteria HeLa Co-Culture and 3D Cell-Titer Glo Screening Assay	71
	3.5.5	Plate reader experiments to test lysis circuit function	72
	3.6	Acknowledgments	72
Chapter 4		Exploiting heterogeneity in coupled, two plasmid systems for dynamic population adaptation	73
	4.1	Abstract	73
	4.2	Introduction	74
	4.3	Results	76
	4.3.1	Duplicate origin plasmid pairs generate population heterogeneity and enable environmental adaptation	76
	4.3.2	Duplicate ori systems enable burden minimization and can increase plasmid stability due to buffering by non-essential plasmids	79
	4.3.3	Minimal sister plasmid provides copy number flexibility and evidence of population memory	84
	4.3.4	Redundant ori plasmid systems promote generational population memory in response to engineered cell lysis in microfluidic culture.	87
	4.3.5	Engineered plasmid incompatibility enables coupled copy number tuning in two plasmid systems	90
	4.4	Supplemental Figures	95
	4.5	Materials and Methods	101
	4.5.1	Strains and plasmids	101
	4.5.2	Plate reader experiments for estimating average copy number in batch culture using fluorescence	102
	4.5.3	Agarose pad slide preparation for single-cell imaging and analysis	102
	4.5.4	Quantitative PCR for determination of average copy number	103
	4.5.5	Microfluidics and microscopy for carbon-source operon strains in multi-strain device	103
	4.5.6	Serial passaging and plating experiment to estimate plasmid loss rate for carbon-source operon strains	103
	4.5.7	Serial passaging and plating experiment to estimate population fraction of duplicate versus single carbon-source operon strains in competition	104
	4.5.8	Serial passaging and memory quantification of inducible Kan strains in plate reader	105
	4.5.9	Microfluidics and microscopy for inducible lysis strains in concentration gradient device	105

4.5.10	Image analysis of inducible lysis strain timelapse microscopy experiments	105
4.5.11	Microfluidics and microscopy for inducible lysis strains in multi-strain device	106
4.5.12	Plasmid Copy Number Model	106
4.6	Supplementary Videos	108
4.6.1	Supplementary Video 4.1	108
4.7	Acknowledgments	108
Chapter 5	A standardized set of MoClo-compatible inducible promoter systems for tunable gene expression in yeast	109
5.1	Abstract	109
5.2	Introduction	110
5.3	Results	113
5.3.1	A Modular Cloning Framework for Constructing Standardized Inducible Systems	113
5.3.2	Doxycycline Inducible Systems with Advanced rtTA Variants	116
5.3.3	ABA Inducible Systems based on ABI and PYL1 Heterodimerization	120
5.3.4	ASV and GZV Inducible Systems based on Controllable NS3 Proteolytic Cleavage	123
5.3.5	Multiple Cloning Site Plasmids for Rapid and Customizable use of Inducible Systems	126
5.4	Discussion	127
5.5	Supplemental Figures	128
5.6	Methods	135
5.6.1	Yeast Strains and Transformations	135
5.6.2	Golden Gate Assembly Protocol	136
5.6.3	Construction of Parts and Plasmids.	136
5.6.4	Characterization of Inducible Promoters	137
5.6.5	Analysis of Induction Curves	138
5.6.6	Creation of Inducible System Integration Plasmids with Multiple Cloning Site	139
5.7	Acknowledgments	140
Bibliography	141

LIST OF FIGURES

Figure 1.1:	Overarching themes of the dissertation.	3
Figure 1.2:	Connection of each chapter to overarching dissertation themes.	3
Figure 1.3:	Progressive Advancements in the Synchronized Lysis Circuit (SLC)	7
Figure 1.4:	Overview of Modular Cloning Workflow via Golden Gate Assembly.	13
Figure 2.1:	Synthetic oscillator creation and tuning through directed mutagenesis and screening.	19
Figure 2.2:	A multi-strain microfluidic device for dynamic phenotype screening.	21
Figure 2.3:	Screening of Synchronized Lysis Circuit (SLC) library strains.	23
Figure 2.4:	Comparison of SLC library strains with varying lysis strengths reveals differences in gene expression dynamics.	25
Figure 2.5:	Comparison between P2N1-Tet and P2N2-Tet Circuit Topologies	29
Figure 2.6:	Optimizing a synchronized genetic oscillator via directed mutagenesis and screening.	33
Figure 2.7:	Modeling the effects of exogenous AHL and lysis Gene RBS strength on SLC oscillatory dynamics (Supplementary data related to Figures 2.3 and 2.4)	37
Figure 2.8:	Analysis of P2N2-Tet Oscillator Circuit Design (Supplementary data related to Figure 2.5)	38
Figure 2.9:	Analysis of P2N2-Tet Design (Supplementary data related to Figures 2.5 and 2.6)	39
Figure 2.10:	Plasmids Used in this Study and Sequenced RBS Variants (Supplementary data related to Figures 2.4 and 2.6 (and throughout))	40
Figure 3.1:	SLC therapy library construction pipeline.	57
Figure 3.2:	Batch culture screening of therapy library lysis dynamics.	58
Figure 3.3:	SLC therapy library strain dynamics in a microfluidic device.	60
Figure 3.4:	SLC therapy library co-culture screening results	63
Figure 3.5:	Characterization of hybrid pLuxTet promoter.	64
Figure 3.6:	Characterization of a TetR-repressible lysis circuit in batch culture.	65
Figure 3.7:	Control of lysis circuit repression with arabinose inducible TetR expression.	67
Figure 3.8:	Improved lysis circuit stability with arabinose-based system.	68
Figure 4.1:	Chapter 4 Graphical Abstract	75
Figure 4.2:	Two plasmid systems with redundant oris show increased heterogeneity and adaptability.	78
Figure 4.3:	Duplicate origin plasmids allow burden-based adaptation to different nutrient environments and improve plasmid stability.	83
Figure 4.4:	Incompatible “sister” plasmid buffering enables sensitive population adaptation and promotes long-term memory.	86
Figure 4.5:	Inducible cell lysis triggers population CN shifting in duplicate ori systems.	89

Figure 4.6:	Engineered plasmid incompatibility enables coupled copy number tuning in two plasmid systems.	91
Figure 4.7:	Diagram of plasmid copy number model	96
Figure 4.8:	Supplementary material related to Figure 4.3.	97
Figure 4.9:	Supplementary material related to Figure 4.4.	98
Figure 4.10:	Supplementary material related to Figure 4.5.	99
Figure 4.11:	Supplementary material related to Figure 4.5.	100
Figure 4.12:	Supplementary material related to Figure 4.5.	101
Figure 5.1:	Workflow for developing yTEST.	114
Figure 5.2:	Parts included in yTEST.	116
Figure 5.3:	Design and induction properties of rtTA Dox inducible systems.	119
Figure 5.4:	Design and induction properties of ABA inducible systems.	122
Figure 5.5:	Design and induction properties of NS3 inducible system.	124
Figure 5.6:	Construction and validation of MCS inducible system integration plasmids.	126
Figure 5.7:	Comparison of advanced rtTA variants used in the yTEST kit.	129
Figure 5.8:	Constitutive promoter Characterization	130
Figure 5.9:	Design of activation domains.	131
Figure 5.10:	Core components of the NS3 protease sequence.	131
Figure 5.11:	Multiple-cloning site (MCS) plasmids	132
Figure 5.12:	Background BY4741 strain growth vs. inducer concentration.	133
Figure 5.13:	Background BY4741 strain fluorescence vs. inducer concentration.	134

LIST OF TABLES

Table 3.1:	Therapeutic genes with their origin, function, and citation	56
Table 4.1:	Bacterial strains used in chapter 4	95
Table 4.2:	Plasmids used in chapter 4	98
Table 4.3:	Primer sequences for qPCR	99

ACKNOWLEDGMENTS

The research in this dissertation would not be possible without the enormous amount of support I've received in and outside of the Biodynamics Lab. First, I want to thank my loving parents. The unwavering support they've given me throughout my life is the cornerstone of my academic success. I want to thank Connor and Dan for being the best homies I could ask for. I want to thank my fiancée, Jacquie, who was always by my side throughout grad school. Your support means everything to me.

I'm extremely grateful for all of the people I've gotten the opportunity to work with in the Biodynamics lab. I want to thank Omar Din, one of the first members of the lab who mentored me. Our many conversations about biology and genetic circuits have always inspired me.

I'm especially grateful for the mentorship and support I received from Nick Csicsery. Collaborating with Nick was one of the true highlights of my PhD experience and my friendship with Nick has made me a better scientist and given me more confidence in myself.

I want to thank Shalni Kumar for working with me and believing in our project. Getting to come up with new ideas and experiments together has been one of the highlights of my scientific career. Thank you for trusting in the power of heterogeneity and duplicate origins.

I want to thank Ricky O'Laughlin and Quoc Tran for getting me involved in their yeast synthetic biology projects. I learned so much from both of them.

Lastly, I want to thank my advisor, Jeff. He has always had genuine confidence in my ability as a scientist even when I didn't. The support Jeff gave me through the highs of grad school and the lowest lows were essential to my success. Thank you, Jeff.

Chapter 1 contains excerpts from a review article originally published as: Lezia, Andrew*, Miano, Arianna*, and Hasty, Jeff. "Synthetic Gene Circuits: Design, implement, and apply" *Proceedings of the IEEE* 110, no. 5 (2021): 613-630. (*equal contribution) The dissertation author was one of the primary authors and researchers of this material.

Chapter 2 contains material originally published as: Lezia, Andrew*, Csicsery, Nicholas*,

and Hasty, Jeff. "Design, mutate, screen: Multiplexed creation and arrayed screening of synchronized genetic clocks." *Cell Systems* 13, no. 5 (2022): 365-375. (*equal contribution) The dissertation author was one of the primary authors and researchers of this material.

Chapter 3 contains unpublished material in preparation for publication as: M. Omar Din*, Andrew Lezia*, and Jeff, Hasty. "Screening of bacterial cancer therapy libraries in 3D co-culture" (*equal contribution) The dissertation author was one of the primary authors and researchers of this material.

Chapter 4 contains material being prepared for submission as: Lezia, Andrew*, Kumar, Shalni*, and Hasty, Jeff. "Burden-minimizing Adaptation of Populations with Duplicate Origin Plasmid Pairs". (*equal contribution) The dissertation author was one of the primary authors and researchers of this material.

Chapter 5 contains material submitted for publication at ACS Synthetic Biology as: O'Laughlin, Ricky*, Tran, Quoc*, Lezia, Andrew*, and Hasty Jeff. "A standardized set of MoClo-compatible inducible promoter systems for tunable gene expression in yeast" (*equal contribution)

VITA

- 2017 B.S. in Biomedical Engineering *summa cum laude*, Washington University
in St. Louis
- 2023 Ph.D. in Bioengineering, University of California San Diego

PUBLICATIONS

Andrew Lezia*, Nicholas Csicsery*, and Jeff Hasty. “Design, mutate, screen: Multiplexed creation and arrayed screening of synchronized genetic clocks.” *Cell Systems* (2022) (*equal contribution).

Andrew Lezia*, Arianna Miano*, and Jeff Hasty. “Synthetic Gene Circuits: Design, Implement, and Apply.” *Proceedings of the IEEE* (2021) (*equal contribution).

Venktesh S Shirure, Ye Bi, Matthew B Curtis, Andrew Lezia, Madeleine M Goedegebuure, S Peter Goedegebuure, Rebecca Aft, Ryan C Fields, and Steven C George. “Tumor-on-a-chip platform to investigate progression and drug sensitivity in cell lines and patient-derived organoids.” *Lab on a chip* (2018)

Venktesh S Shirure, Andrew Lezia, Arnold Tao, Luis F Alonzo, and Steven C George. “Low levels of physiological interstitial flow eliminate morphogen gradients and guide angiogenesis.” *Angiogenesis*. (2017)

ABSTRACT OF THE DISSERTATION

Engineering and screening dynamic behaviors in microbial populations

by

Andrew Robert Lezia

Doctor of Philosophy in Bioengineering

University of California San Diego, 2023

Professor Jeff Hasty, Chair

Engineering novel, biological functions with synthetic genetic circuits is easier than ever before due to constant discovery of new genetic parts, development of efficient ways to put those parts together, and innovative methods to model and study complex phenotypes. As the field of Synthetic Biology continues to grow, different focus areas and challenges have come to light. In this dissertation, I identify key themes and current challenges in Synthetic Biology and use novel circuit design and screening approaches to build on existing research in these areas. One growing area of focus is controlling and coordinating microbial behavior at the population level. A major challenge in this area is screening dynamic, population-level circuits for desired behavior with the same throughput as single-cell circuit screening methods. Chapter 2 of this

dissertation introduces a novel microfluidic device that enables screening of mutant bacterial libraries for complex, population-level phenotypes that change with time. Chapter 3 focuses on genetic circuit screening as well, but from a more application-based standpoint. Specifically, a workflow is developed for screening bacterial expressed toxins for their ability to inhibit cancer cell growth when released via engineered bacterial cell lysis. Novel candidates are uncovered for bacterial-based cell therapies. While noise and heterogeneity are typically avoided in synthetic biology, Chapter 4 presents a novel strategy for exploiting engineered heterogeneity in bacterial populations to enable the populations to quickly adapt to varying environments. Chapter 5 addresses the need for new, quantitatively-characterized inducible promoter systems in yeast. The systems developed in this chapter are designed to be compatible with existing modular cloning toolkits in yeast, making their implementation simple and standardized. Together, the results presented in this dissertation demonstrate novel strategies for controlling population-level behavior in bacteria, screening genetic circuits for complex phenotypes, and creating new genetic parts for circuit regulation.

Chapter 1

Introduction

1.1 Synthetic Biology and Dissertation Overview

Over a few billion years life has evolved solutions to problems at the limit of human comprehension. In this period, natural selection has driven the emergence of innumerable molecular machines in the form of proteins and ribonucleic acids (RNA) that facilitate diverse chemical reactions with astounding specificity and efficiency. Equally as fascinating as nature's endless tool box are the complex networks that these tools operate within, which span individual molecular pathways to entire ecosystems. Until relatively recently, this breadth of parts and devices seemed impervious to human tinkering, shrouded in the complexity of the parts themselves as well as their encompassing networks. In the last 100 years or so, human innovation and research has cleared much of this fog of complexity allowing us to see biological systems not as magic, but as decomposable and comprehensible networks. In addition to uncovering the basic flow of information at the molecular level, researchers have identified many small motifs of genetic interactions that occur much more often than random and contribute to massive biological networks [1]. This relatively newfound understanding of biological networks and their components has grown at a rapid pace leading to researchers constructing their own synthetic

gene circuits over the last 20 years [2–4].

The first synthetic gene networks mimicked simple electronic circuits and showed that biological systems could be created with a bottom-up design approach centered around principles like abstraction and modularity typically seen in traditional engineering fields [5, 6]. While these initial forays into synthetic gene circuits helped shine a light on the fact that biological systems could be engineered, they also brought into focus a slew of characteristics that kept biology distinct from engineering including the stochasticity of gene expression and context-dependent behavior of genetic parts. Now, the field of synthetic biology is in its adolescence, with a multitude of engineered circuits leaving the lab to solve real-world problems.

The growth of synthetic biology has led to the emergence of several prominent focus areas. The forthcoming chapters in this dissertation highlight projects that are directly and indirectly connected through common themes. For example, Chapter 2 directly links to other chapters by detailing the development of a microfluidic cell culture device that is then used elsewhere. In contrast, Chapters 2 and 4 share an indirect connection, as they both describe approaches to engineering population-level behavior in bacteria. Figure 1.1 illustrates the significant synthetic biology topics explored in this dissertation, while Figure 1.2 shows the correlation of each chapter to each synthetic biology topic. In the following sections, I provide a brief overview of each topic area and its relevance to the dissertation chapters. To start, I present work from the Biodynamics Lab on the Synchronized Lysis Circuit (SLC) and how it has been improved and utilized for cancer therapy. This serves as an example of how iterative design and basic research can lead to genetic circuits with real-world relevance.

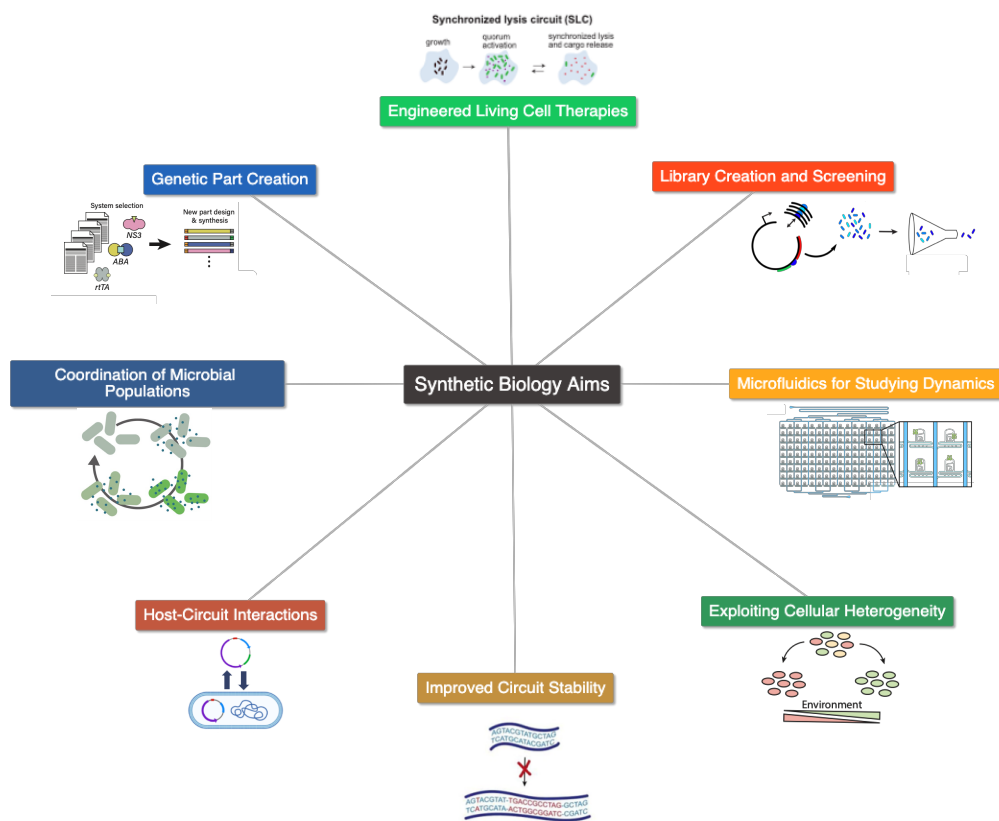


Figure 1.1: Overarching themes of the dissertation.

	Chapter 2: Design, mutate, screen: Multiplexed creation and arrayed screening of synchronized genetic clocks	Chapter 3: Screening of therapeutic libraries for cancer cell toxicity using synchronized cell lysis	Chapter 4: Exploiting heterogeneity in coupled, two plasmid systems for dynamic population adaptation	Chapter 5: A standardized set of MoClo-compatible inducible promoter systems for tunable gene expression in yeast
Microfluidics for studying dynamics	X	X	X	
Exploiting Cellular Heterogeneity			X	
Coordination of Microbial Populations	X		X	
Library Creation and Screening	X	X		X
Host-circuit interactions		X	X	
Engineered Living Cell Therapies		X		
Genetic Part Creation	X	X	X	X
Improved Circuit Stability		X	X	

Figure 1.2: Connection of each chapter to overarching dissertation themes.

1.2 Dissertation Themes

1.2.1 Engineered Living Cell Therapies

Compared to traditional, chemical-based therapeutics for disease, therapies made from and delivered by engineered living organisms offer many advantages due to their potential for dynamic, environment-specific behavior. For instance, if we consider a system with two states, diseased and healthy, synthetic gene circuits can enable an engineered cell to distinguish between these two states and activate a specific program of gene expression depending on the state, much like a computer [7]. Here, I describe work from our group and others on using engineered bacteria for cancer therapy that demonstrates: 1) Why bacteria may be good vehicles for delivering therapy to solid tumors, 2) How synthetic gene circuits can be used to dynamically control the release of a therapeutic as well as the size of the bacterial population delivering the therapy, and 3) How additional circuitry could help solve challenges related to gene circuit stability and exogenous control of therapeutic release.

The identification of tumor-colonizing bacteria and their potential anti-tumor effects dates back over a century [8], and recent research has further reinforced the observation that many different types of bacteria can colonize and grow within a range of solid tumor types [9–12]. Given this abundance of research on the ability of bacteria to colonize solid tumors and challenges associated with some chemotherapeutics penetrating into solid tumors, multiple groups identified the potential for bacteria to be used as vehicles for therapy-delivery.

One system was recently developed that enables bacteria to release different therapeutic payloads within tumors while preventing unchecked growth of the bacterial population (Figure 1.3A). This system, the Synchronized Lysis Circuit (SLC), utilizes a naturally occurring bacterial phenomenon, quorum sensing (QS), to synchronize therapeutic production and release from a tumor-colonizing population of bacteria [13]. Specifically, the circuit consists of three primary genes: 1) an N-Acyl homoserine lactone (AHL) synthase, LuxI, 2) a lysis gene derived from

a phage, and 3) a gene encoding an anti-cancer therapeutic. Each of these genes is driven by the pLux promoter, which is activated by the AHL-LuxR transcription factor complex. At low population levels, cells produce low levels of AHL due to leaky expression from the pLux promoter. AHL is free to diffuse among the cells and, as the population grows, the local concentration of AHL increases in proportion to the number of cells. Once the population size reaches a quorum threshold size, AHL concentrations become sufficient to fully activate the pLux promoter via LuxI-mediated positive feedback, which leads to significant production of the lysis gene and a therapy gene. Production of the lysis gene causes the majority of cells in the population to lyse and release the therapy molecule while the few remaining cells are able to grow up again perpetuating cycles of growth, therapy production, and lysis.

As this mechanism of delivery relies on bacteria lysing and releasing their intracellular contents, it is readily amenable to releasing diverse types of therapeutic molecules as potentially difficult to engineer secretion mechanisms are unnecessary. Additionally, since this circuit regularly culls the bacterial population size, it addresses some of the major safety concerns associated with containment of engineered therapeutics. Since its original development, the SLC has been utilized to deliver nanobodies targeting an anti-phagocytotic receptor that is commonly overexpressed in cancer [14] as well as immune checkpoint-inhibiting nanobodies [15].

While the initial design of the SLC has proven success expressing different types of therapeutics in mouse models, there are multiple challenges associated with this approach including the propensity of the lysis circuit to mutate over time and the lack of exogenous control over the lysis circuit behavior. To address stability issues of the SLC and extend its functional lifetime, Liao et. al. recently developed new genetic circuitry across multiple engineered strains of bacteria [16](Figure 1.3). In this rock-paper-scissors (RPS) circuit, three strains of *E. coli* are engineered to each express a unique bacterial toxin known as a colicin. Each strain is also designed to express immunity to two out of the three colicins in the circuit, while remaining susceptible to the third colicin. This creates a simple network of interactions where three strains

can be cycled by sequentially introducing a strain that kills the previous strain. This circuit was used to extend the functional lifetime of the SLC by introducing a copy of the SLC into each strain making up the RPS circuit. As soon as the SLC becomes non-functional in one strain due to mutation, this strain can be replaced by the next strain in the RPS circuit and so on and so forth, allowing the SLC to function over much longer time scales than possible in a single strain alone. While this RPS circuitry has yet to be applied with the SLC *in vivo*, it represents a promising strategy for extending the lifetime of genetic circuits in real-world applications.

In another advancement on the original SLC circuitry, Miano et. al. recently developed a mechanism to control the dynamics of the SLC using an external inducer molecule [17](Figure 1.3). This circuit, the inducible SLC (iSLC), makes use of the quorum sensing machinery from the photosynthetic bacterium *Rhodospseudomonas palustris*, which relies on the external, plant-derived inducer molecule, p-coumaric acid (pCA) to produce its quorum sensing molecule, p-coumaroyl-HSL (pC-HSL). When this pCA-inducible QS system was used for the SLC instead of the original Lux system, the dynamic behaviour of the SLC could be controlled in one of three different states depending on the concentration of pCA. For low pCA concentrations, insufficient pC-HSL is produced to activate lysis and the population grows normally. For intermediate levels of pCA, the SLC functions as described previously, with synchronized cycles of growth, therapy production, and lysis. Lastly, for high pCA concentrations, the circuit acts as a kill switch, with lysis protein production high enough to prevent significant growth of the population. The ability to control the dynamics of an engineered therapy strain with a non-toxic inducer like pCA, along with the kill-switch control capability to quickly eliminate the engineered strain with high levels of pCA, make this circuit a promising strategy for bacterial-based cancer therapeutics.

Chapter 2 of this dissertation builds on advancements in controlling and stabilizing the SLC by screening mutant variant libraries of this circuit for versions with different dynamical properties. Chapter 3 demonstrates how the lysis circuit can be used to rapidly test a library of potential therapeutic genes for their ability to kill cancer cells in a 3D co-culture model.

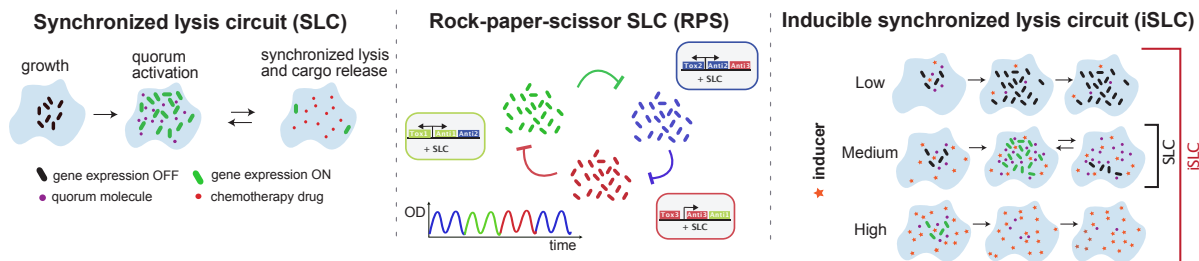


Figure 1.3: Advancements in the Synchronized Lysis Circuit (SLC). Top left panel shows the behavior of the synchronized lysis circuit (SLC) which can deliver bursts of therapy payload release in an oscillatory fashion [13]. The following panel shows a synthetic community of three populations which can kill each-other with toxins in a rock-paper-scissor pattern [16]. Each population is also equipped with the SLC for cargo release. The last panel shows an inducible synchronized lysis circuit which has different dynamics as a function of inducer concentration [17].

1.2.2 Microfluidics for Studying Cellular Dynamics

As the behaviors researchers wish to endow cells with become more complex, they become more difficult to study and observe. Technology developments now allow different types of cells to be grown in precisely controlled spatio-temporal environments perfused by microliters of culture media. These microfluidic devices now have countless lab-on-a-chip applications ranging from culturing human tissue-like organoids [18] to simultaneously culturing thousands of bacterial strains in distinct cell traps [19].

One of the most common materials that microfluidic devices are made of is polydimethylsiloxane (PDMS). PDMS has many features that make it ideal for cell culture. For one, microscopic device features can easily be made on PDMS via soft lithography where PDMS is poured on a silicon wafer master mold and then baked until it is solid. PDMS is non-toxic to cells, allows free diffusion of oxygen through the device, and is optically clear for high magnification imaging. In the Biodynamics Laboratory, there have been over two decades of improvements on microfluidic devices to study genetic circuit dynamics in bacteria [19–26]. A key advantage of these devices is that they allow researchers to generate detailed, time-lapse fluorescence microscopy movies that provide temporal information that other assays do not permit.

Chapter 2 introduces a new microfluidic device for spotting multiple strains of bacterial directly from liquid culture to a multiplexed microfluidic device. This device is used in Chapters 3 and 4 as well as a previously developed microfluidic culture device that allows bacteria to be cultured at different population sizes and in the presence of different inducer concentrations.

1.2.3 Coordination of Microbial Populations

Over the last decade, synthetic biologists have increasingly focused on creating genetic circuits to control complex, population-level behavior [27, 28]. By harnessing cell-cell communication systems, like naturally occurring quorum sensing (QS) modules in bacteria, researchers have created circuits that synchronize behaviors, such as genetic oscillations, across thousands of cells [25, 29]. Population-level synthetic gene circuits have been applied in many areas, such as living-therapeutics where cell-cell communication has been used to engineer population-control mechanisms that decrease the chance of systemic inflammatory responses to engineered bacteria [13]. In recent years, circuits for cell-cell communication have helped create microbial consortia composed of distinct strains that mimic naturally-occurring ecosystems where metabolic pathways are distributed across different organisms [30]. Increased interest in population-level gene circuits have brought new challenges in circuit design and testing. Whereas the ability to screen dynamic single-cell circuits has improved dramatically in the last few years, there has been less progress on methods to screen for complex, population-level phenotypes.

Chapter 2 addresses the challenge of studying population-level phenotypes of bacteria in a more high-throughput manner than existing methods. Chapter 2 also introduces a new circuit design for coordinating genetic oscillations among populations of bacteria. Chapter 4 explores how controlling the non-genetic phenotypic heterogeneity in a bacterial population can allow the population to more flexibly adapt to different environmental conditions.

1.2.4 Host-Circuit Interactions

One of the key features of synthetic biology that makes it more challenging than traditional engineering is the complex interface between a synthetic circuit and the host cell used to execute that circuit. Recent work in synthetic biology has focused on studying the burden associated with genetic circuit expression and ways to mitigate that burden. For instance, Ceroni et al. investigated genetic circuit topologies that are less burdensome on host bacteria [31]. They further built on this work by designing a burden-responsive feedback circuit that could decrease the expression of a target protein if its expression was too burdensome to the cell [32].

Chapter 4 relates to the theme of host-circuit interactions by devising a way that bacterial populations can exploit phenotypic heterogeneity to minimize the burden associated with plasmid-based gene expression. Chapter 3 presents evidence that constitutive expression of different therapeutic genes from a plasmid can alter the dynamics of a genetic circuit.

1.2.5 Improved Circuit Stability

One of the most important challenges to overcome when taking genetic circuits out of the lab into the real world is ensuring their stability. Natural selection tells us that heterologous gene expression from a host cell will be lost over time if it is detrimental to host fitness. Now, an array of strategies have been developed to improve circuit stability including “development of environmentally specific permissive growth, mutation-resistant recoded or reduced genomes, burden-based feedback control, perfect-adaptation networks, and population product addiction” [33].

Chapter 3 addresses problems with the stability of a synchronized lysis circuit (SLC). Due to the incredibly strong selective pressure created by encoding self-lysis, the SLC is prone to failure due to mutation. For therapeutic applications using this circuit, large amounts of a lysis circuit strain need to be grown in batch culture before the strain is deployed in *in vivo*

environment. In Chapter 3, I describe the construction of a modified lysis circuit that can be completely repressed in the presence of arabinose, but functions normally in the absence of inducer.

Chapter 4 looks at the stability of plasmid-based genetic circuits in a novel way. Specifically, we show that “incompatible” plasmids, which are so named due to their inherent instability, are actually *more* stable than standard “compatible” plasmids under certain, specific environmental conditions.

1.2.6 Exploiting Cellular Heterogeneity

Since its inception, synthetic biologists have always tried to draw parallels to traditional engineering fields. Specifically, researchers in this field have tried to precisely characterize genetic parts so that they can be modularly swapped into different circuits and behave as expected. Unfortunately, unlike traditional engineering fields, biological systems are incredibly context-dependent and stochastic. Nonetheless, natural systems have achieved functions that are nearly impossible to implement with traditional engineering approaches.

The causes and impacts of gene expression noise and heterogeneity in biological systems have been studied extensively [34]. Until recently, synthetic biologists generally saw noise as a challenge to creating precise and predictable genetic circuits. Now, there is more focus on how natural biological systems exploit heterogeneity and how noise can actually be a tool for synthetic biologists to work with [35].

In Chapter 4 of this defense, we demonstrate a mechanism of creating plasmid copy number heterogeneity in a population of engineered bacteria. We show how this heterogeneity enables fitness-based adaptation of the population to different environments and also how it can improve circuit stability.

1.2.7 Library Creation and Screening for Genetic Circuits

Mutation and selection are the core processes by which nature creates novel proteins, genetic circuits, and organisms. Now, synthetic biologists mimic nature and create artificial variation in their host cells and selecting or screening for those with desired behaviors [36]. Methods for selectively introducing genetic variation to proteins and larger genetic vectors have become efficient and powerful and is relatively easy to create large mutant libraries of many different types of genetic parts (e.g. promoters, non-coding RNAs, ribosome binding sites, and proteins) [37]. As the behaviors researchers try to endow cells with become more complicated, screening variants that exhibit complex phenotypes that have dynamic behaviors in space and time has become a major focus area in library-based methods for genetic circuit creation.

To tackle this challenge, Chapter 2 describes the development of an arrayed, multiplexed, microfluidic device for culturing multiple bacteria strains from a mutant library. Chapter 3 also advances library creation and screening for synthetic biology applications, but in a different way. Specifically, in Chapter 3, we describe a pipeline for rapidly testing bacterial expressed toxins for their ability to kill cancer cells when released from the bacteria by programmed cell lysis.

1.2.8 Genetic Part Creation and Modular Cloning Toolkits

Synthetic biologists must select biological parts in order to implement genetic circuit designs. While electrical circuit components are responsible for regulating the flow of electricity through a larger system, biological parts can loosely be thought of as regulating the flux of RNA, protein, and metabolites within single cells and among populations of cells. As the field of synthetic gene circuits has grown, so has the number and type of parts available to researchers to program their desired host cell or organism. Implementation of genetic circuit design can generally be broken down into two components: 1) The selection of regulatory parts to carry out the circuit function and 2) The synthesis and assembly of those parts into the organism of choice.

One of the biggest advancements in the construction of genetic circuits came from the discovery of multiple techniques to assemble many pieces of DNA in simple, single reactions. One technique, Gibson Assembly, made possible the combination of many pieces of DNA in a single reaction by taking advantage of the mutual activity of T5 exonuclease, Phusion polymerase, and Taq ligase at 50C [38]. With this method, different genetic parts could be rapidly combined once they had been PCR-amplified with overhangs containing overlapping sequences with the adjacent part. While an incredibly powerful tool overall, Gibson Assembly does have some weaknesses such as the need to PCR amplify each part which could lead to undesirable mutations and the difficulty of assembling very small pieces of DNA due to the exonuclease activity. Another cloning strategy, Golden Gate Assembly, developed around the same time dramatically accelerated the creation of standardized, easy-to-use, genetic part kits. Golden Gate Assembly takes advantage of type IIS restriction endonucleases which cut DNA at a distinct point away from their recognition sequence. This allows parts to be designed that are digested with the same enzyme, but that have unique overhangs after digestion allowing many parts to be digested and ligated in a single reaction mixture [39,40]. By standardizing the user-defined overhangs and utilizing different type IIS restriction enzymes, a significant number of modular cloning (MoClo systems) have been developed for use in organisms spanning bacteria [41–43], yeast [44,45], plants [46,47], and mammalian cells [48]. (Figure 1.4) shows a diagram of the general MoClo workflow for generating multi-gene expression systems.

As an example of a typical MoClo work-flow, we look at the yeast MoClo Toolkit developed by Lee et. al. in the laboratory of John Dueber [44]. This toolkit exemplifies many of the characteristics researchers need to take into account in order for their MoClo platform to be used by other researchers. For example, in this yeast toolkit, the authors identify 8 unique part types (type 1-8) with predefined flanking overhangs. Each part type has as a recommended function associated with it (e.g. type 3 parts are coding DNA sequences and type 4 parts are transcription terminators), but in theory a researcher could create a new part of any type by adding

;) Modular Assembly of Genetic Circuits

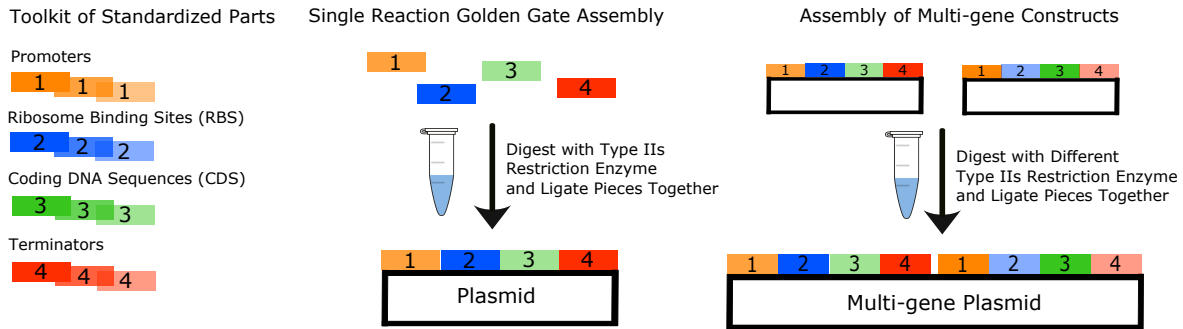


Figure 1.4: Overview of Modular Cloning Workflow via Golden Gate Assembly. Different genetic part types can be easily combined in single reactions using user-defined overhangs that created by digestion by type IIS restriction enzymes. Following rounds of assembly can be used to make multi-gene constructs.

the correct overhangs to the part. The kit employs a GFP-dropout strategy to facilitate screening of correctly-assembled constructs, and their system uses alternating type IIS restriction enzymes and selection markers to make the construction of multi-gene constructs simple and easy. Importantly, the kit is readily available on Addgene and has 100+ basic parts making it accessible. The utility of this kit has further been improved by the creation of compatible part libraries by other groups. Specifically, Shaw et al. created 42 parts for building tunable GPCR-based biosensors that are designed for use with the yeast MoClo toolkit [45].

Each chapter of this dissertation contributes novel genetic parts to synthetic biology in one way or another. Chapter 2 involves the creation of mutant circuit libraries of oscillators, uncovering new circuit versions with improved dynamics. In Chapter 3, new toxin-expressing plasmids are designed and cloned into bacteria. Chapter 5 is the most focused on the development of new parts for synthetic biology. Specifically, in chapter 5, we describe the construction of multiple new inducible systems for controlling gene expression in yeast. These inducible systems are a direct extension of the yeast MoClo Toolkit created by Lee et al. and will be deposited on Addgene to make these resources readily acceptable.

1.3 Acknowledgments

This chapter contains excerpts from a review article originally published as: Lezia, Andrew*, Miano, Arianna*, and Hasty, Jeff. "Synthetic Gene Circuits: Design, implement, and apply" *Proceedings of the IEEE* 110, no. 5 (2021): 613-630. (*equal contribution)The dissertation author was one of the primary authors and researchers of this material.

Chapter 2

Design, mutate, screen: Multiplexed creation and arrayed screening of synchronized genetic clocks

2.1 Abstract

A major goal in synthetic biology is coordinating cellular behavior using cell-cell interactions; however, designing and testing complex genetic circuits that only function in large populations remains challenging. While directed evolution has commonly supplemented rational design methods for synthetic gene circuits, this method relies on efficient screening of mutant libraries for desired phenotypes. Recently, multiple techniques have been developed for identifying dynamic phenotypes from large, pooled libraries. These technologies have advanced library screening for single-cell, time-varying phenotypes, but are currently incompatible with population-level phenotypes dependent on cell-cell communication. Here we utilize directed mutagenesis and multiplexed microfluidics to develop an arrayed-screening workflow for dynamic, population-level genetic circuits. Specifically, we create a mutant library of an existing

oscillator, the synchronized lysis circuit, and discover variants with different period-amplitude characteristics. Lastly, we utilize our screening workflow to construct a transcriptionally-regulated synchronized oscillator that functions over long timescales.

2.2 Introduction

Over the last decade, synthetic biologists have increasingly focused on creating genetic circuits to control complex, population-level behavior [27]. By harnessing cell-cell communication systems, like naturally occurring quorum sensing (QS) modules in bacteria, researchers have created circuits that synchronize behaviors, such as genetic oscillations, across thousands of cells [25, 29]. Population-level synthetic gene circuits have been applied in many areas, such as living-therapeutics where cell-cell communication has been used to engineer population-control mechanisms that decrease the chance of systemic inflammatory responses to engineered bacteria [13]. In recent years, circuits for cell-cell communication have helped create microbial consortia composed of distinct strains that mimic naturally-occurring ecosystems where metabolic pathways are distributed across different organisms [30]. Increased interest in population-level gene circuits have brought new challenges in circuit design and testing. Whereas the ability to screen dynamic single-cell circuits has improved dramatically in the last few years, there has been less progress on methods to screen for complex, population-level phenotypes.

Two approaches have greatly facilitated genetic circuit creation: 1) rational “plug and play” methods and 2) evolutionary “design, then mutate” strategies [49]. In the “plug and play” method, researchers choose well-characterized genetic components to rapidly engineer a circuit with the desired behavior predicted by a computational model [50]. While the principles of abstraction and standardization afforded by this method are alluring, the context-dependent function of genetic parts often prevents this method from reaching the same precision as in other engineering fields [51, 52]. Conversely, directed evolution or “design, then mutate” methods for gene circuit

construction take a different approach. In this method, mathematical models guide the selection of key circuit components (e.g. promoters, ribosome binding sites (RBSs), and operators) to mutate to create large libraries of variants that are then screened [53, 54]. Methods to create large, targeted mutant libraries have improved vastly, now allowing researchers to simultaneously mutate multiple genetic targets at once [55–57], use host organisms to mutate the desired target *in vivo* [58–60], and rapidly assemble many pieces of DNA in single reactions [38, 61]. Site directed mutagenesis (SDM) techniques in particular have made the creation of precisely-targeted mutant libraries, easy, inexpensive, and fast [62]. In general, a combination of rational design and directed evolution is ideal as it takes advantage of existing biological knowledge while acknowledging remaining gaps in understanding. Regardless of the chosen method to get from conceptual design to functional circuit, the ability to rapidly screen circuit variants for a desired phenotype is paramount.

Presently, devising methods to screen variants from large libraries is more challenging than creating the libraries [63]. As researchers continue to study more complex, time-dependent cellular behaviors, there is a need for technologies that take advantage of the high spatio-temporal information provided by live-cell, time-lapse microscopy while maintaining the ability to identify and isolate unique variants from large libraries. New advances in library-screening have done just this, improving the throughput of screening while maintaining the ability to link genotype-phenotype relationships in interesting variants. Two separate groups recently developed related imaging-based methods for observing complex phenotypes in large pool-synthesized strain libraries and connecting the observed phenotypes with the underlying cell genotypes [64, 65]. Both of these methods separate phenotype observation and genotype determination into two steps. After time-lapse imaging is used to observe complex phenotypes among library members either adhered to a cover-slip or continuously-cultured in a mother machine-like microfluidic device, the cells are fixed and multiple rounds of fluorescent *in situ* hybridization (FISH) are performed to detect unique RNA barcodes expressed by each strain. Since each RNA barcode is

associated with a known, unique genetic perturbation, barcode determination for a given strain directly connects genotype and phenotype, something that has typically been challenging for large, pooled-strain libraries. In an impressive demonstration of their workflow, Lawson and Camsund et al. determined how 235 different CRISPR interference knockdowns impacted coordination between replication and division cycles in *E. coli* [66].

Another group recently developed a method to isolate single cells after time-lapse microscopy (SIFT) using optical trapping [67]. They screened a large library of precise synthetic gene oscillators and uncovered variants spanning a 30-fold range of average periods. In this method, since cells can be retrieved after long-term imaging of dynamic behavior in a microfluidic device, cells with interesting phenotypes can be propagated and sequenced. Notably, tens of thousands of cell lineages can be screened per day with this technique. While both *in situ* genotyping and optical trapping of strains from pooled-strain libraries dramatically improve screening for dynamic phenotypes at the single cell level, these technologies are currently incompatible for screening population-level genetic circuits that rely on cell-cell communication.

In this work, we address the gap in techniques to screen mutant libraries of population-level genetic circuits for dynamic phenotypes. We build upon previously-developed multiplexed microfluidic platforms for arrayed cell library screening to simultaneously culture dozens of unique *E. coli* populations from large mutant libraries [19]. Our technique enables us to rapidly array potentially up to 48 distinct strains on a microfluidic device directly from liquid culture. Using this arrayed-strain microfluidic culture system, we develop a workflow for quantitatively screening libraries of gene circuits with complex phenotypes only seen at the population-level. We use this workflow to tune the dynamics of an existing oscillator, the synchronized lysis circuit (SLC) [13], and uncover new principles regarding its regulation. Additionally, we develop a new synchronized gene oscillator and demonstrate how we are able to improve the circuit by combining computational modeling with our screening pipeline. The final oscillator we develop exhibits robust and tunable oscillations over long time scales. Overall, this work demonstrates the

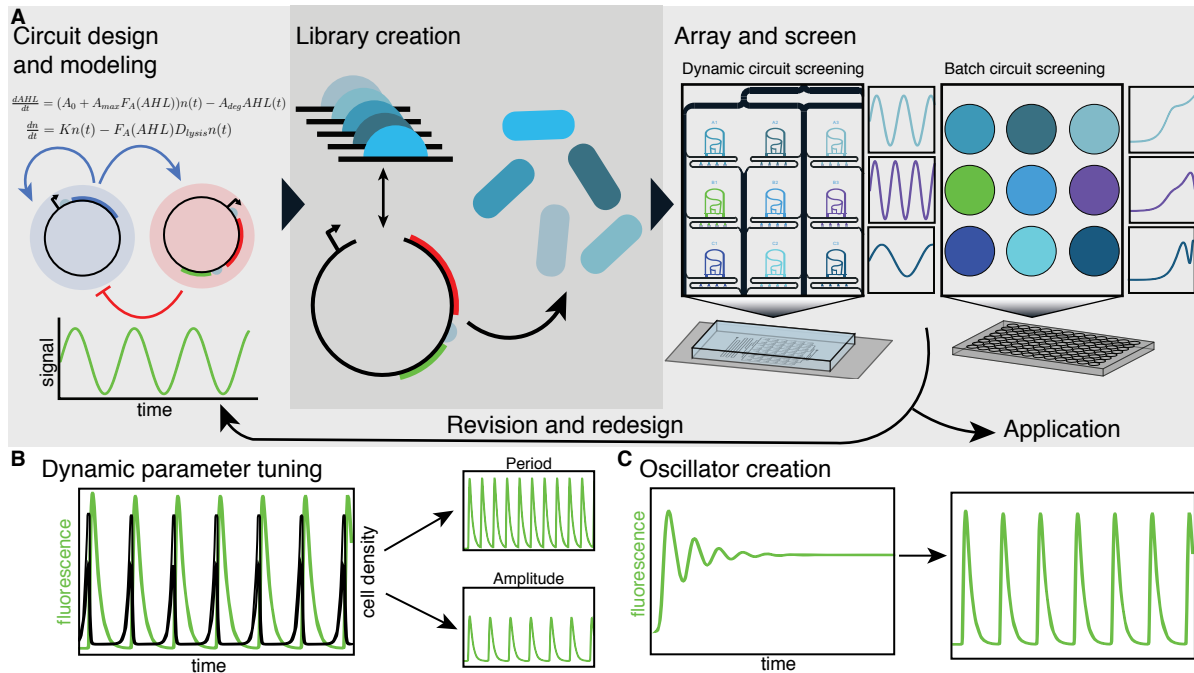


Figure 2.1: Synthetic oscillator creation and tuning through directed mutagenesis and screening. (A) Overview of gene circuit creation and screening work-flow. Mathematical modeling of circuit dynamics helps to identify parameters to target in order to improve or modify circuit behavior. Large libraries of a given circuit are quickly constructed via site-directed-mutagenesis (SDM). High-throughput, multi-strain microfluidic devices permit dynamic phenotype screening to supplement and improve upon traditional batch-culture methods of circuit screening. Circuit variants with desired or interesting behavior can be used for real-world applications, used to better inform circuit models, or placed through another cycle of mutagenesis and screening to further improve behavior. (B) The gene circuit library construction and screening work-flow developed here can be used to tune the behavior of an existing oscillator circuit. (C) The system can also aid in the construction of new genetic circuits such as oscillators synchronized at the population level.

power of directed mutagenesis to supplement rational circuit design and illustrates how arrayed, multi-strain microfluidics can improve the ability to screen dynamic phenotypes at the population level.

2.3 Results

2.3.1 Overview of directed evolution approach for synthetic oscillator creation and tuning

We sought to develop a system for constructing and tuning dynamic, population-level gene circuits by directed mutagenesis and screening (Figure 2.1). In this work, we focus on tuning and creating QS-based oscillator circuits in *E. coli* as they: 1) exhibit complex, time-varying phenotypes that can be difficult to predict and monitor, 2) have many dynamic parameters that can be tuned (e.g. period, amplitude, and prominence), and 3) are increasingly being tested for real-world applications. We begin by creating targeted mutant libraries of a genetic circuit using site-directed-mutagenesis (SDM). We utilize deterministic modeling of circuit dynamics to help guide the choice of circuit elements to mutate. Following library creation, we screen strains for interesting phenotypes in both well plate-based batch culture and microfluidic-based continuous culture. Batch culture screening approaches permit rapid screening of many variants for significant phenotype differences, but are insufficient for observing dynamic phenotypes only seen in continuous culture where the metabolic state of the cell population is relatively constant [68]. Thus, after an initial library screen in 96 well-plates, we deploy a high-throughput, multi-strain microfluidic device to further screen interesting library members.

The multi-strain device was adapted from a previous design in which a single inlet-outlet system fed a manifold array of 2,176 cell traps [19]. For improved compatibility with liquid cultures instead of solid colonies (liquid cultures have a greater tendency to wick and spread through channels), the spacing between spotting regions where cells are deposited was increased from 1.125 mm to 2 mm (Figure 2.2). The final PDMS-based device consists of a 6x8 array of cell trapping regions that are loaded with liquid bacterial cultures by acoustic droplet ejection using a Labcyte Echo 550 prior to bonding the device to a glass slide or coverslip. Each position features four smaller cell traps downstream of the large trapping region that serve as regions of interest

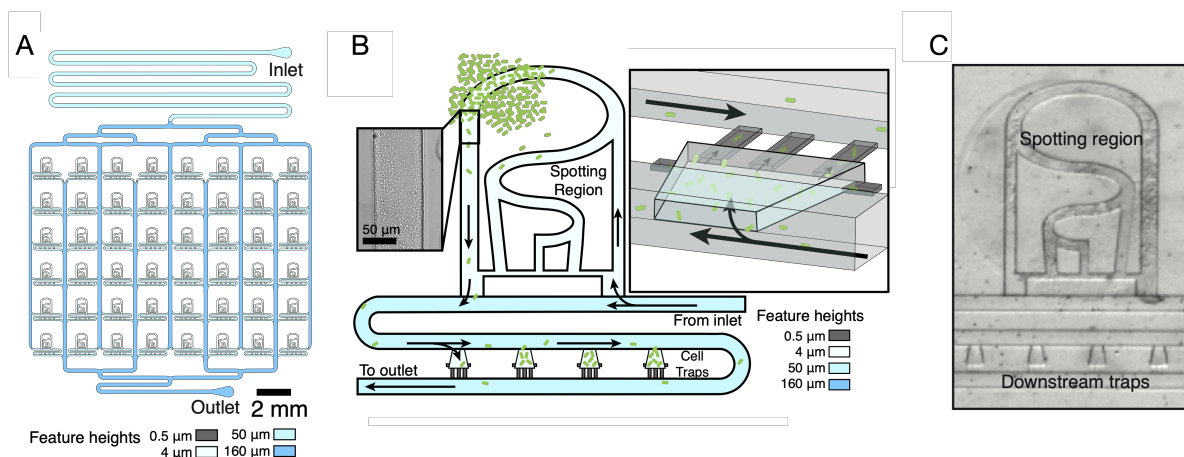


Figure 2.2: A multi-strain microfluidic device for dynamic phenotype screening. (A) A microfluidic device was developed that allows 48 unique strains to be arrayed by acoustic droplet ejection and cultured continuously. (B) Each individual growth region consists of a spotting region where a liquid culture of a strain is deposited. Fluid flow moving through the channels of the spotting region carries some cells toward cell traps connected to the main fluidic channel. As fluid flow pushes cells into the cell traps, they begin to grow and fill up the trapping region as they cannot pass through the $0.5 \mu\text{m}$ height device channel. During an experiment, cellular populations in the trapping region are imaged continuously to observe gene expression dynamics. (C) Microscope image of cell spotting region and smaller downstream traps.

(ROIs) for tracking population dynamics in fluorescent and transmitted light channels. With this device, up to 48 distinct positions can be loaded with a unique *E. coli* strain, each housing a continuous culture for multiple days where media composition and flow rate are precisely controlled. The high spatio-temporal resolution data from variants can be used to improve circuit models and inform design considerations for relevant applications.

2.3.2 Tuning the oscillatory dynamics of a synchronized lysis circuit by directed mutagenesis

To demonstrate the ability of our system to tune circuit dynamics via directed mutagenesis and screening, we worked with a single plasmid version of a previously-developed synthetic gene oscillator, the synchronized lysis circuit (SLC) [13]. Bacteria transformed with the SLC have been used to release therapeutics in solid tumors [9, 13, 69, 70], and the ability to tune the circuit

dynamics could improve the utility of this circuit for cancer therapy. In the SLC, expression of the LuxI protein, and subsequent production of the QS autoinducer N -Acyl homoserine lactone (AHL), generates synchronized positive feedback in a colony of isogenic cells. The positive activation of the pLux promoter in-turn drives negative feedback via expression of the lysis protein, E, from phage ϕ X174, causing synchronized lysis of the colony. A few cells in the population are able to survive the lysis event and continue growing, perpetuating cycles of growth, gene expression, and mass lysis (Figure 2.3A).

We generated a mutant library of the SLC by randomizing five base pairs in the ribosome binding site (RBS) upstream of the lysis protein leading to as many as 1024 unique circuit variants (Figure 2.3A). We chose to create a library significantly larger than the maximum throughput of our microfluidic device to increase the probability that transformants selected at random would all have different RBS sequences. Altering the strength of the RBS preceding the lysis gene affects the translation rate for the lysis protein, which potentially alters the oscillatory dynamics by modulating the negative feedback component of the circuit. We hypothesized that strains with a stronger RBS driving the lysis gene would lyse more rapidly upon reaching a threshold population size leading to higher frequency oscillations compared to strains with weaker RBSs.

We randomly selected 24 members from the SLC library for screening. We cultured these strains in a 96 well plate and monitored their lysis dynamics using a TECAN microplate reader. For the 24 strains examined in batch, we saw differences in the presence and magnitude of lysis events and GFP expression immediately before a lysis event (Figure 2.3B). While differences in cell population dynamics and GFP fluorescence can be coarsely ascertained from the batch culture data, sustained SLC oscillations are typically only seen in continuous culture, necessitating the use of multiplexed microfluidics for dynamic parameter screening.

In parallel with the batch culture experiments, the 24 selected library members were screened on a 48-position multiplexed device using a previously described custom optical assembly [19]. Both fluorescence and transmitted light images were collected every 10 minutes,

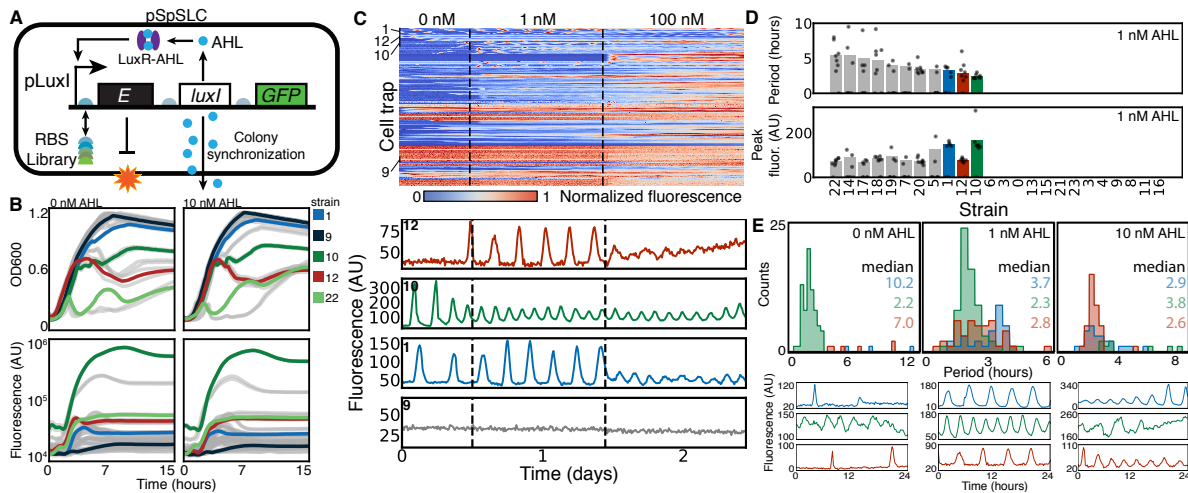


Figure 2.3: Screening of Synchronized Lysis Circuit (SLC) library strains. (A) A single-plasmid synthetic oscillator (pSpSLC) was developed with AHL production from the LuxI protein as a cell-synchronized positive feedback mechanism, and cell lysis as negative feedback. A library was created by randomizing five bases in the RBS upstream of the lysis protein gene, *E*. (B) When screened in batch culture, the library strains exhibit a range of growth, lysis and GFP expression dynamics. (C) 24 library members were screened on a 48 strain microfluidic device and subjected to temporal changes in the background AHL concentration. Different, dynamic fluorescent phenotypes were observed across these 24 strains, with four examples shown. In the heat map, fluorescence (AU) of each strain was linearly scaled between 0 and 1 relative to itself. (D) Extracted parameters, oscillation period and peak fluorescence, of 24 oscillator strains under 1 nM AHL. 8 cell traps were evaluated for each strain, with each point representing the measured value for a single trap. Non-oscillating cell traps were reported as zero, with bars representing the mean of the oscillating traps. (E) Peak-peak interval histograms for three library strains under different AHL concentrations, with 8 distinct cell traps evaluated for each strain. Representative GFP time-traces for each strain at the specified AHL concentration are shown below.

with fluorescence used as the primary output to quantify oscillator dynamics. While 48 unique strains can grow in the device simultaneously, screening only 24 members allowed for additional replicates on the chip (8 small cell trap ROI's per strain). Experiments were started on LB media with 0 nM AHL for 12 hours during initial trap filling, then subjected to varying background concentrations of AHL over a several day period to survey oscillatory dynamics. Clustering of all cell traps revealed an abundance of phenotypes, predominantly “broken” oscillators with no fluorescent oscillatory dynamics, but also several working oscillators (Figure 2.3C). Four strains are highlighted in Figure 2.3C, showing three working oscillators that activate under different AHL concentrations and have differences in their period and amplitude across conditions. Dynamic parameters (period and peak fluorescence) were extracted for all 24 strains at 1 nM AHL to quantitatively demonstrate the variety of oscillators discovered by library screening (Figure 2.3D). To further characterize the three working oscillators highlighted in Figure 2.3C (pSpSLC₀, pSpSLC₁₀, and pSpSLC₁₂), peak-peak interval histograms for these strains were constructed (Figure 2.3E). Analysis of these oscillation frequencies at varied AHL concentrations reveals ideal conditions for each oscillator, with pSpSLC₁₀ exhibiting more consistent oscillations at 1 nM AHL, and pSpSLC₁₂ oscillating more consistently at 10 nM AHL. For strain pSpSLC₁₂, oscillations are sparse at 0 nM of AHL, regular at 1 nM and 10 nM with frequency increasing at higher concentrations, and absent at 100 nM (Figure 2.3C and E). The trend of more frequent oscillations with increasing exogenous AHL concentration matched modeling results obtained using a deterministic model of the SLC (Figure 2.7).

To better understand how changes to the lysis gene RBS led to different oscillator dynamics, we investigated two strains in more detail. Specifically, we looked at the original oscillator (pSpSLC₀) used to build the library which exhibited frequent oscillations with little to no GFP production before lysis and compared it to library strain 10 (pSpSLC₁₀) which exhibited slower oscillations and high GFP expression before each lysis event (Figure 2.4A and B, Supplemental Videos 1 and 2). To directly characterize how the different RBSs affected population lysis in

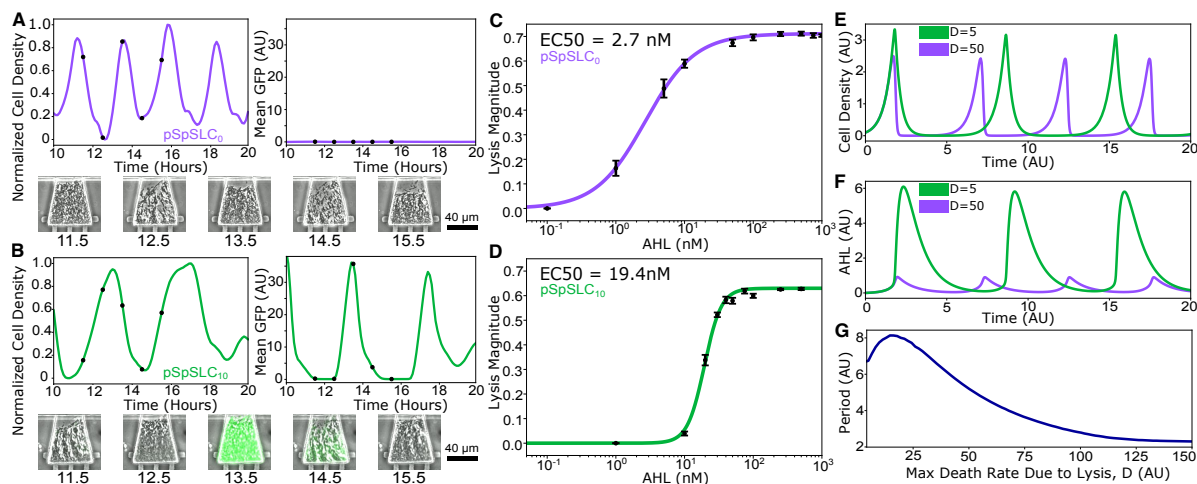


Figure 2.4: Comparison of SLC library strains with varying lysis strengths reveals differences in gene expression dynamics. (A) GFP and cell density time traces for the original single plasmid SLC (pSpSLC₀) grown in the multistrain microfluidic device with accompanying microscope images of one microfluidic trap for specific time points. (B) GFP and cell density time traces for SLC library strain 10 (pSpSLC₁₀) grown in the multi-strain microfluidic device with accompanying microscope images of one microfluidic trap for specific time points. (C) Lysis dose-response curve for pSpSLC₀. Error bars represent standard deviation of three separate lysis measurements. (D) Lysis dose-response curve for pSpSLC₁₀. Error bars represent standard deviation of three separate lysis measurements. (E) SLC modeling results showing how changing the maximum death rate due to lysis, D , impacts oscillatory population dynamics. (F) SLC modeling results showing how changing the maximum death rate due to lysis, D , impacts AHL concentration dynamics. (G) Modeling results showing how the period of lysis oscillations changes with the parameter D .

response to AHL, we re-constructed the strains without the positive feedback component, *luxI* (Figure 2.7B). In batch culture, we then grew the strains under varying AHL concentrations to generate a lysis dose-response curve for each RBS (Figure 2.4C, D and Figure 2.7B). We found that the original strain with higher frequency oscillations had a much lower EC_{50} compared to the lower frequency library strain, strongly suggesting that pSpSLC₀ had a higher translation initiation rate for the lysis gene. Using a previously-developed deterministic model of the lysis circuit dynamics [71], we confirmed that the period of oscillations is generally inversely correlated with the strength of expression for the lysis gene (Figure 2.4E,F, and G). Additionally, this model showed that the peak AHL (and GFP) production immediately preceding a lysis event decreased as the expression strength of the lysis gene was increased (Figure 2.4F and Figure 2.72C). This prediction from the model agreed with our experimental results where the library strain with the weaker RBS driving the lysis gene exhibited substantially more GFP expression preceding lysis.

The usefulness of *in-situ* screening with a “design then mutate” approach was further demonstrated when investigating rational design tools, such as the the RBS calculator developed by Salis et al. [72]. For the pSpSLC₀ RBS and the pSpSLC₁₀ RBS sequences, the RBS calculator predicted lysis protein translation rates of 1957 and 1460 respectively. Despite these small differences in predicted translation rates, within the reported margin of error for the calculator [73], the experimentally measured lysis dose response curves for the two RBS variants demonstrated significant differences in lysis gene expression strength, with the pSpSLC₀ having an EC_{50} of 2.7nM and the pSpSLC₁₀ having an EC_{50} of 19.4nM (Figure 2.4C, D). To further examine these RBSs, they were placed in a circuit with a simpler phenotype: constitutive expression of sfGFP on a low copy number plasmid. In this GFP-expressing circuit, the pSpSLC₀ RBS sequence led to an approximately 10 fold increase in GFP expression relative to the pSpSLC₁₀ RBS sequence, while the RBS calculator predicted a lower translation rate (8839) for the pSpSLC₀ RBS than the pSpSLC₁₀ RBS (14049) (Figure 2.10A). It is well-documented that the protein coding component of an mRNA transcript can affect translation initiation, leading to the same RBS sequence yielding

different translation rates depending on the downstream sequence [74, 75]. Nonetheless, our characterization of these RBS sequences in an AHL-inducible lysis circuit and a constitutive GFP-expressing circuit yielded similar results for their relative strength. Thus, in this case, we found *in-situ* screening to be more useful than existing rational design tools, particularly in the context of the lysis circuit where small changes in expression level can lead to large changes in observed phenotype due to the complex mechanism of the lysis protein [76]. Together these results highlight the importance of screening for desired circuit properties, even for libraries where circuit components can be rationally designed to a degree, especially in the context of complex phenotypes such as the population-level oscillations of the SLC.

Our results here demonstrate the importance of considering the relative RBS strength for the lysis gene in the SLC. In therapeutic applications using this circuit [13], it may be desirable to have the production of a therapeutic gene driven by the same pLux promoter as the lysis gene. Here, we demonstrate the importance of considering the relative expression strength for the lysis gene and a therapy gene in this scenario. If the lysis gene translation initiation rate far exceeds that of the therapy gene, the engineered cells may exhibit robust cycles of growth and lysis without releasing a significant amount of therapeutic, akin to the case for the original SLC strain where there was little to no GFP production preceding each lysis event.

2.3.3 Creation of a transcriptionally-regulated synchronized gene oscillator circuit via directed mutagenesis and screening

Beyond tuning the oscillatory phenotypes of an *existing* oscillator, such as the SLC, we sought to further show the utility of our screening workflow for optimizing *new* population-level genetic circuits with complex dynamics. While tuning the dynamic behavior of a circuit is a common goal in synthetic biology, it is often difficult to create a circuit that displays the desired behavior predicted by a model in the first place, especially for circuit designs where the desired dynamics might only exist for a small number of parameters. We chose to implement a

synchronized gene oscillator design consisting of coupled positive and negative feedback loops using only quorum sensing molecule production and simple transcriptional regulation.

While a plethora of QS-mediated, population-level oscillators have been previously developed in bacteria, most do not exclusively use transcriptional repression as a negative feedback mechanism, often relying on quorum sensing molecule degradation proteins, or in the case of the SLC, the destruction of cellular components [13, 29, 77, 78]. In the case of population-level oscillators, using only transcriptional repressors may be particularly applicable to QS systems for which QS molecule degradation enzymes have not been identified. In a recent study, Chen et al. employed the repressor LacI as a negative feedback mechanism in conjunction with the QS molecule degradation enzyme AiiA in a multi-strain oscillator [29]. For this system, they explored different positive and negative-feedback motifs, notably finding that a design with 2 negative and 2 positive feedback links (P2N2) was more robust than a design with a single negative feedback link (P2N1). We sought to further explore these motifs, instead in a single-strain system that could require fine parameter tuning to improve, or even see, oscillatory dynamics.

To start, we created two versions of the oscillator circuit with slightly different topologies, similar to Chen et. al (Figure 2.5A and B). The first version, P2N1-Tet (no negative auto-regulation), uses two AHL inducible promoters: pLuxTet, which is activated by the LuxR-AHL complex and repressed by the tetracycline repressor protein, TetR, and pLux, which is only activated by LuxR-AHL. pLuxTet drives production of LuxI, which synthesizes AHL and drives positive feedback. pLux drives production of fluorescently-tagged TetR, which represses pLuxTet. As each cell accumulates high levels of TetR, the pLuxTet promoter becomes inactivated leading to a steady decline in AHL as it's removed from the population by fluid flow. The second circuit topology, P2N2-Tet (with negative auto-regulation), is identical to P2N1-Tet except that the TetR-repressible pLuxTet promoter is used for expression of both LuxI and TetR. TetR was chosen as the transcriptional repressor because it binds the TetO operator as a dimer [79] and

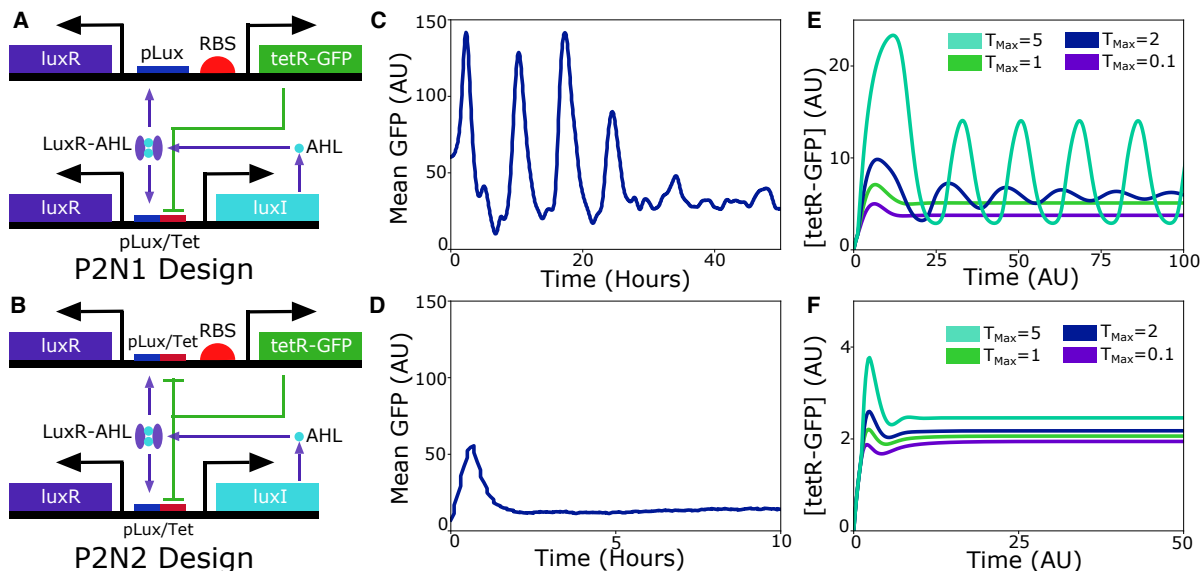


Figure 2.5: Comparison between P2N1-Tet and P2N2-Tet Circuit Topologies (A) Circuit diagram for the P2N1-Tet design. (B) Circuit diagram for the P2N2-Tet design. (C) Representative mean GFP time trace for first implementation of the P2N1 oscillator design in a cell trap with area of $0.81E-2 \text{ mm}^2$ at an aTc concentration of 50ng/mL . (D) Representative time trace for first implementation of the P2N2-Tet oscillator design in a cell trap with area of $0.81E-2 \text{ mm}^2$ at an aTc concentration of 50ng/mL . (E) Modeling results for P2N1-Tet design with delay parameter set to one for varying maximal expression levels of TetR. (F) Modeling results for P2N2 design with delay parameter set to one for varying maximal expression levels of TetR (T_{Max})

is typically modeled with a lower hill coefficient than LacI, which binds LacO as a tetramer and can also be involved in DNA looping [80]. Previous research on delayed-negative feedback oscillators suggests that high non-linearity (i.e. cooperativity) in repressor binding increases the parameter range for which oscillatory behavior is observed [81,82]. Thus, for designs with lower repressor binding cooperativity, such as the TetR design explored here, it may be important to screen mutant libraries for circuits that oscillate.

Initially, we wanted to characterize a first implementation of each oscillator design and choose the more promising one to optimize via mutagenesis and screening. We used a previously-developed single-strain microfluidic device with a variety of cell trap sizes and a concentration gradient [17] to characterize the behavior of both designs for varying levels of anhydrotetracycline (aTc). The first implementation of the P2N2-Tet design did not lead to oscillations in any of the

cell traps analyzed. Instead this circuit only displayed single GFP peaks that quickly decayed to steady-state GFP levels as shown in the representative time trace in Figure 2.5D (bottom). Furthermore, GFP peaks for this design were only seen in the three largest trap sizes, and the steady-state mean trap GFP fluorescence was proportional to the concentration of aTc in the media (Figure 2.8A and C). In contrast, the initial version of the P2N1-Tet design occasionally displayed clear oscillatory peaks (Figure 2.5C); however, oscillations were never seen in the largest trap size tested, and only seen in 37.5% of the 32 cell traps analyzed for the next two smallest trap sizes.

To better understand the differences we saw experimentally between the two oscillator designs, we created a mathematical model consisting of delayed ordinary differential equations. In the model for the P2N1-Tet design, we saw that oscillatory behavior could be achieved for smaller values of the delay parameter than for the P2N2 design (Figure 2.5E and F). Specifically, when the delay term, τ , was set to one, the P2N2-Tet design displayed a single peak in TetR-GFP expression followed by a rapid decay to a steady state value. On the other hand, we found that the P2N1 design could achieve oscillatory behavior even when the delay term was set to one (Figure 2.5E). Based on this, we hypothesized that the experimentally-observed lack of oscillations for the P2N2-Tet design was due to insufficient delay in the negative feedback caused by TetR repression. We also looked at the effect that repressor cooperativity had on the propensity for oscillatory behavior in our model of the P2N2-Tet circuit. We found that for increased repressor cooperativity (i.e. hill coefficient of 2 vs. 4), the P2N2 design could generate oscillations for smaller values of the delay parameter, τ (Figure 2.8 3B). This corresponds well with results obtained from the two strain oscillator study of Chen et al. as well as previous oscillator studies from our group demonstrating that LacI (higher hill coefficient than TetR) negative autoregulation can be a feature of robust oscillator circuit designs [21].

In modeling the P2N1-Tet oscillator design, we also found that the existence of sustained oscillations was highly-dependent on the maximum TetR expression rate. Specifically, if the TetR

expression rate parameter was not sufficiently high, the model predicted oscillations that would quickly decay over time (Figure 2.5E). Based on these results, we hypothesized that we could optimize our initial implementation of the P2N1-Tet design to exhibit more regular oscillations by tuning the expression strength of TetR-GFP by directed mutagenesis followed by screening of the resultant library with our multiplexed microfluidic device.

To create a mutant library where TetR expression strength was varied, we changed the RBS preceding TetR (highlighted in Figure 2.5A) to RBS sequences derived from the Anderson Lab RBS collection [83] by SDM. The final library consisted of as many as 4096 unique sequences. For initial screening of this circuit library, we picked 48 unique colonies and screened them in batch culture using a 96-well plate in the presence and absence of 100 ng/mL anhydrotetracycline (aTc) and tracked their GFP expression during growth (Figure 2.6A). For further screening in microfluidics, we selected 8 library members that spanned the range of GFP expression we saw in the well plate assay and loaded these strains on the multi-strain microfluidic platform. Only 8 out of the 48 strains from the batch culture screen were chosen to culture in the microfluidic device because these strains spanned the range of GFP fluorescence levels we saw in the batch culture screen. When grown in the multi-strain device, the majority of library strains exhibited one or two small peaks in TetR-GFP expression before decaying to relatively steady, intermediate levels of expression (Figure 2.6B).

The original P2N1-Tet strain and strain D1 were the only two strains screened that consistently had more than one GFP peak in the multi-strain device. To quantify the differences between the damped oscillations shown by the original strain and strain D1, we fit replicate GFP traces for each strain with a decaying exponential function to determine the effective damping coefficient for each strain. Strain D1 had a smaller damping coefficient than the original strain, indicating the strain D1 was closer to displaying sustained oscillations in this device. In order to further study the behavior of strain D1 and compare it to the original P2N1-Tet strain, we grew strain D1 in the single-strain microfluidic device used to initially characterize the original

P2N1-Tet strain.

When strain D1 was grown in the microfluidic chip with variable trap sizes, we found that it exhibited regular oscillations over long time periods in multiple trap sizes (Figure 2.6C, Figure 2.9A, and Supplemental Video 3). Specifically, strain D1 was able to oscillate in larger trap sizes, had a larger amplitude, and oscillated in a much larger percentage of cell traps than the original P2N1-Tet strain (Figure 2.6C, D and Figure 2.9A, B). Moreover, we found that strain D1 had less variability in oscillatory period compared to the original strain, as shown in the peak-peak interval histogram of Figure 2.6E.

Additionally, we found that the characteristics of the oscillations for the D1 strain were unaffected by aTc concentrations ranging from 0 to 50 ng/mL, with no clear impact on period or amplitude (Figure 2.9B and D). While this apparent insensitivity to aTc could be a result of aTc degradation during the experiment due to the molecule's photosensitivity, our previous experiment with the P2N2 design suggests that aTc is stable for at least 20 hours in the microfluidic experiments, as we saw stable aTc-mediated TetR-GFP expression differences maintained for more than a day in that experiment (Figure 2.8D). Modeling results suggested that aTc would increase the DC offset of oscillations as well as extend the period of the P2N1-Tet design (Figure 2.9E). Thus, it is likely that the lack of aTc impact we saw was a result of the concentrations being too low compared to the very strong TetR expression. For instance, aTc concentrations of 100ng/mL are often used for full induction of TetR-repressible promoters in *E. coli* Mg1655 Z1, a strain with constitutive genomic production of TetR [84]. It is likely that the TetR-expression level is much higher in the P2N1-Tet circuit due to the LuxI-mediated positive feedback, relatively high plasmid copy number, and lack of negative autoregulation to prevent TetR levels from increasing rapidly before AHL production is shut off. Lastly, the period of the D1 oscillator was also able to be tuned by varying the flow rate, with reduced flow rate leading to more frequent oscillations (Figure 2.9C).

While our experimental data strongly suggest that the RBS in the D1 oscillator strain

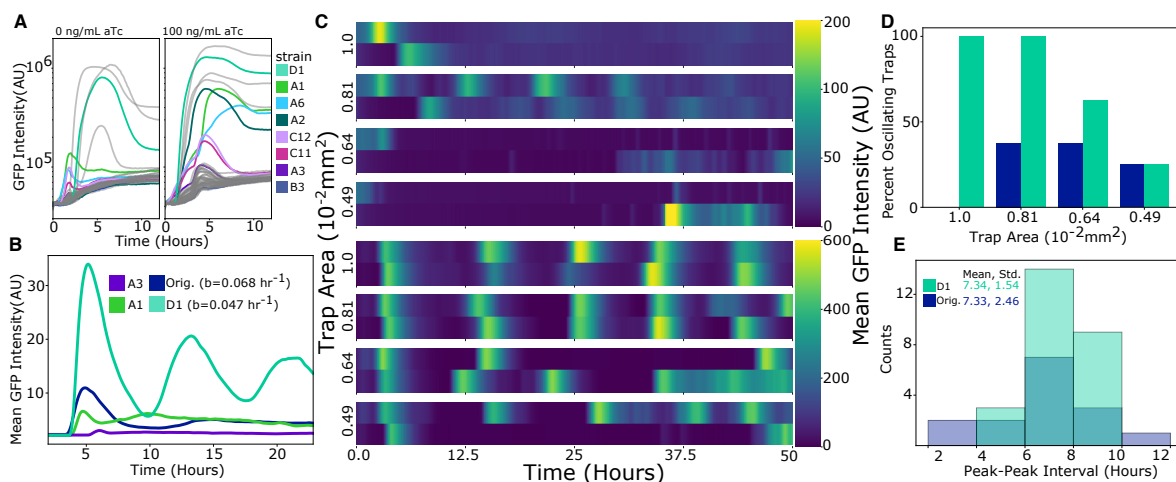


Figure 2.6: Optimizing a synchronized genetic oscillator via directed mutagenesis and screening. (A) A library of potential oscillator strains was created by randomizing the RBS in front of the *tetR-gfp* gene by SDM. All of the strains were screened for differences in TetR-GFP expression in batch culture in the presence of 0 or 100 ng/mL aTc. The eight highlighted strains were selected for additional characterization and testing in the multi-strain microfluidic platform. (B) Representative TetR-GFP time traces for a subset of strains screened in the multi-strain platform. Damping coefficients, b , were calculated for the original strain and strain D1 by fitting the GFP time traces with decaying exponential functions. The reported coefficient values represent the mean value for 4 replicate cell traps and 12 replicate cell traps for the original and D1 strains respectively. Standard deviations for mean coefficient values were 0.0053 and 0.011 for the original and D1 strains respectively. (C) Heatmaps showing oscillatory dynamics for the original implementation of the synchronized oscillator (top) and oscillator library strain D1 (bottom) in cell traps of different sizes with 50 ng/mL aTc. Color scale is linear and represents mean trap GFP signal (AU). (D) Comparison of the number of cell traps that exhibited oscillations for both strains. For each cell trap size, 16 unique cell traps were analyzed. Oscillatory behavior was defined as a given cell trap population showing 3 or more peaks in mean GFP fluorescence during a 50 hour time window. (E) Peak-peak interval histogram comparing the dynamics of the original strain to strain D1 in cell traps with with area of $0.81 \times 10^{-2} \text{ mm}^2$. Counts represent the number of peak-peak pairs observed across 16 cell traps for each strain.

led to stronger TetR-GFP expression levels than in the original P2N1 oscillator strain, we again looked translation rates predicted by the RBS calculator. We found that the RBS calculator results did not correlate well with our experimental results, with the calculator predicting a translation rate of 9438 for the original RBS and 1658 for the D1 RBS. As we did for the RBS sequences from the lysis circuit library, we cloned these RBS sequences in front of a constitutive promoter on a low copy plasmid driving sfGFP expression. In this circuit, the D1 RBS had about 4-fold more GFP expression than the original P2N1 RBS. In this context, the RBS calculator again predicted stronger expression for the original RBS (translation rate of 6614) compared to the D1 RBS (3728) in direct contrast to the experimental results (Figure 2.10B). Together, these results further highlight the utility of screening genetic circuit variants for desired behavior even when rational design tools exist.

2.4 Discussion

Tuning genetic circuits by screening variant libraries for desired phenotypes has long been fundamental to synthetic biology design. However, the mass-screening of dynamic phenotypes has remained a persistent challenge and our ability to generate genotypic diversity far exceeds our ability to screen complex phenotypes [63]. Despite limited means for dynamic phenotype screening, canonical gene circuit motifs, including oscillators, logic gates, and feedback controllers have been increasingly deployed in time-dependent applications spanning metabolic engineering to therapeutic delivery [13, 85–88]. Multiplexed microfluidics, such as ours, can aid in the development of circuits like these, for both academic research and as synthetic biology exits the lab and enters the real world.

For bacteria, it is well-documented that the growth-state of a growing culture has a significant impact on gene expression [89–91]. Thus, to reliably characterize and evaluate complex circuit dynamics, the cellular growth environment should be as constant as possible. In

this article, we further demonstrate the importance of continuous culture screening, specifically in the context of dynamic gene circuits like oscillators. In screening the SLC library, we saw that the presence of a lysis event in the batch culture screen generally correlated with a propensity for robust oscillations in continuous culture, but continuous culture was necessary to confirm and detect sustained oscillations for any library members. On the other hand, batch screening of the TetR-GFP synchronized oscillator provided little evidence regarding which strains were more likely to oscillate in microfluidic culture but did facilitate the selection of strains with varying TetR expression for further testing in microfluidics. One likely reason why oscillations were not seen in batch culture for the TetR synchronized oscillator is that the oscillatory period of the circuit that was seen in microfluidics (around 10 hours) is considerably longer than the time the cellular population remained in exponential phase (around 3-4 hours) during batch culture. While our results show that batch culture can offer some insight into the design of oscillator circuits, in this context, batch culture is most useful as a means to cull non-interesting variation in dynamic gene circuit libraries. Ultimately, the microfluidic approach is necessary for fully characterizing dynamic phenotypes.

Microfluidic culturing systems have served as useful tools for approximating complex real world environments in the past, simulating environments spanning soil to human organs [92,93]. While not a perfect recreation of these complex environments, tuning environmental and time-dependent parameters with microfluidics serves an important role in prototyping and scaling up gene circuits. This work shows how environment, specifically population size, can significantly impact the circuit dynamics, with the TetR synchronized oscillator behaving differently when grown in different cell trap geometries. Understanding how circuit dynamics change, or are resistant to change, as trap size varies can be critical to predicting how a circuit might behave when deployed in a real world, non-microfluidic environment.

One challenge in engineering *population-level* behaviors is that they are resistant to screening with sufficiently high throughput to interrogate the large libraries typically needed

for directed evolution where complex sequences such as those encoding proteins are targeted to improve strain performance. While some of the novel, pooled-library approaches for screening complex phenotypes described earlier achieve orders of magnitude greater throughput than what we present here, there is no clear path forward to adapting those approaches to situations where desired phenotypes for a given strain are only seen in large population sizes or when the strain is spatially isolated from all other library members. Thus, in the future, we could envision workflows where key single-cell indicator phenotypes that are suggestive of population-level phenotypes are first screened for using high-throughput pooled library techniques and then a subset of interesting variants is screened at the population-level using an arrayed, continuous culture platform like the one we present here. In the future, the throughput of our device could potentially be increased to accommodate on the order of 1000 unique strains as indicated by our groups previous work on using large bacterial libraries for biosensing [19].

2.5 Supplemental Figures

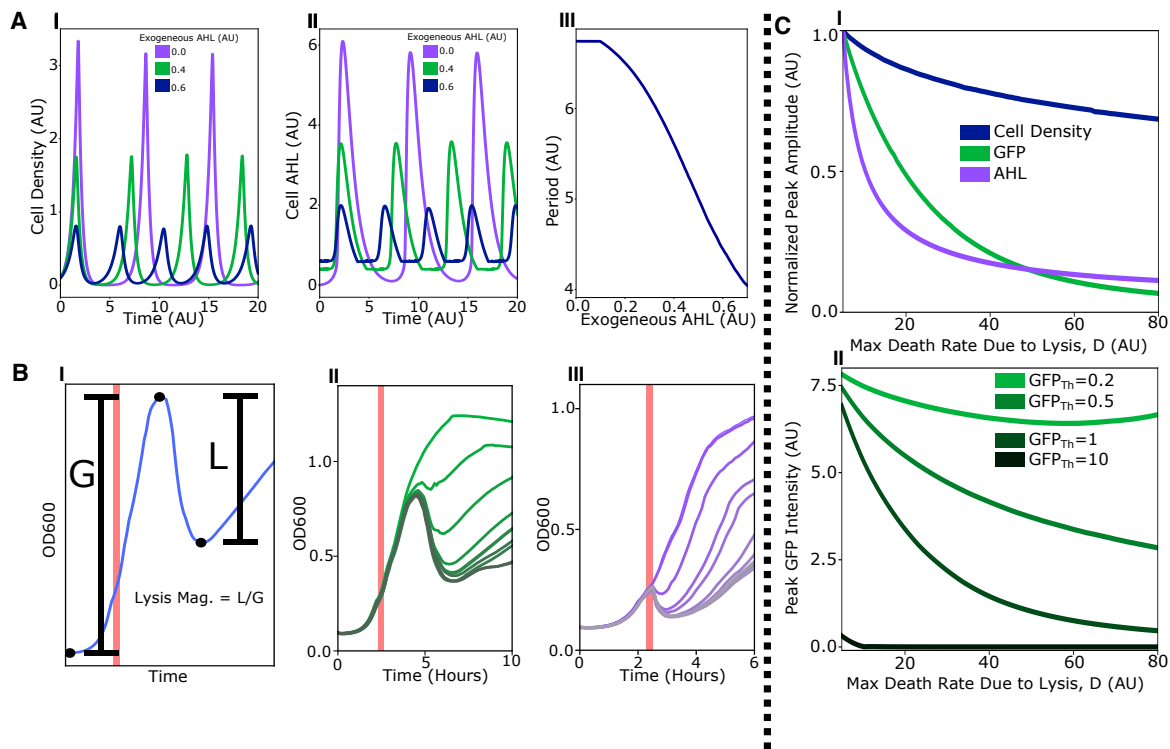


Figure 2.7: Modeling the effects of exogenous AHL and lysis Gene RBS strength on SLC oscillatory dynamics (Supplementary data related to Figures 2.3 and 2.4) (A) Modeling results showing effect of exogenous AHL on SLC dynamics. I) Cell density vs. time for different media AHL concentrations. II) Cellular AHL concentration vs. time for different exogenous AHL concentrations. III) Oscillatory period as a function of the exogenous AHL concentration. (B) Representative data used to create lysis dose response curves shown in Figure 3C and 3D. I) Lysis magnitude was calculated as the change in culture optical density (OD) during a lysis phase (L) divided by the change in OD during a growth phase (G). Light red vertical bar represents time point when 2 μ L of a 100X AHL stock was spiked into each culture well to achieve the desired AHL concentration. II) Representative growth and lysis curves used to construct the dose-response curves shown in Figure 3 for the pSpSLC₁₀ strain RBS. III) Representative growth and lysis curves used to construct the dose-response curves shown in Figure 3 for the pSpSLC₀ strain RBS. (C) Modeling the effect of lysis strength on GFP expression in the SLC. I) Normalized peak amplitude of cell density, cellular AHL, and cellular GFP for varying values of the model parameter D , the max death rate due to lysis. II) Peak GFP intensity as a function of D for varying threshold AHL values needed to trigger GFP expression, GFP_{Th} .

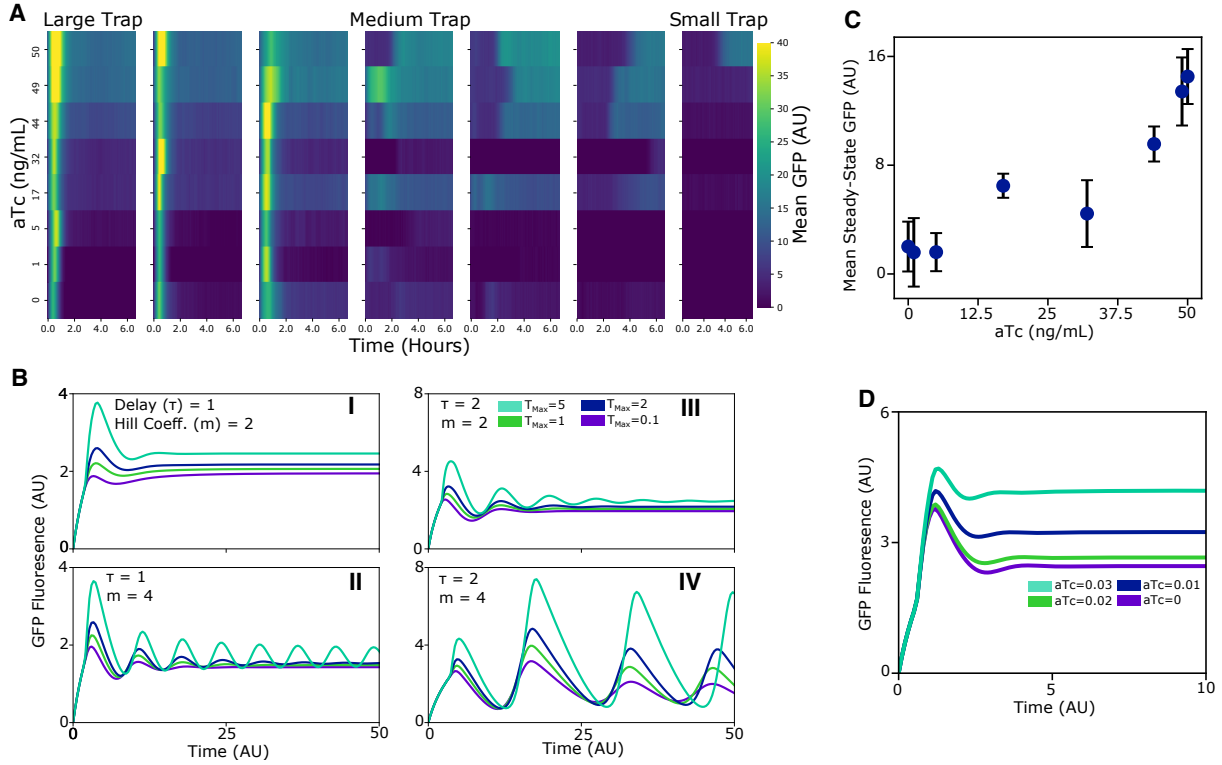


Figure 2.8: Analysis of P2N2-Tet Oscillator Circuit Design (Supplementary data related to Figure 1.5) (A) Heatmap showing representative mean GFP time traces for the original implementation of the P2N2-Tet oscillator design grown in a microfluidic device with variable trap sizes and aTc concentrations. Cell trap sizes ranged from $1.0 \times 10^{-2} mm^2$ (Large Trap) to $0.16 \times 10^{-2} mm^2$ (Small Trap). Color scale is linear and represents mean trap GFP signal (AU). (B) Modeling results for the P2N1-Tet circuit design with varying TetR expression levels (T_{Max}) for different values of the model delay parameter, τ , and the TetR repression Hill coefficient, m . I) $\tau = 1, m = 2$ II) $\tau = 1, m = 4$ III) $\tau = 2, m = 2$ IV) $\tau = 2, m = 4$. (C) Mean steady-state GFP for P2N1-Tet circuit in microfluidics for varying aTc concentrations. Error-bars represent standard deviation of 8 distinct cell traps from the four largest trap sizes pooled together. (D) Modeling results showing the impact of aTc on P2N1-Tet circuit dynamics. aTc concentrations are in arbitrary units.

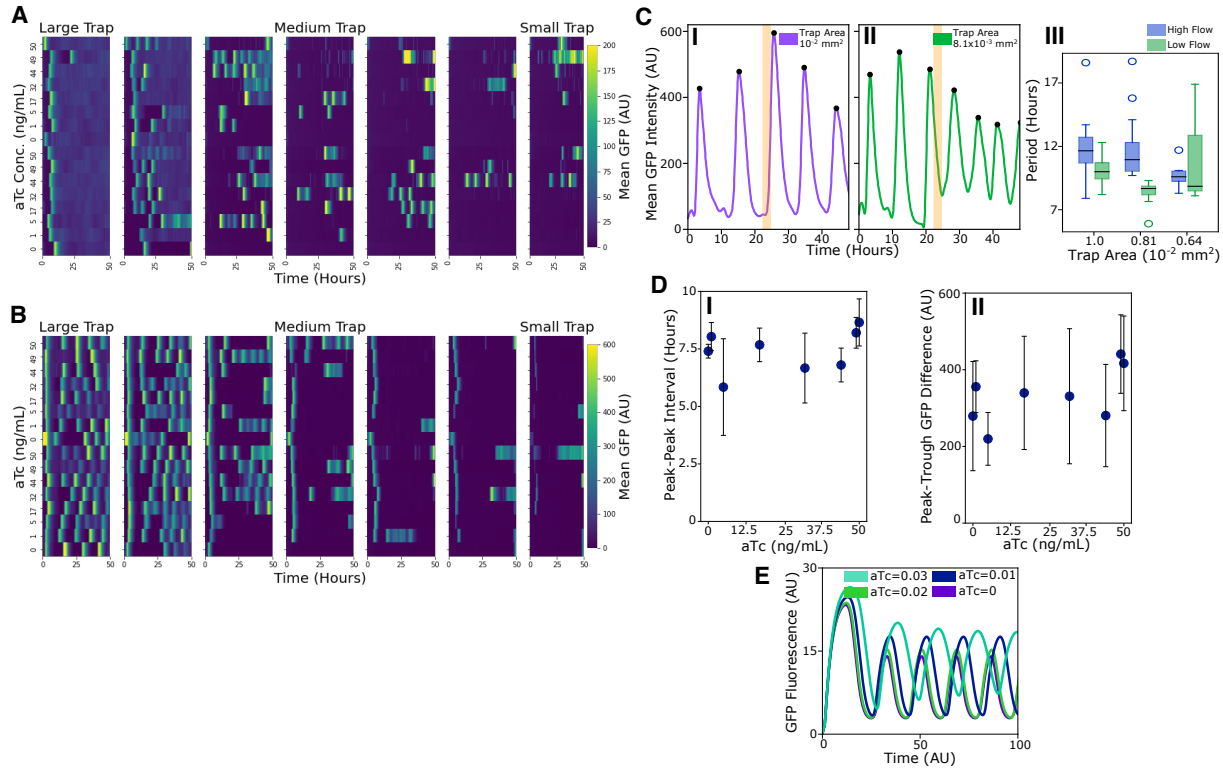


Figure 2.9: Analysis of P2N2-Tet Design (Supplementary data related to Figures 2.5 and 2.6) (A) Full single strain microfluidic data set for the original implementation of the P2N1-Tet synchronized oscillator. Cell trap sizes ranged from $1.0 \times 10^{-2} \text{mm}^2$ (Large Trap) to $0.16 \times 10^{-2} \text{mm}^2$ (Small Trap). Color scale is linear and represents mean trap GFP signal (AU). (B) Full single strain microfluidic data set for the P2N1-Tet synchronized oscillator library strain D1. Cell trap sizes ranged from $1.0 \times 10^{-2} \text{mm}^2$ (Large Trap) to $0.16 \times 10^{-2} \text{mm}^2$ (Small Trap). Color scale is linear and represents mean trap GFP signal (AU). (C) The D1 P2N1-Tet strain oscillates with different frequencies based on trap size and flow rate. I, II) Representative time traces of oscillator GFP dynamics in two different cell trap sizes. Light red vertical bars indicate time point where the hydrostatic pressure driving flow was reduced from 10 to 6 inches of H_2O . III) Boxplot showing changes in period of oscillations for three different trap sizes at high and low flow rates corresponding to hydrostatic pressures of 10 and 6 inches of H_2O respectively. Box extends from first to third quartile of data and whiskers extend 1.5x the interquartile range. (D) The oscillatory properties of the P2N1-Tet strain D1 are unaffected by aTc concentrations up to 50ng/mL. I) Representative scatter plot showing mean peak-peak interval for different aTc concentrations for strain D1. Data are for the second largest trap size ($0.81 \times 10^{-2} \text{mm}^2$) under the low flow condition referred to in panel B (6 inches of H_2O). For each concentration, error bars represent standard deviation of all measured peak-peak pairs across two replicate cell traps. II) Representative scatter plot showing mean peak-trough GFP difference for varying aTc concentrations for strain D1. Data are for the second largest trap size ($0.81 \times 10^{-2} \text{mm}^2$) under the low flow condition referred to in panel B (6 inches of H_2O). For each concentration, error bars represent standard deviation of all measured peak-trough pairs across two replicate cell traps. (E) Modeling results showing the predicted impact of aTc on P2N1-Tet circuit dynamics. aTc concentrations are in arbitrary units.

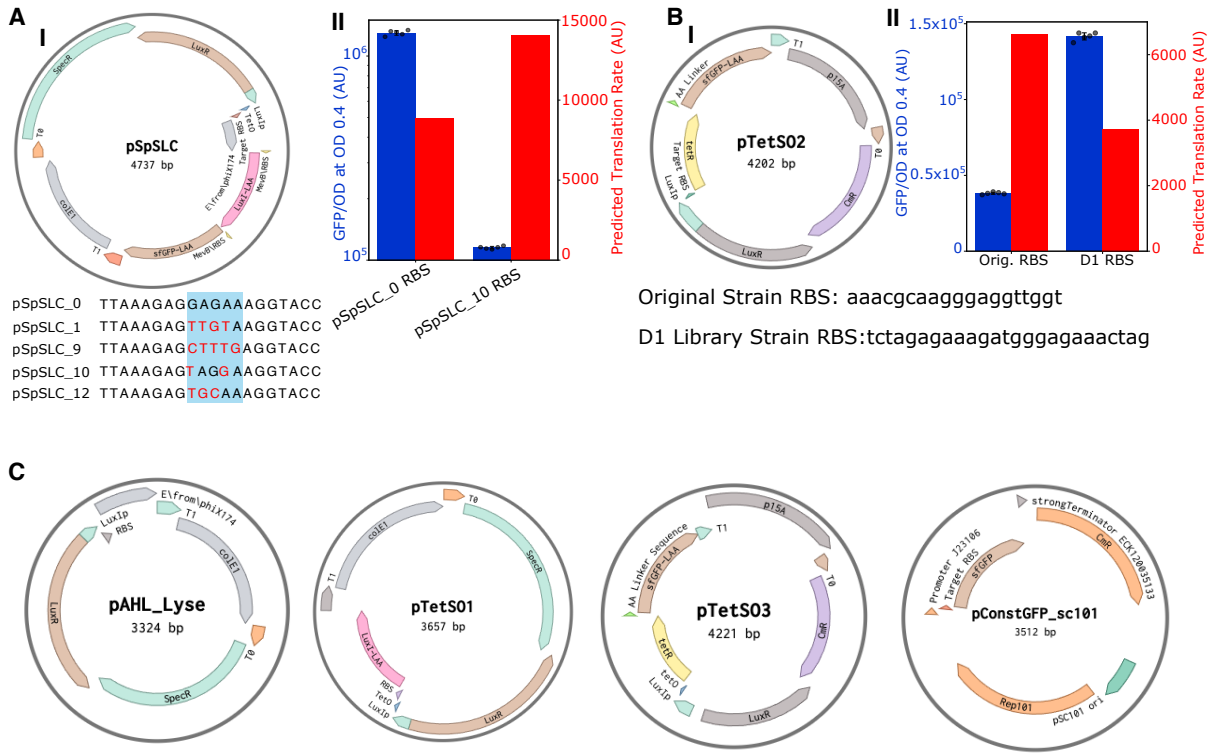


Figure 2.10: Plasmids Used in this Study and Sequenced RBS Variants (Supplementary data related to Figures 2.4 and 2.6 (and throughout)) (A) I) Plasmid map for the synchronized lysis circuit (SLC) used in this study with lysis gene RBS sequences for selected library strains shown below. II) Comparison of experimental (blue) and RBS calculator predicted (red) expression strengths for the pSpSLC₀ and pSpSLC₁₀ RBS sequences driving constitutive GFP expression in the plasmid pConstGFP_sc101 shown in panel C. For experimental data, bar heights represents mean and error bars represent standard deviation of 5 independent cultures (individual data points are plotted with bar graph). (B) I) Plasmid map for the negative feedback plasmid used in the P2N1-Tet oscillator circuit design with TetR-GFP RBS sequences for the original strain and strain D1 shown below. II) Comparison of experimental (blue) and RBS calculator predicted (red) expression strengths for the original and D1 P2N1-Tet TetR-GFP RBS sequences driving constitutive GFP expression in the plasmid pConstGFP_sc101 shown in panel C. For experimental data, bar heights represents mean and error bars represent standard deviation of 5 independent cultures (individual data points are plotted with bar graph). (C) Plasmid maps for remaining plasmids used in this study. pAHL_Lyase was used to construct lysis dose response curves shown in Figure 3. pTetS01 was the positive feedback plasmids for the P2N2-Tet and P2N1-Tet oscillator designs. pTetS03 was the negative feedback plasmid for the P2N2-Tet design. pConstGFP_sc101 was used for the experimental characterization of RBS strength shown in panels A and B.

2.6 Materials and Methods

2.6.1 Cloning and library creation for SLC strains

The original version of the single-plasmid synchronized lysis circuit (pSpSLC.0) was created by Gibson Assembly using PCR-amplified DNA sequences obtained from previously-existing lysis circuit plasmids developed in our lab. The plasmid sequence was confirmed with Sanger sequencing (Eton Bioscience, San Diego, CA). To generate a mutant library of the pSpSLC oscillator plasmid, 5 base pairs in the Shine-Dalgarno sequence of the ribosome binding site (located 7 to 12 base pairs upstream of the start codon of the lysis protein, E) were randomized by site directed mutagenesis. The original sequence at this position was: GAGAA. First, the entire plasmid was PCR amplified with the following degenerate primers where N indicates any base: 5' CATTAAAGAGNNNNNAGGTACCATGATGGTAC 3' and 5' AATTCTCTCTATCACTGATAG 3'. The PCR reaction mix was incubated with DPN1 at 37C for 30 minutes to digest template plasmid and then the 4.7 kb PCR product was run on an agarose gel and extracted using a QIAquick Gel Extraction Kit (QIAGEN). 1 μ L of the gel extracted PCR product was mixed with 0.5 μ L T4 ligase buffer, 0.5 μ L T4 PNK, and 3 μ L of DNase-free water and incubated at 37C. Next, 0.5 μ L T4 ligase buffer, 0.5 μ L T4 DNA ligase, and 4 μ L were added to the reaction mixture and the mixture was incubated at room temperature overnight. The following day, 50 μ L of chemically competent MG1655 E. coli cells were transformed with 3 μ L of the reaction mix and plated on an LB agar plate containing 0.2% glucose and spectinomycin. 24 colonies from the agar plate were randomly selected for mutant screening and grown up for 16 hours in LB media with 0.2% glucose and spectinomycin prior to use in experiments.

Cloning and library creation for TetR synchronized oscillator strains

Plasmids pTetSO1, pTetSO2, and pTetSO3 were created by Gibson Assembly using PCR-amplified DNA sequences obtained from previously-existing plasmids created in our lab.

Plasmid sequences were confirmed with Sanger sequencing (Eton Bioscience, San Diego, CA). To generate a mutant library of the two plasmid P2N1-Tet synchronized oscillator design, the RBS preceding TetR-GFP on the plasmid pTetSO2 was randomized to RBS sequences derived from an RBS library created by Professor Christopher Anderson [83]. Specifically, the entire plasmid was PCR amplified using Q5 DNA Polymerase with the following degenerate primers where N indicates any base: 5' NNGANNACTAGATGTCTAGATTAGATAAAAGTAAAG 3' and 5' NTCTTTCTCTAGAATTCGACTATAACAAACCATTTTC3'. Degenerate primers were ordered from Integrated DNA Technologies (IDT). A blunt-end ligation was performed to re-circularize the plasmid before co-transformation with plasmid pTetSO1 into MG1655 *E. coli* competent cells. The transformation was plated on LB agar containing chloramphenicol and spectinomycin and 48 colonies from the agar plate were randomly selected for mutant screening.

2.6.2 Microfluidic device development and fabrication

Our group has previously described the microfabrication techniques used to pattern SU-8 photoresist onto a silicon wafer to create the mold for our device [94]. A poly-dimethylsiloxane (PDMS) device was made from the wafer by mixing 77 grams of Sylgard 184 and pouring it on the wafer centered on a level 5"x5" glass plate surrounded with an aluminum foil seal. The degassed wafer and PDMS was cured on a flat surface for one hour at 95°C.

2.6.3 Multi-strain Microfluidic experimental protocol

For multi-strain microfluidic experiments, cells were grown overnight on LB+antibiotic media. Lysis oscillator strains were grown on LB supplemented with 0.2% glucose to suppress expression of the pLux promoter driving lysis. 45 μ L of each cultured strain were transferred to its own well in a 384 Echo compatible plate for direct transfer onto microfluidic devices. A PDMS device cleaned with 70% Ethanol and adhesive tape was aligned to a custom fixture

compatible with the Labcyte Echo. Both the fixture and a clean 4"x3" glass slide sonicated with 2% Helmanex III were exposed to oxygen plasma. 2.5 nL of each strain were deposited from the 384 Echo compatible plate directly onto each PDMS device. The device and glass slide were bonded together and cured at 37°C for two hours. Before setting up a microfluidic experiment, the device was placed in a vacuum for a minimum of 20 minutes. The device was then mounted onto the custom optical enclosure. The inlet port was connected to a 50 mL syringe and tygon tubing with LB media with antibiotic (spectinomycin for SLC oscillator strains, chloramphenicol and spectinomycin for tetR-GFP synchronized oscillator strains), and 0.075% Tween-20. The waste port was connected to tygon tubing and a 1L waste bottle. The height difference between the inlet and outlet was 20" corresponding to a flow rate of approximately 1 mL/hr. Tween-20 was used in the media as a surfactant to reduce clogging and therefore increase the longevity of microfluidic experiments. Tween-20 has been used by our group in many experiments without an adverse effect on *E. coli* [25, 94]. Microfluidic experiments were performed on a custom optical enclosure or on a Nikon TE2000-U epifluorescent inverted microscope (Nikon Instruments Inc., Tokyo, Japan). Cells were grown on the device on LB media with the appropriate antibiotics, and 0.075% Tween-20 until traps were filled to confluence. Extracted fluorescence time series were normalized to remove device background fluorescence and strain background fluorescence.

2.6.4 AHL induction protocol in SLC microfluidic experiments

For AHL inductions, LB with the predetermined AHL concentration was mixed and pipetted into the source media syringe. For periods where the same AHL concentration was left on the device for over 24 hours, the media was pipetted out of the syringe and replaced every 12 hours.

2.6.5 Live-cell imaging and data extraction for SLC library experiments

Microfluidic devices were imaged in a custom optical enclosure continuously every ten minutes in both the transmitted light and GFP fluorescence channels with a 1 second and 60 second exposure respectively. The custom optical enclosure uses an SBIG STX-16803 CCD Camera with a custom lens stack assembly containing the Semrock FF01-466/40-32-D-EB and FF02-520/28-50-D-EB excitation and emission filters, respectively. The enclosure has green and blue LED spotlight sources obtained from ProPhotonix for transmitted light and fluorescence light sources, respectively. The optical resolution of the enclosure is 36 μm . The enclosure was temperature controlled to 37°C.

Images were synced from the enclosure to a server via WiFi for further data processing. Custom software produced flat-field-corrected images in both channels in real-time to remove optical vignetting using the following equation:

$$C = m * \frac{R - D}{F' - D'} \quad (2.1)$$

where R is the raw image to be flat-field corrected, D is the dark-current image for that device, taken at the same exposure settings as R , F' is a raw image taken by the camera with no device present, D' is the dark-current image taken at same exposure as F' , m is the mean value for all values in the array $(F' - D')$, and C is the resulting corrected image.

Flat-field corrected images were then processed in ImageJ, where a custom "Region Of Interest" or ROI manager was used to extract fluorescence, transmitted light, and background values.

Data was initially processed by subtracting the local background signal, in order to eliminate any local or regional fluctuations that are of an additive (or, analogously, subtractive) nature. The result of this background correction was to produce a vector \vec{x}_t representing the background-corrected fluorescent signals of all cell traps at time t :

$$x_{(t, s_i)} = x_{(t, s_i)}^{trap} - x_{(t, s_i)}^{background} \quad (2.2)$$

where t refers to the current time point, s_i refers to the strain in cell trap i , $x_{(t, s_i)}^{trap}$ is the flat-field corrected fluorescent signal from the *trap* of position i at time t , and $x_{(t, s_i)}^{background}$ refers to the flat-field corrected local background fluorescent signal at position i at time t .

Once extracted, period and peak analysis was performed on fluorescence traces using the `find_peaks` function in the `scipy` signal processing toolbox, filtering for peaks with a minimum prominence of 10 (arbitrary fluorescence units).

Single strain microfluidic device loading and bonding

For the single-strain microfluidic experiments, a previously-developed PDMS device with variable cell trap sizes and a concentration gradient generator was used [17]. Prior to cell loading, the device was placed in a vacuum chamber for 30 minutes. During this period, 1mL of an overnight culture of the engineered strain was spun down and concentrated in 10 μ L of LB media with 0.075% tween. Immediately following removal from the chamber, the cell suspension was pipetted to cover the outlet of the device and sterile LB media + 0.075% tween was pipetted to cover the two inlet ports. After media and cells were pulled into the microfluidic chip by the vacuum and the cell traps had filled with cells, two inlet syringes with fluidic tubing attached were connected to the inlet ports of the device. Similarly an outlet syringe with tubing was connected to the outlet port of the device. All of the cell traps had the same width (100 μ m) and height (1.2 μ m) and ranged in length from 40 to 100 μ m. Media flow was maintained across the device by maintaining the source syringes 5-10 inches above the outlet syringe fluid height. For experiments using anhydrotetracycline (aTc), one inlet syringe was prepared with a concentration of 50ng/mL aTc in LB while the other syringe was prepared with 0ng/mL aTc leading to a gradient of 8 different aTc concentrations across the device.

2.6.6 Generation of lysis dose-response curves

To generate the lysis dose-response curves shown in Figure 3, 200 μ L cultures of the strains containing the plasmid pAHL_Lyse were started by seeding cells from a saturated culture at a 1:100 ratio in LB media. The cultures were grown at 37C and optical density was monitored every five minutes using a TECAN microplate reader with orbital shaking. Once the cultures reached early exponential phase (OD 0.2-0.3), the well plate was quickly removed from the microplate reader and each culture well was spiked with 2 μ L of a 100X AHL stock to achieve the desired final concentration. The well plate was then re-inserted into the microplate reader and the cultures were grown for 12 hours.

To calculate a lysis magnitude value from each condition, the growth curve for that condition was examined for an inflection point where the derivative of the culture OD with respect to time changed from positive to negative. Then, lysis magnitude was calculated as L/G, where G is the positive change in OD from the initial time point to the inflection point and L is the negative change in OD from the inflection point to the time point at which OD was lowest following the inflection point (SI Fig. 2B). A dose response curve was generated with the lysis magnitude vs. AHL concentration data by fitting the data to the Hill Equation.

2.6.7 Calculation of damping coefficients

To calculate the damping coefficients (b) presented in Figure 5b for the original P2N1-Tet strain and strain D1 in the multistrain microfluidic device, the following equation was fit to the mean GFP intensity for a given cell trap using the curve_fit function in the SciPy python library:

$$GFP(t) = Ae^{(-b*t)}.$$

2.6.8 Peak detection for comparison of P2N1-Tet strains

To compare the percentage of traps with oscillations between the original P2N1-Tet strain and strain D1 (Figure 4D), 50 hours of single strain microfluidic data for both strains was analyzed for peaks using the `find_peaks` function in the SciPy python library. To account for the differences in amplitude between the two oscillators, the height threshold in the peak finding script was changed for analysis of the two strains.

2.6.9 Data analysis of multi-strain microfluidic transmitted-light image stacks

To calculate the normalized cell density vs. time plots shown in Figure 3 using 10x transmitted light (TL) microscope images, the following protocol was used. First, the mean TL pixel value for each trap (TL_{trap}) was extracted in ImageJ along with a the mean pixel value for a selection of equal size on a part of the chip containing no cells (TL_{BG}). To obtain an approximate cell density from these two measurements, the following formula was used: $CellDensity = \text{Log}(1 + \frac{TL_{BG}}{TL_{trap}})$. Lastly, for each trap the approximate cell density was normalized as: $NormalizedCD = \frac{CD - \min(CD)}{\max(CD) - \min(CD)}$

2.6.10 Analysis of single strain microfluidic data

To analyze the 10x image stacks obtained from time-lapse microscopy experiments with the TetR-GFP synchronized oscillator strains, the mean GFP pixel intensity from each image was extracted using imageJ for each trap size and inducer concentration. The data shown in SI Fig. 4A and 4B represent the mean, background-subtracted GFP data for two separate microfluidic experiments. To calculate the average oscillatory period for the D1 oscillator for different conditions (SI Fig. 4C), cell traps were chosen that had at least two distinct peaks in mean GFP expression for each flow rate and trap size combination. The period for each cell trap that was

included in the data analysis was calculated as the mean time elapsed between each peak divided by the number of GFP peaks. The bar plot in SI Fig. 4C was created by taking the mean period for each flow rate and trap combination and the error bars represent the standard deviation among analyzed cell traps.

2.6.11 Theoretical RBS translation rate prediction with RBS Calculator

2.0

To estimate the relative translation initiation rates for specific RBS sequences from the different mutant libraries (SI Fig. 5A and B), Version 2.1 of the RBS calculator developed by Salis et al. was used (https://salislab.net/software/predict_rbs_calculator) [73]. Specifically, the full mRNA sequence (including the 5' non-coding region and the downstream coding sequence) were input into the RBS Calculator's prediction function. The values reported in the results and shown in the bar charts of SI Fig. 5A and B represent the predicted translation initiation rate (AU) for the start codon of the relevant gene.

2.6.12 Experimental characterization of selected RBS sequences in constitutive GFP expressing circuit

To experimentally determine the relative expression strength for specific RBS sequences from the different mutant libraries (SI Fig. 5A and B), these RBS sequences were cloned in front of a GFP gene driven by a constitutively active promoter. After verifying the resultant strains by sequencing, each strain was grown in LB media in a 96-well plate and GFP was monitored over time using a TECAN microplate reader. The values shown in the bar chart of SI Fig. 5A and B represent the mean GFP/OD value (n=5) for each strain when the strain was in an exponential growth phase at an OD of 0.4.

2.6.13 Deterministic modeling of Synchronized Lysis Circuit dynamics

For all modeling of the SLC, we used a modified version of a previously-published deterministic model of SLC dynamics [71]. This simple model consists of two differential equations, one that describes the production and dilution of the quorum sensing molecule AHL (Equation 2.3) and one that describes cell growth and lysis-induced cell death (Equation 2.4). We added an additional ODE to this model to directly account for AHL-induced GFP production (Equation 2.5). To model the effect of exogenous AHL on circuit dynamics (SI Fig. 2A), we modified equation 2.3 so that the value of AHL at any given time-point ($AHL(t)$) was not allowed to decrease below some set point AHL_{min} . We did not explicitly include a delay term in the SLC model that accounts for delays in transcription and translation of LuxI relative to the rapid binding of the AHL-LuxR complex to the pLux promoter. This choice was made because the cellular growth and lysis dynamics accounted for by the model occur on a much slower time scale than delays in gene expression making inclusion of a delay term in the hill function for LuxR-AHL binding unnecessary to predict circuit dynamics. All model results were obtained in MATLAB using the ode45 function. The following parameters were used in the SLC model simulations except where noted: $K = 2, D_{lysis} = 5, A_0 = 0.4, A_{max} = 8, AHL_{th} = 1, m = 4, A_{deg} = 1, G_{max} = 8, G_{deg} = 1, GFP_{th} = 3$

$$\frac{dAHL}{dt} = (A_0 + A_{max}F_A(AHL))n(t) - A_{deg}AHL(t) \quad (2.3)$$

$$\frac{dn}{dt} = Kn(t) - F_A(AHL)D_{lysis}n(t) \quad (2.4)$$

$$\frac{dGFP}{dt} = G_{max}F_G(AHL) - G_{deg}GFP(t) \quad (2.5)$$

$$F_A(AHL) = \frac{AHL(t)^m}{AHL_{th}^m + AHL(t)^m} \quad (2.6)$$

$$F_G(AHL) = \frac{AHL(t)^m}{GFP_{th}^m + AHL(t)^m} \quad (2.7)$$

2.6.14 Deterministic modeling of tetR-GFP Synchronized Oscillator dynamics

To model the behavior of the P2N1-Tet synchronized oscillator design, we used a delayed, ordinary differential equation model loosely based off a previous model of a similar synchronized oscillator [78]. The model consists of two main equations describing the production and degradation of AHL (Equation 2.8) and TetR (Equation 2.9). Equation 2.8 takes into account that both the basal and maximal production rates of AHL are affected by TetR repression while basal AHL production leads to additional AHL production in an auto-catalytic positive feedback loop. Equation 2.9 takes into account that TetR expression is only impacted by AHL in the P2N1 design. To model the P2N2 design of the circuit, we replaced equation 2.9 with equation 2.10 to account for TetR negative autoregulation. In the model, the degradation terms for both AHL and TetR represent that both proteins are actively degraded by the same protease (ClpXP) via Michaelis-Menten kinetics. To account for delays in the transcription, translation, and production of AHL and TetR relative to their rapid binding to transcription factors or operator sites, we include a delay term (τ) in the hill functions for AHL and TetR (Equations 2.12 and 2.13). For modeling results looking at the impact of aTc (SI Fig. 3D and 4E), we added a differential equation describing the binding of aTc to TetR (Equation 2.11). Since, aTc effectively prevents TetR from binding and repressing the pLuxTet promoter, we accounted for the effect of aTc in the hill function for TetR binding (Equation 2.12). All model results were obtained in MATLAB using the delayed differential equation solver, solveDDE. The following parameters were used in all of the synchronized oscillator model simulations except where noted: $A_0 = 5, T_0 = 2, A_{Max} = 30, T_{Max} = 5, AHL_{th} = 1, tetR_{th} = 1, m = 2, n = 4, A_{deg} = 1, T_{deg} = 1, f_{deg} = 0.1, \tau = 1, aTc = 0, K_c = 1000, K_d = 1$

$$\frac{dAHL}{dt} = A_0F(tetR) + A_{max}F(AHL)F(tetR) - \frac{A_{deg}AHL(t)}{1 + f_{deg}(AHL(t) + tetR(t))} \quad (2.8)$$

$$\frac{dtetR}{dt} = T_0 + T_{max}F(AHL) - \frac{T_{deg}AHL(t)}{1 + f_{deg}(AHL(t) + tetR(t))} \quad (2.9)$$

$$\frac{dtetR}{dt} = T_0F(tetR) + T_{max}F(AHL)F(tetR) - \frac{T_{deg}AHL(t)}{1 + f_{deg}(AHL(t) + tetR(t))} \quad (2.10)$$

$$\frac{dtetRaTc}{dt} = K_c[aTc]^2(tetR(t) - tetRaTc(t)) - K_d tetRaTc(t) \quad (2.11)$$

$$F(tetR) = \frac{1}{1 + \left(\frac{tetR(t-\tau) - tetRaTc(t-\tau)}{tetR_{th}}\right)^m} \quad (2.12)$$

$$F(AHL) = \frac{AHL(t-\tau)^n}{AHL_{th}^n + AHL(t-\tau)^n} \quad (2.13)$$

2.7 Supplementary Videos

2.7.1 Supplementary Video 2.1 (related to Figure 2.4)

Representative time-lapse microscopy images for SLC strain pSpSLC₀ grown in the multi-strain microfluidic device.

2.7.2 Supplementary Video 2.2 (related to Figure 2.4)

Representative time-lapse microscopy images for SLC strain pSpSLC₁₀ grown in the multi-strain microfluidic device.

2.7.3 Supplementary Video 2.3 (related to Figure 2.6)

Representative time-lapse microscopy images for TetR oscillator strain D1 grown in the single strain microfluidic device with variable trap dimensions.

2.8 Acknowledgments

This chapter contains material originally published as: Lezia, Andrew*, Csicsery, Nicholas*, and Hasty, Jeff. "Design, mutate, screen: Multiplexed creation and arrayed screening of synchronized genetic clocks." *Cell Systems* 13, no. 5 (2022): 365-375. (*equal contribution) The dissertation author was one of the primary authors and researchers of this material.

Chapter 3

Screening of therapeutic libraries for cancer cell toxicity using synchronized cell lysis and developing regulation to increase lysis circuit stability

3.1 Abstract

Bacterial-based approaches for cancer therapy are blossoming due to the discovery of tumor-associated microbiota in virtually every type of cancer [70,95]. Many of these microbes are easy to engineer, making them excellent delivery vehicles for genetically encoded therapy. A landmark study from 2016 demonstrated that synchronized, bacterial cell lysis could be used as a mechanism to release genetically encoded cargo that killed cancer cells [13]. Releasing therapeutic molecules by cell lysis is desirable because it is applicable to a wide range of molecule types without the need to engineer specific secretion mechanisms [96]. Thus, there is a significant opportunity to use lysis triggered release of cancer therapeutics to screen libraries of different

candidate genes for their ability to inhibit cancer growth. Here we develop a work flow for constructing bacterial therapy libraries and screening them against cancer cells in a 3D co-culture model. We find multiple candidates for future study in animal models. Additionally, we develop circuitry to improve the stability of genetic circuits that rely on cell lysis for therapy release.

3.2 Introduction

As described in the introduction in chapter 1, engineered cell lysis enables therapeutic payloads from different molecular classes to be released from bacteria. While this is advantageous for *in vivo* applications, it also makes lysis-based release an ideal *in vitro* screening platform for many therapies. By simply inserting different therapeutic gene coding sequences into the lysis circuit plasmids, any therapeutic peptide can presumably be produced and released into the surroundings. Since, initial screening is done with *E. coli* which can be challenging to get to secrete proteins [97], lysis-based release can dramatically speed up the screening pipeline. It is important to note that many proteins derived from higher eukaryotes undergo extensive post-translational processing that may prevent their proper assembly when expressed in bacteria.

Recently, a bacteria-in-spheroid co-culture model (BSCC) was developed for screening bacterial-based cancer therapies [98]. In the BSCC model, bacteria are co-cultured with a nascent tumor-spheroid and the bacteria colonize the inside of the spheroid. After bacteria colonization, culture media containing a poorly diffusible antibiotic is added to the co-culture to prevent the rapid overgrowth of bacteria outside of the spheroid. After bacterial colonization and addition of antibiotics, the spheroid can be imaged continuously to track spheroid and bacteria growth as well as coarsely-tracking gene circuit dynamics via fluorescent reporters. Using this platform, Harimoto et al. were able to visualize the oscillatory dynamics of the SLC in tumor spheroids and screen multiple unique bacterial-produced therapeutics for their ability to inhibit spheroid growth. While this system was a significant advance in speeding up screening of lysis circuit therapies, it

has some challenges limiting its throughput. For instance, assessing therapeutic efficacy solely by looking at changes in spheroid size can be time intensive and may sometimes unreliably report cancer cell death without performing further biochemical assays.

Recently, in the cancer therapy field, focus has been placed on culturing mammalian cells in 3D environments with a relevant extracellular matrix where the cells behave differently than they do in 2D monolayers on culture plates [99]. Many research groups are working on tumor-on-a-chip platforms that seek to better mimic the *in vivo* behavior of cancer cells and key features of the tumor microenvironment. These platforms range in complexity and throughput and focus on re-creating hallmarks of tumor progression such as hypoxia, angiogenesis, and metastasis, and often include multiple cell types associated with the tumor microenvironment [100]. In this chapter, we utilize 3D-cancer cell culture in a fibrin matrix to improve the physiological relevance of the therapy screening results we obtain.

3.3 Results

3.3.1 Construction of Therapy Library

We sought to make a library of lysis circuit strains that expressed different therapy genes under the pLux promoter that also drives LuxI and the lysis gene, E. To do this, we first identified candidate toxin genes in the literature that were likely to kill cancer cells. We identified the following classes of proteins and peptides for therapeutic candidates: pore forming toxins (PFTs) from bacteria, bacteriocins (some of which have been shown to have anti-cancer properties), protein synthesis inhibitors from plants, pro-apoptotic peptides, enzymes, antibiotics, and other tumor growth inhibitors, some of which are derived from animals. Table 3.1 summarizes the different toxins we identified and includes literature sources describing the mechanism of action for the different toxins.

After identification of candidate therapy genes, we optimized their codons for expression

Table 3.1: Therapeutic genes with their origin, function, and citation

Therapeutic Gene	Origin	Function	Citation
Pyocin S2 (Psy2)	Bacterial (<i>P. aeruginosa</i>)	Bacteriocin	[101]
Alpha hemolysin (Hly)	Bacterial (<i>S. aureus</i>)	Pore-forming toxin	[102]
Diphtheria toxin (dt)	Bacterial (<i>Corynebacterium diphtheriae</i>)	Inhibits protein synthesis	[103]
p28	Bacterial (<i>P. aeruginosa</i>)	Impedes degradation of tumor suppressor gene p53	[104]
Hemolysin (hlyA)	Bacterial (<i>V. Cholerae</i>)	Pore-forming toxin	[105]
Exotoxin A (ExoA)	Bacterial (<i>P. aeruginosa</i>)	Induces apoptosis	[106]
Protective antigen and lethal factor (PA+LF)	Bacterial (<i>B. anthracis</i>)	Inhibits MAPK kinases	[107]
Colicin E1 (colE1)	Bacterial (<i>E. coli</i>)	Bacteriocin	[108]
Chlorotoxin (cltx)	Animal (<i>Leiurus quinquestriatus</i>)	Neurotoxin, prevents proliferation in glioma	[109]
Gelonin (gel)	Plant (<i>Gelonium multiflorum</i>)	Inhibits protein synthesis	[110]
Hemolysin E (HlyE* + control)	Bacterial (<i>E. coli</i>)	Pore-forming toxin	[111]
Teretoxin (Tv1)	Animal (<i>Terebra variegata</i>)	Neurotoxin	[112]
Gomesin	Animal (<i>Acanthoscurria gomesiana</i>)	Inhibits proliferation	[113]
Pardaxin P5	Animal (<i>P. marmoratus</i>)	Inhibits proliferation	[114]
Melittin	Animal (<i>Apis mellifera</i>)	Bee venom	[115]
Pardaxin-1	Animal (<i>P. pavoninus</i>)	Inhibits proliferation	[116]
Hemolysin BL (Hbl)	Bacterial (<i>Bacillus cereus</i>)	Membrane lytic toxin	[117]
Agkhipin	Animal (<i>Gloydus halys Pallas</i>)	Venom	[118]
bioactive cationic peptide (BCP-A)	Animal (Human)	Interferes with cancer cell membrane	[119]
FIMGPY	Animal (<i>Raja porosa</i>)	Induces apoptosis	[120]
Colombistatin	Animal (<i>Bothrops colombiensis</i>)	Disintegrin	[121]
BH3-interacting domain death agonist (BID)	Animal (Human)	Pro-apoptotic peptide	[122]
non-haemolytic enterotoxin (Nhe)	Bacterial (<i>Bacillus cereus</i>)	Pore-forming toxin	[123]

in *E. coli* and contracted the company GensScript to insert the desired therapy genes into one of the lysis circuit plasmids. The original SLC system is a two-plasmid system where one plasmid contains the activating components and a GFP reporter (pTD103LuxIsfGFP) and the other contains the lysis component (pZA35X174E). The candidate genes were incorporated into the lysis plasmid as in the original SLC study from 2016, and subsequently transformed into *E. coli* strain MG1655 [13]. The library constructs are thus represented by the general two-plasmid scheme shown below (Fig. 3.1).

3.3.2 Confirming lysis dynamics of different therapeutic strains

A batch-culture screen in 96-well plates for growth dynamics confirmed the lysis ability of the constructed strains (Fig. 3.2). We used the original 2-plasmid SLC, which does not have any added therapeutic proteins, as a control for this experiment. This strain was chosen as a control because it was characterized in the 2016 paper, and is known to produce oscillatory lysis dynamics over time. In Figure 3.2, growth curves for 6 representative library strains are shown

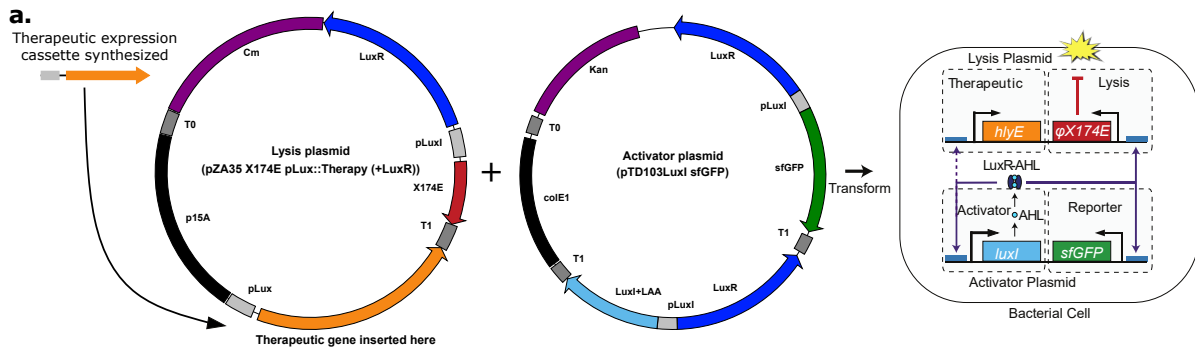


Figure 3.1: SLC therapy library construction pipeline: First, the prospective therapeutic genes are synthesized with the pLux promoter to produce the therapeutic expression cassette. Secondly, this cassette is inserted into the lysis plasmid via AvrII restriction sites. These are generated on the insert by overhangs on primers. Once the lysis/therapeutic plasmid is constructed, it can then be transformed into the bacterial strains of choice, along with the activator plasmid.

that were tested on the plate reader, along with the original 2-plasmid SLC as a control. The plate reader conditions tested were either media (LB) only or 100nM external AHL. External AHL was added as an inducer in case production of the prospective therapeutic affected the growth or metabolism of the strain such that circuit function is reduced. The LB media only cases were performed with three technical replicates (N=3) and the AHL cases were performed with two technical replicates (N=2).

We find that all of the transformed strains exhibit lysis behavior (Fig. 3.2b-g), similar to the original 2-plasmid SLC (Fig. 3.2a). Interestingly, some strains had a quorum threshold population level which was lower than the control, such as the strains containing Psy2, HlyA, and Hly. When AHL was added to the media, the result was generally a decreased quorum threshold, which was delayed in some cases (for HlyA and ExoA for example). We also measured the minimum slope of the growth curve to see if there were differences in the intensity of synchronized lysis between the different strains. We find that the control, DT, ExoA, and HlyA strains generally possess similar minimum slopes, whereas the rest of the strains were generally higher (Fig. 3.2h). For these strains (Gel, Hly, and Psy2), it may be that the expressed therapeutic affects the bacterial growth and/or metabolism, resulting in affected lysis dynamics.

While plate reader experiments are useful to provide information on the fundamental

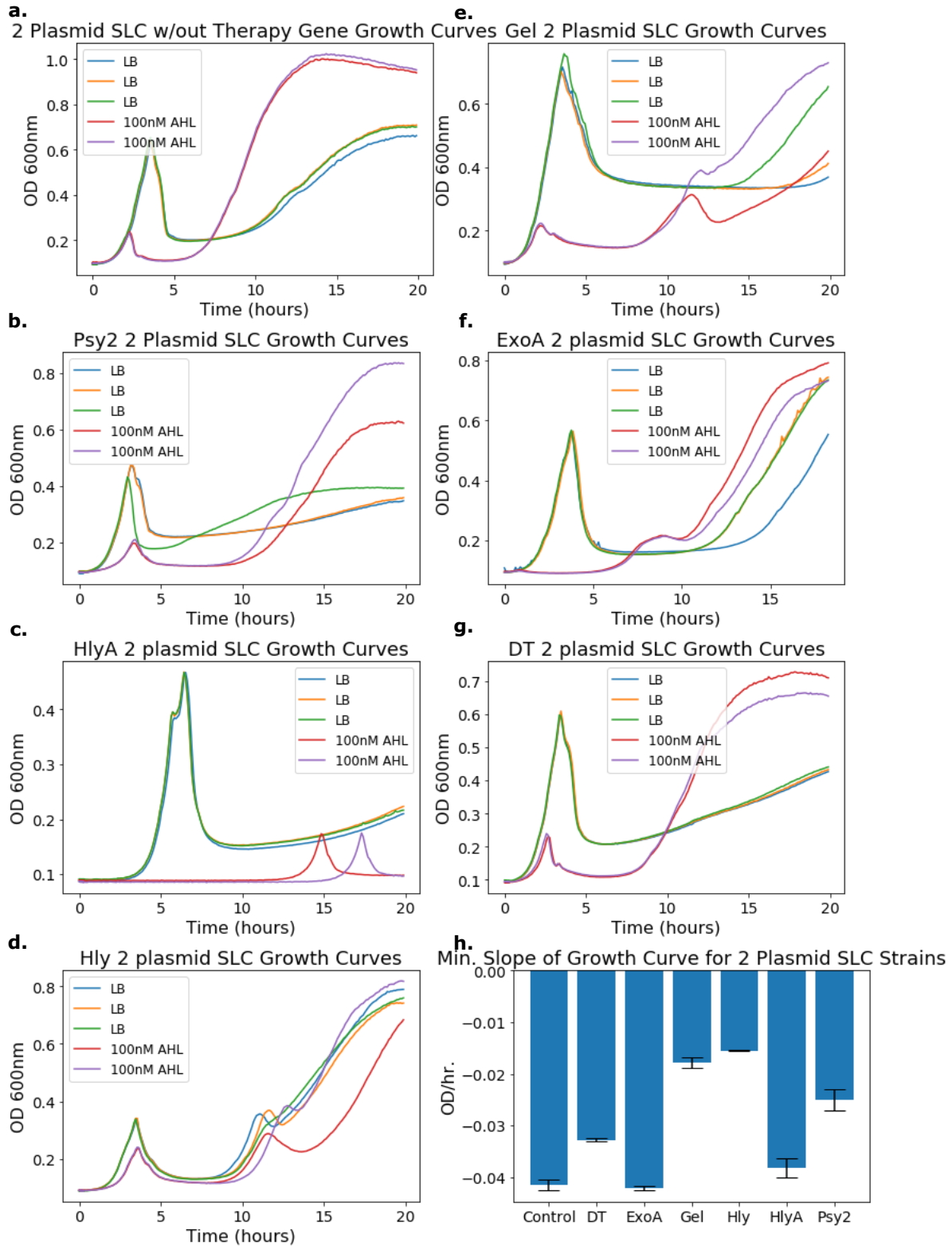


Figure 3.2: Plate reader data showing the growth and lysis ability of the library strains. All of these data were taken with the 2 plasmid SLC constructs. The strains included a control (a) with no therapeutic gene, psy2 (b), hlyA (c), hly (d), gel (e), exoA (f), and DT (g). (h) We also show the average minimum slope of these growth curves (error bars indicate standard deviation for N=3).

circuit characteristics of the SLC, growth and auto-activated lysis, continuous flow methods are needed to explore the dynamical behaviors of the circuit. While these experiments are considerably more time and labor intensive than the plate reader experiments, they provide valuable information about the properties of oscillations possible with the different SLC strains. We began by testing a small subset of the two-plasmid SLC library strains on the multi-strain microfluidic device introduced in Chapter 2. We find that all four of the different two-plasmid SLC constructs exhibit lysis oscillations: hlyE, hlyA, psy2, and DT (Figure 3.3). Interestingly, we do see some variability in the period of these circuits. In general, the strains exhibited oscillations where the period was generally longer in the beginning and then reached a more consistent value. It appears that the dynamics of all the strains converge over time. Future studies could be done to compare the values of these periods between strains in order to quantify any effects the expressed therapeutic has on the circuit.

3.3.3 Establishing a 3D co-culture screening platform

Following creation of the lysis circuit therapy library and confirmation of lysis dynamics, we wanted to screen the library of SLC bacteria for their potential to kill cancer cells. The ideal co-culture system bridges simple *in vitro* studies and more complex *in vivo* studies using murine cancer models and should recapitulate key features of the tumor microenvironment while remaining sufficiently high-throughput to efficiently screen many library strains.

We decided to culture cancer cells in a 3D extracellular matrix prior to co-culturing with bacterial library strains and measuring cancer cell death. After identifying an appropriate hydrogel component to create a 3D cancer cell culture, we implemented a screening platform to test the library strains. In this implementation, we set-up the 3D cancer cell culture on 96-well plates before adding the bacteria. We implemented this screening system by using simple readout for cancer cell viability (intracellular ATP).

Given previous success in making viable 3D cancer cell cultures using a fibrin matrix [124],

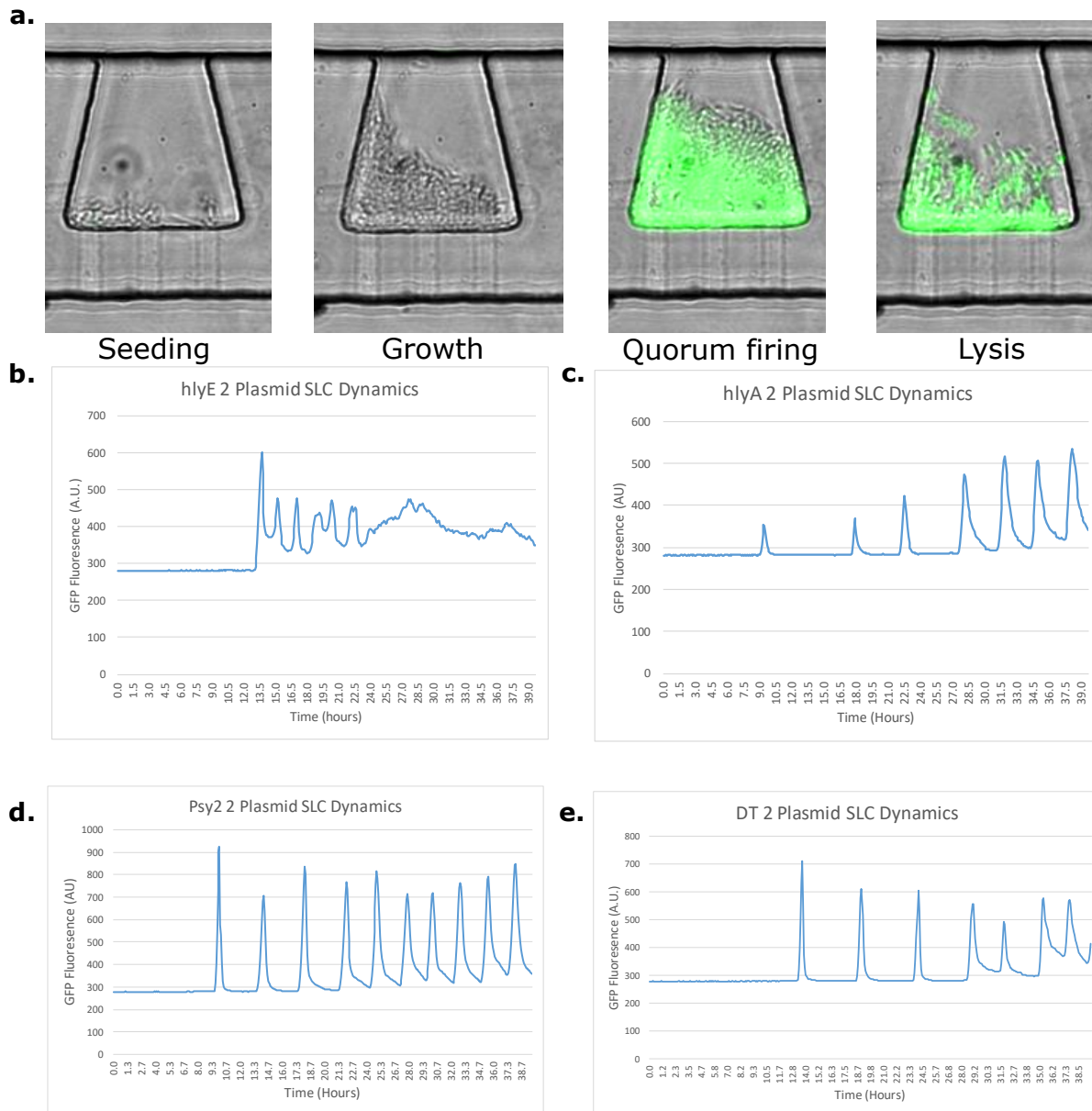


Figure 3.3: SLC library strain dynamics in a microfluidic device. (a) Images showing the different stages of SLC behavior in microfluidic bacterial growth chambers. The base of these chambers measure $70\mu\text{m}$, and the height in the z-axis is $4\mu\text{m}$. The GFP fluorescence from these strains indicates quorum activation, and GFP peaks correspond to lysis peaks. Fluorescence trajectories for hlyE (b), hlyA (c), psy2 (d), and DT (e) are shown.

we used this approach to begin screening our library. We grew 3D cancer cultures embedded in fibrin. Bacterial strains were then added to the co-culture (via suspension from liquid medium) and then incubated at 37C. We then used the 3D CellTiter Glo assay [125] to measure intracellular ATP levels as a proxy for cancer cell viability. A detailed protocol of this screening approach is included in the Methods section.

3.3.4 Library screening results

We performed a library screen with the strains shown in Table 3.1. We reported cell viability based on CellTiter glo assay results relative to a negative control strain containing the lysis circuit, but expressing no therapeutic (Figure 3.4). For strains with the same effect on the cancer cell culture as the SLC only strain, their relative viability should be 1 (i.e. no different than the viability of the negative control). Anything below 1 indicates that this strain has greater toxic effect on the cancer cell culture. Five SLC strains from the library were identified as having a greater toxic effect on the cancer cells, the strains expressing ExoA, HlyA, Hly, PA+LF, and DT. Further experiments were performed with a subset of these (ExoA, HlyA, Hly, and PA+LF) and the results were successfully replicated(Figure 3.4c).

Interestingly, all of effective candidates were bacterial toxins. Both Hly and HlyA are pore-forming toxins (PFTs), much like HlyE. ExoA and DT target components of protein synthesis, while PA+LF targets mitogen activated protein kinase kinases (MAPK kinases). The pore-forming toxins generally seem to have a greater effect on cancer cell viability, however, future experiments are needed to confirm this. In addition, some of these library strains had effects on the cancer cell culture that resulted in less toxicity against the cancer cells when compared with the negative SLC control strain. This may be due to these strains generally being less robust because of the extra protein production (either growth or metabolism may be affected). We believe that this hypothesis may be supported by previous experiments that we performed, where we have shown that therapeutic producing strains which had reduced growth rates and lysis thresholds

were generally ineffective against tumors *in vivo* [13].

3.3.5 Development of a repressible synchronized lysis circuit for improved growth stability in batch culture

A major goal of synthetic biology is to improve the stability of engineered genetic circuits for real-world applications such as chemical production and living therapeutics. Some strategies to improve the longevity of genetic circuits include: encoding burden-based feedback into genetic circuits [32], splitting circuit functions between different members of a cellular consortia [126], and creating “kill-switch” circuits that eliminate population members who have lost regular circuit function [127]. The synchronized lysis circuit is especially prone to failure due to mutation in larger culture sizes due to the intense selection pressure imposed by cycles of massive cell death. To extend the lifetime of this circuit in *E. coli*, Liao et al. utilized a three-strain system with rock-paper-scissor like interactions. In this system, when the SLC mutates or fails in one *E. coli* strain it can be replaced by a different SLC-containing strain that expresses a colicin to kill off the first strain [16]. While colicin-based strain cycling demonstrates a potential strategy to extend the lifetime of the SLC during therapeutic applications, mass-production of lysis circuit strains prior to use in an application requires a different strategy to avoid mutation.

In previous work with the SLC, unwanted lysis during strain cultivation was prevented by adding glucose to the culture media. The native pLux quorum sensing promoter from *V. fischeri* used in the SLC is activated in part by cyclic AMP (cAMP) via the cyclic AMP receptor protein (CRP) [128]. Thus, high levels of glucose, which lead to decreased levels of cellular cAMP decrease transcription from the pLux promoter. Despite this glucose-based catabolite repression of the SLC, significant lysis often occurs during initial grow-up of SLC strains prior to use in an experiment or application limiting the ability to efficiently cultivate large volumes of lysis circuit bacteria.

To improve the ability to turn lysis gene expression off from the pLux promoter during

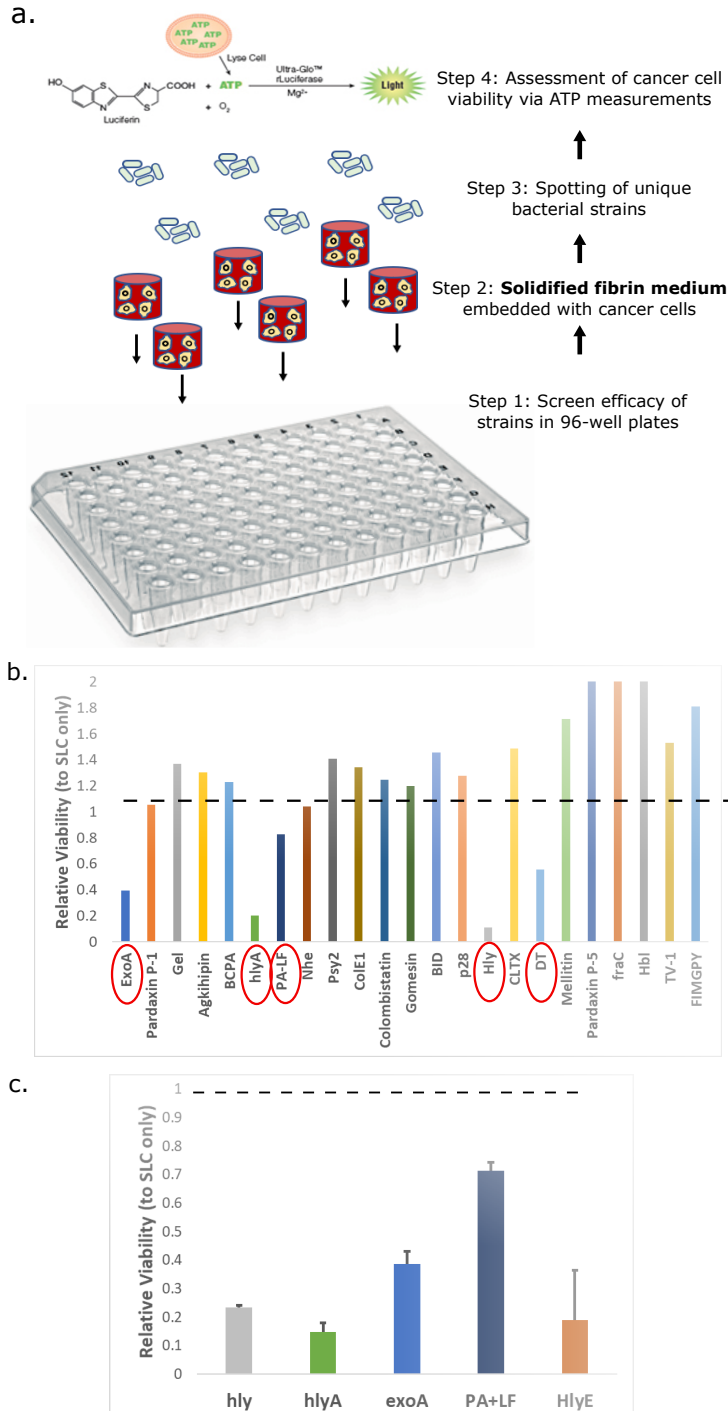


Figure 3.4: SLC therapy library co-culture screening results. (a) Overview of screening protocol (b) 3D HeLa cell culture viability results with the library strains from a. Library strains showing a greater effect on reducing cancer cell viability are circled in red. The dashed line represents the same viability as would be expected with the negative control strain (SLC only). (c) A follow-up experiment comparing the some of the candidates selected from b with the previously validated toxin and positive control, HlyE. Error bars represent standard error with N=3-4.

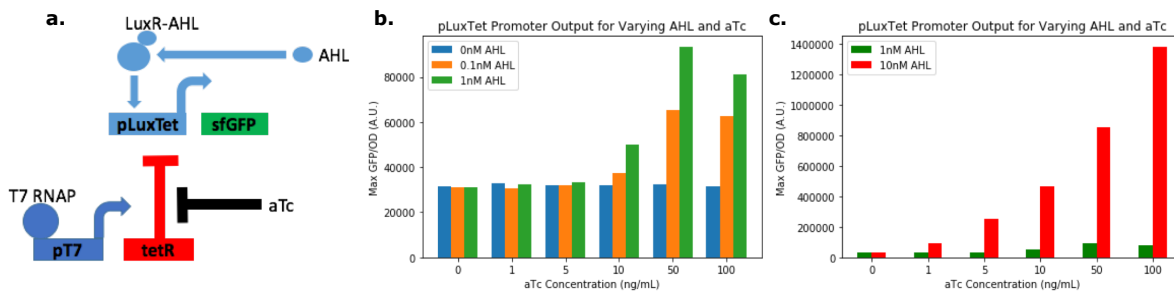


Figure 3.5: Characterization of hybrid pLuxTet promoter. (A) Diagram of genetic circuit used to test behavior of pLuxTet promoter. LuxR-AHL activates expression from the promoter while TetR represses transcription. aTc can activate the promoter in the presence of AHL by relieving repression from constitutive TetR repression. (B) Characterization of pLuxTet promoter output for different AHL (0-1nM) and aTc (0-100ng/mL) concentrations. (N=1) (C) Characterization of pLuxTet promoter for different AHL (1-10nM) and aTc (0-100ng/mL) concentrations. (N=1)

strain cultivation, we utilized a hybrid, repressible version of the pLux promoter. This promoter variant features a copy of the TetO operator sequence immediately following the pLux promoter allowing transcription to be turned off by expression of the tetracycline repressor protein (TetR). First, we verified that the hybrid pLuxTet promoter was repressed by TetR and activated by LuxR-AHL. To do this, we created one plasmid where the pLuxTet promoter drives expression of LuxR and sfGFP and another plasmid where TetR expression is driven by the T7 phage promoter and T7 RNA polymerase. Figure 3.5 demonstrates that the pLuxTet promoter is activated by LuxR-AHL like the wild-type pLux promoter, but only when anhydrotetracycline (aTc) is present which binds TetR and prevents TetR from repressing the promoter.

Next, we used the pLuxTet promoter to drive expression of LuxI, the lysis gene E and GFP in the SLC. We found that the strength of lysis in this circuit was able to be controlled by the addition of aTc and AHL, confirming that the TetR-repressible Lux promoter could be used as a tool to prevent leaky expression of cell lysis (Fig. 3.6).

For stable batch culture growth of the SLC, we wanted to have the ability to control repression of the lysis circuit with an exogenous inducer. To accomplish this, we placed the tetR gene under control of the arabinose-inducible pBAD promoter. In this system, the lysis circuit should be repressed in the presence of arabinose and function normally in the absence of

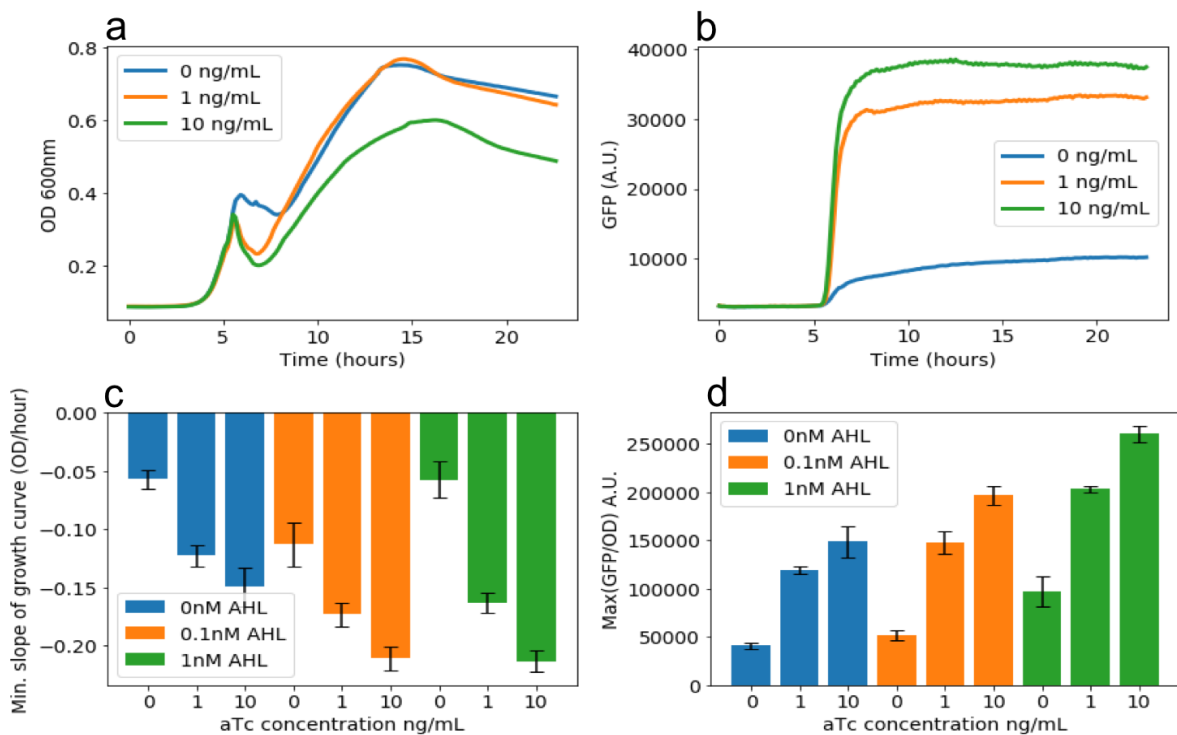


Figure 3.6: Characterization of a TetR-repressible lysis circuit in batch culture. (A) Representative growth curves for the circuit for different concentrations of aTc. (B) Representative GFP fluorescence trajectories over time for different concentrations of aTc. Here, GFP fluorescence represents the output from the pLuxTet promoter. (C) Bar chart showing the minimum slope of the growth curve for different combinations of aTc and AHL added to the culture media. The minimum slope of the growth curves is used as a measure of cellular lysis here. (N=3) (D) Bar chart showing the maximum value of GFP/OD for different combination of aTc and AHL added to the culture media. Here, GFP fluorescence represents the output from the pLuxTet promoter.

arabinose. When grown in batch culture, arabinose was able to successfully eliminate cell lysis. Specifically, an arabinose concentration of 0.05% was able to prevent lysis even when 10nM AHL was added to the culture media. (Fig. 3.7)

Having created a system where the repression of the SLC in batch culture could be controlled by the addition of arabinose to the culture media, we wanted to compare how the arabinose inducible repression of the SLC compared to catabolite repression due to glucose. We cultured a strain that contained the arabinose SLC as well as an extra copy of the LuxI positive feedback loop on a separate plasmid in both 0.2% glucose and 0.1% arabinose. We found that in this strong lysis circuit, 0.1% arabinose was much more effective at preventing lysis than 0.2% glucose as measured by the maximum negative slope of the growth curves (Fig. 3.8B and C).

Finally, to verify that arabinose inducible repression of the SLC preserved circuit function in long-term growth environments, we grew the strain in the presence of different concentrations of arabinose and then passaged this culture into media without arabinose. We found that initial growth of the strain in media without arabinose caused loss of circuit function when the strain was passaged while initial growth of the strain with 0.1% arabinose resulted in maintenance of circuit function (Fig. 3.8D). Together, these results demonstrate a potential strategy for cultivation of highly mutation prone circuits prior to use in applications.

3.4 Discussion

In this chapter, we demonstrated how lysis-based release of bacterial-produced proteins can enable rapid screening of different genes for cancer therapy. While we did identify some promising therapy candidates that were mostly from the class of pore-forming toxins, the majority of therapy strains in our library had little effect on cancer cell viability compared to a control. While most of the chosen therapy genes have at least some documented evidence of anti-cancer properties (Table 3.1), there are many potential reasons our initial library screen showed no

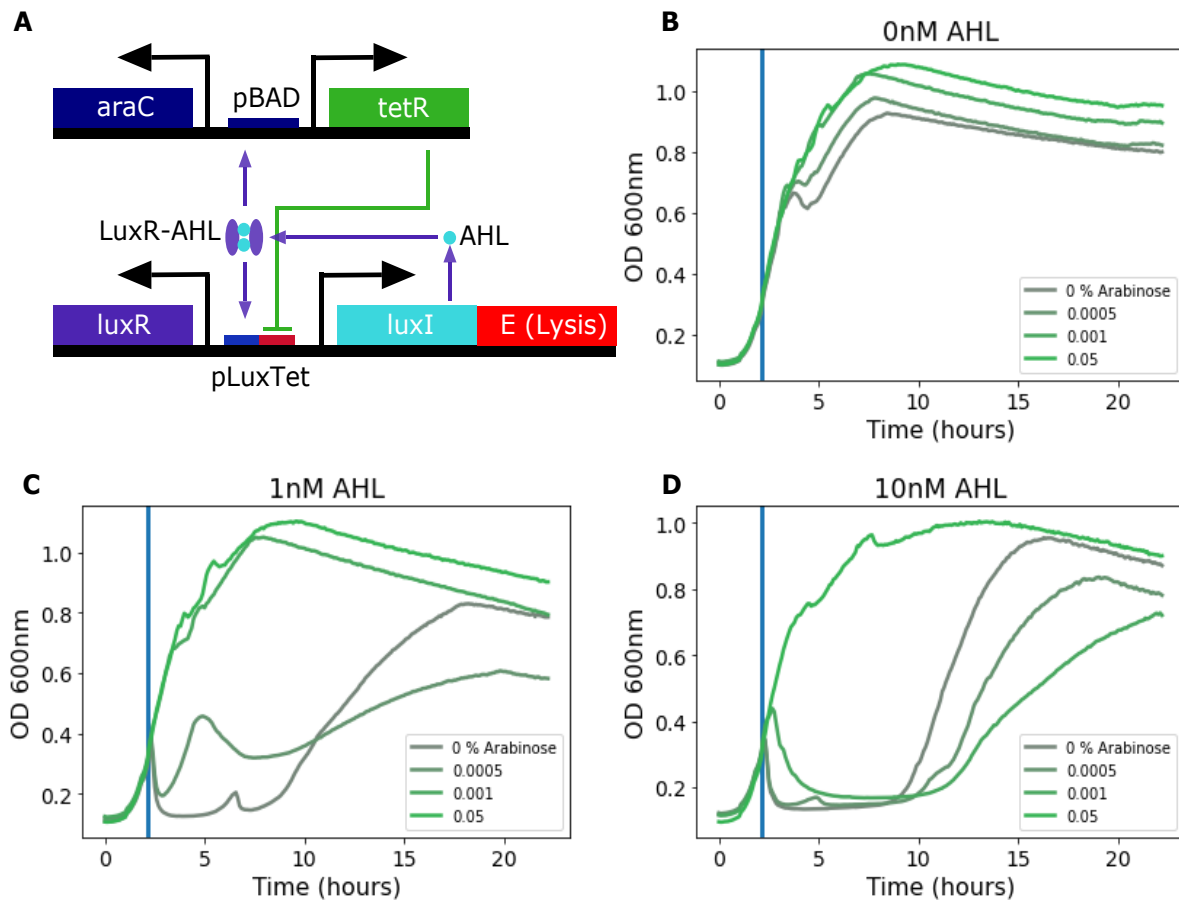


Figure 3.7: Control of lysis circuit repression with arabinose inducible TetR expression. (A) Circuit diagram of arabinose controllable repression of the lysis circuit. (B) Representative OD vs. time curves for varying concentrations of arabinose in the presence of 0nM AHL. Vertical blue bar indicates time at which AHL was added to the culture. (C) Representative OD vs. time curves for varying concentrations of arabinose in the presence of 1nM AHL. Vertical blue bar indicates time at which AHL was added to the culture. (D) Representative OD vs. time curves for varying concentrations of arabinose in the presence of 10nM AHL. Vertical blue bar indicates time at which AHL was added to the culture.

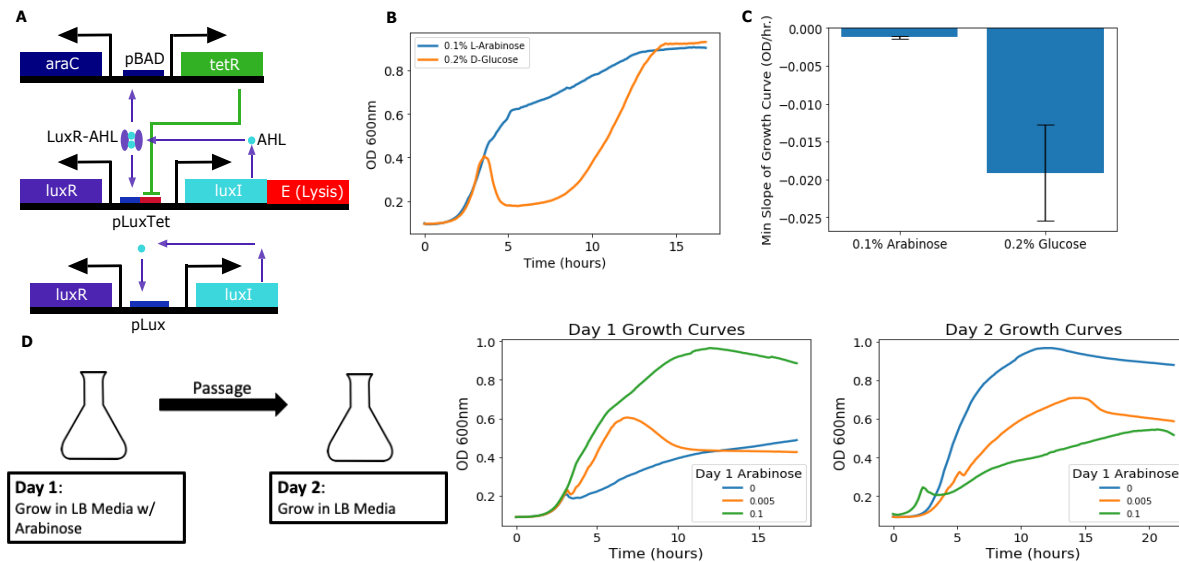


Figure 3.8: Improved lysis circuit stability with arabinose-based system. (A) Diagram of lysis circuit variant used to test long-term stability of arabinose-repressible lysis circuit. (B) Growth curves for the circuit shown in part A grown in LB media with either 0.2% glucose or 0.1% arabinose. (C) Minimum slope of growth curve for circuit grown in glucose vs. arabinose. Error bars represent standard deviation of 3 separate cultures. (D) Experiment showing that growing the circuit in arabinose media preserves lysis ability when passaged into media without arabinose. For cultures initially grown in the absence of arabinose, lysis function is lost.

efficacy. For one, many of the therapy genes that showed no effect were derived from animal or plant organisms. We tried to avoid choosing proteins that would require extensive post-translational modification, but it is possible that some of these proteins were not functional when expressed in *E. coli*. In future studies, it would be useful to do some basic characterization to ensure that *E. coli* is able to produce a functional version of the different proteins. At the same time, one of the advantages of using the cellular lysis platform for screening, is that it is easy to test new therapy candidates without spending a lot of time optimizing expression levels.

Another potential reason why the number of promising hits in our library screen was relatively small is that some of the therapeutic candidates might work on a longer time-scale than we measured here. For instance, in our screening experiments, HeLa cells were exposed to the therapeutic proteins and molecules for less than a day. For therapy candidates that work by slowing cancer cell proliferation (rather than triggering rapid cell-death like pore forming toxins do), the length of bacteria and cancer co-culture might be insufficient to see differences in cancer cell abundance between a therapy strain and the control. In future work, it would be interesting to see how longer co-culture periods affect which therapy strains perform better than the the control strain with no therapy gene.

A major challenge in scaling-up cell-based therapies for use in the real-world, is producing sufficient amounts of the therapeutic cells without the underlying genetic circuits they harbor breaking due to mutation. This problem is especially relevant to lysis-based therapies as engineered cell lysis poses an immense selective pressure for circuit mutation. Here, we showed how the use of a hybrid, repressible-inducible promoter can be used to turn off circuit function in the presence of one inducer (i.e. arabinose) enabling batch-production of the therapeutic strain. Due to the tight regulation and minimal leaky production of the lysis circuit repressor (TetR) from the pBAD promoter, the lysis circuit is unrepressed in the absence of arabinose and functions as expected. In future work, it would be interesting to try to scale up lysis strain production in large bioreactors to see if the regulatory circuit developed in this chapter is able to prevent circuit

mutation in larger populations.

3.5 Materials and Methods

3.5.1 Construction of lysis circuit toxin library

Genscript was contracted to help with cloning of toxin library plasmids. Specifically, they were supplied with the previously constructed pZA35X174E plasmid. They synthesized codon-optimized sequences of the relevant toxin genes and sub-cloned them into the pZA35X174E vector plasmid we supplied by standard restriction digest cloning. Upon receiving the therapy plasmids, they were co-transformed with the pTD103LuxIsfGFP plasmid into chemically competent MG1665 *E. coli* cells. The transformation was plated on LB agar plates supplement with Kan, Cm, and 0.2% glucose. Successful transformants were verified by Sanger sequencing.

3.5.2 Microfluidic culture of lysis circuit toxin library strains

To look at the lysis circuit dynamics of a subset of library strains in continuous culture, we used the multi-strain microfluidic device introduced in Chapter 2. Briefly, to load this device, overnight cultures of library strains were spotted to the device using the Labcyte Echo liquid handler. After devices were bonded, they were perfused with the relevant culture media and imaged continuously at 20X on a Nikon microscope. See Chapter 2 for more details on protocol for setting up the device.

3.5.3 3D HeLa Cell Culture in Fibrin Matrix

HeLa Cells (ATCC CCL-2) were grown in 35X10mm tissue culture dishes until 90% confluent. The cells were lifted, pelleted, and re-suspended in 10mL DMEM with 10% FBS, 1X kanamycin, and 1X chloramphenicol. A 3mL solution of fibrinogen was prepared in DPBS at

a concentration of 10mg/mL. Fibrinogen was incubated in a 37C water bath for 15-30 minutes until completely dissolved. The fibrinogen solution was then filtered through a 0.22uM syringe filter. Thrombin was prepared in milliQ H2O w/ 0.9% NaCl at a concentration of 100U/mL. 1uL aliquots of 100U/mL thrombin were prepared in small microcentrifuge tubes and kept on ice until needed. 1mL of the HeLa Cell suspension was mixed with 1mL of the fibrinogen solution. 50uL of the fibrinogen/HeLa cell solution was pipetted into one of the tubes containing 1uL thrombin. The fibrinogen cell mix and thrombin were quickly mixed by pipetting up and down 5 times. The mixture was then rapidly pipetted into a well on a 96-well plate. Care was taken to ensure the gel covered the entire well bottom and no bubbles were introduced. 30 wells in a 96-well plate were loaded with 50uL of HeLa cells suspended in a fibrin matrix. Then, the well plate was incubated in a 37C CO2 incubator for 30 minutes to allow fibrin to completely form a gel. After this, 200uL of 37C DMEM+FBS+Kan+Cm was gently pipertted on top of the fibrin gel in each well. DMEM was replaced every alternate day until cells were ready for co-culture with bacteria (about 1 week).

3.5.4 Bacteria HeLa Co-Culture and 3D Cell-Titer Glo Screening Assay

All lysis circuit library strains were grown overnight in 3mL cultures in LB media supplemented with kanamycin, chloramphenicol and 0.2% glucose. The following day, 2uL of each of these overnight cultures were used to seed separate 200uL cultures of each strain in different wells of a 96-well plate. The growth media was DMEM+FBS+Kan+Cm for the 200uL cultures. The 96-well plate was incubated in a Tecan Infinite M200 microplate reader with orbital shaking until the optical density at 600nm of each culture was around 0.2. These 0.2 OD600 cultures were used to inoculate different HeLa fibrin culture wells by adding 2uL of bacterial culture to the 200uL cancer cell culture. Before adding the bacteria to the HeLa wells, the media in the HeLa wells was replaced with fresh DMEM+FBS+Kan+Cm. The bacteria and cancer cell cultures were incubated at 37C for 12 hours. Then, the culture wells were washed 3-4 times with

DMEM+10%FBS+PenStrep. The well plate was then incubated at 37C for 1 hour. Following incubation, all media was removed from the wells and they were washed 3-4 times with 200uL of DPBS. After the final wash, 50uL of DPBS was left in the cancer cell wells. Then 50uL of 3D Cell Titer-Glo reagent was added to each well. The well plate was then incubated in the microplate reader with orbital shaking for 5 minutes to lyse the cancer cells and mix the reagent and culture together. The well plate was then left at room temperature for 20 minutes. Finally, 50uL from each well was transferred to a flat white-bottom Costar 96-well plate. Luminescence was measured on the microplate reader with a one second integration time.

3.5.5 Plate reader experiments to test lysis circuit function

For plate reader experiments looking at lysis capability of therapy library strains or repressible lysis circuit strains, overnight cultures of the specific strains were grown in LB with 0.2% glucose and the appropriate antibiotics for plasmid maintenance. The next day, 2uL of an overnight culture was used to start a 200uL culture in a 96-well plate. The cultures were then grown in a Tecan Microplate Reader for 24 hours with OD and GFP measurements taken every 5 minutes. The resulting growth curves and fluorescence curves were analyzed for the presence of lysis events and promoter induction.

3.6 Acknowledgments

This chapter contains unpublished material in preparation for publication as: M. Omar Din*, Andrew Lezia*, and Jeff, Hasty. “Screening of bacterial cancer therapy libraries in 3D co-culture” (*equal contribution) The dissertation author was one of the primary authors and researchers of this material.

Chapter 4

Exploiting heterogeneity in coupled, two plasmid systems for dynamic population adaptation

4.1 Abstract

In synthetic multi-plasmid systems, it is standard to use only plasmids with orthogonal replication mechanisms to avoid phenotypic heterogeneity and ensure plasmid stability. In nature, however, microbial populations actively exploit heterogeneity to survive in fluctuating environments. Here we show that the intentional use of distinct plasmids with identical origins of replication (oris) can help an engineered bacterial population adapt to its environment. We find that copy number coupling between distinct plasmids in such systems allows for copy number buffering of an essential, but high-burden construct through the action of a stably maintained, nonessential plasmid. Plasmid coupling also generates population state memory without additional layers of regulatory control. This work reimagines how we design synthetic populations to survive and adapt by strategically giving control back to the cells.

4.2 Introduction

Heterogeneous gene expression in cellular populations is typically viewed as a challenge to synthetic biologists striving for tight control of cellular phenotypes. While population variation can be an obstacle to engineering biology, it is pervasive in natural systems [129]. Whether driven by stochastic gene expression differences or environmental stress, living systems often strategically rely on heterogeneity to improve population survival via division of labor or bet-hedging. For example, in some biofilm forming species, more motile individuals focus on population expansion while others contribute to biofilm maintenance [130]. Additionally, some microbial populations utilize bet-hedging, a strategy where a sub-population of cells are more suited to a potential future environment at the cost of fitness in their current surroundings [131, 132]. Bet-hedging is commonly associated with spore-formation, carbon metabolism, and antibiotic persistence in bacterial populations [133]. Regardless of the mechanism, a fundamental benefit of population heterogeneity is increased adaptability to fluctuating environmental conditions [134]. The widespread use of heterogeneity in nature suggests that synthetic genetic circuits could exploit gene expression noise to adapt to different environmental conditions and carry out complex functions [135, 136].

One source of noise commonly encountered in synthetic biology is variation in plasmid copy number (CN). Until recently, plasmid CN was an overlooked regulation strategy for tuning genetic circuits. Now researchers have developed multiple ways to use plasmid CN for genetic circuits, including creating strain libraries that exhibit different CNs [137], designing plasmids whose CN can be tuned with small molecule inducers [138–140], and using engineered DNA cutting to dynamically change plasmid CN over time [77]. In this work, we intentionally engineer plasmid CN noise as a tool for synthetic gene circuits by exploiting overlapping plasmid replication mechanisms.

Plasmid CN is commonly controlled by built-in negative feedback loops that act to inhibit

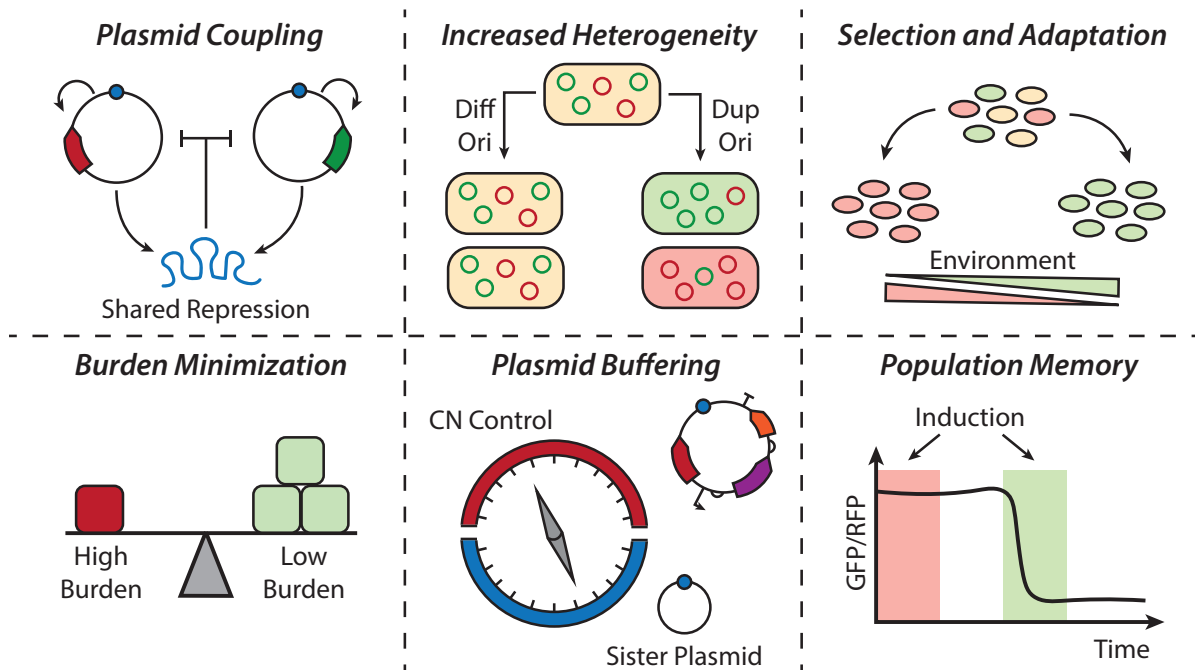


Figure 4.1: Two plasmids are coupled via shared copy number regulation mechanisms. This coupling leads to increased phenotypic heterogeneity in a population. Different cells are selected for in varied environments due to fitness advantages. Systems with two incompatible plasmids allow for burden minimization of high cost plasmids. They also enable buffering of an essential plasmid of interest by a non-essential, minimal sister plasmid. Lastly, coupled plasmid systems can maintain population memory following selection.

plasmid replication when CN exceeds some set point [141]. For instance, the widely used ColE1-origin of replication (ori) makes use of an antisense RNA that inhibits replication by selectively binding an RNA pre-primer that is essential for replication [142]. Since plasmids with the same ori share the same regulation strategy, they cannot be distinguished during replication, which can increase CN heterogeneity and facilitate loss of one plasmid. Plasmids that share replication mechanisms are referred to as incompatible because they cannot be stably maintained by a cell in the absence of external selection. Although it is widely accepted that plasmids with the same ori are unstable, some research suggests that plasmids from the same incompatibility group can persist for extended periods of time without selection [143] and some commonly used to measure plasmid loss rate may have overestimated plasmid loss rates [144].

In this work, we investigate the ability of two plasmid systems with shared oris to create

population heterogeneity and enable adaptation to different environmental conditions (Fig.4.1). We show that populations with heterogeneous gene expression created by plasmid ori redundancy rapidly adapt to stressors such as antibiotics and engineered cell lysis. We also show that in these shared ori systems a non-essential plasmid can act as a tuning knob for the CN of an essential plasmid, a concept we name *plasmid buffering*. In certain environments, we find that plasmid buffering leads to increased plasmid stability for incompatible plasmids compared to compatible ones, contradicting conventional wisdom that plasmid incompatibility always leads to faster plasmid loss. We also explore the dynamics of CN adaptation, specifically looking at how changes in CN persist following a transient selection. Overall, this work shows how plasmid incompatibility can create heterogeneity in a bacterial population, enabling copy number adaptation to different environments.

4.3 Results

4.3.1 Duplicate origin plasmid pairs generate population heterogeneity and enable environmental adaptation

Before engineering complex, two-plasmid systems with increased CN heterogeneity due to shared oris, we wanted to better understand the distribution of two distinct ColE1-type plasmids co-existing in a population of *E. coli*. To characterize heterogeneity in populations with duplicate ori constructs, we used two simple plasmids, one carrying a chloramphenicol resistance cassette (CmR) and expressing a red fluorescent protein (RFP) constitutively and one with a spectinomycin resistance cassette (SpecR) and expressing a green fluorescent protein (GFP) (Fig. 4.2A).

To test the fundamental assumption that duplicate ori plasmids would share a coupled total CN similar to that of a single plasmid with the same ori, we performed quantitative real time

PCR (qPCR) on strains containing either the two plasmids described above or a single plasmid carrying both antibiotic resistance and fluorescence markers (Fig. 4.2A). Relative qPCR CN of each fluorescent marker divided by the total ColE1 ori CN confirmed that in the duplicate ori case, the CN of each GFP or RFP plasmid was split roughly equally and each had about half of the total CN of a single ColE1 plasmid (Fig. 4.2B).

While qPCR provides a useful, population-level measurement of average CN, we wanted to better understand the underlying, single-cell CN distribution in two plasmid systems that either had the same oris or different oris with orthogonal regulation mechanisms. To do this, we compared two strains: one containing the GFP and RFP-expressing ColE1 plasmids described before (Dup_ori) and one with an RFP-expressing ColE1 plasmid and a GFP-expressing sc101 plasmid (Diff_Ori) (Fig. 4.2A). To obtain single cell fluorescence measurements of the Dup_Ori and Diff_Ori strains, we prepared agarose pad samples of each strain for fluorescence microscopy. In both the Dup_Ori and Diff_Ori strain, we saw considerable variability in both GFP and RFP expression. For the Diff_Ori strain, GFP and RFP expression were well correlated ($R^2 = 0.9357$) suggesting that variability in GFP and RFP expression was due to variability in the cell state that affected the CN of both plasmids similarly (Fig. 4.2D). Conversely, for the Dup_Ori strain, GFP and RFP expression showed little to no correlation ($R^2 = 0.464$), suggesting that the most significant cause of variability in this strain was the shared replication mechanism between the plasmids (Fig. 4.2C). Using a probabilistic plasmid replication and division model, we simulated growth of a population carrying two plasmids of either different or duplicate oris (Methods Fig. 4.7). In the absence of selection, we saw that this simple theory recapitulated the divergent heterogeneity we found experimentally with duplicate ori plasmids (Fig. 4.2E,F).

Having shown that plasmid CNs in the Dup_Ori strain were linked and heterogeneous, we wanted to see if the relative CN of the two plasmids could shift in response to different environmental conditions. To test whether variable antibiotic concentrations could bias the mean population CN, we cultured the Dup_Ori strain in 50x the normal working concentration of chlo-

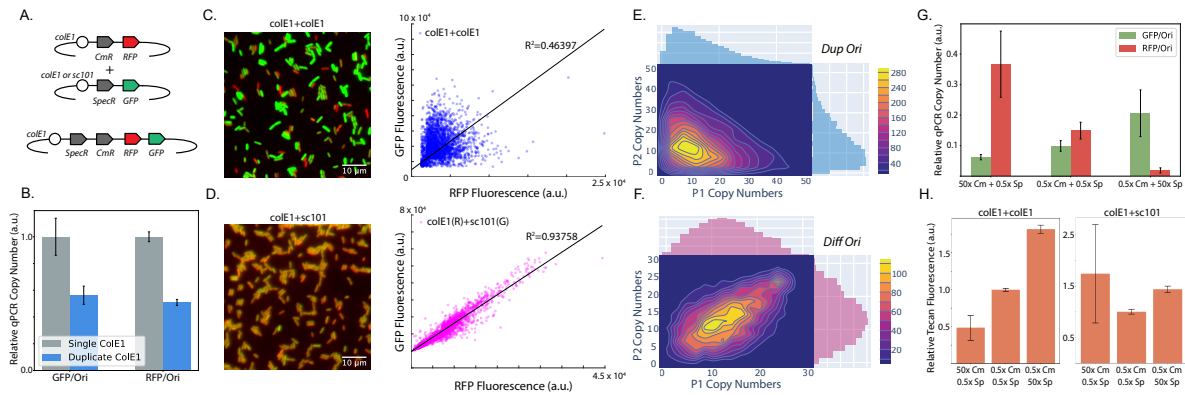


Figure 4.2: Two plasmid systems with redundant ori show increased heterogeneity and adaptability. (A) Diagram of plasmids used to look at CN behavior in different ori combinations. (B) Mean population CNs for a single ColE1 plasmid compared to two distinct ColE1 plasmids in the same cell as determined by qPCR. Error bars represent standard deviation of N=3 measurements. (C) Fluorescent micrograph of single cells with duplicate ColE1 ori plasmids and accompanying scatter plot showing GFP/RFP distribution for the population. (D) Fluorescent micrograph of single cells with different ori plasmids and accompanying scatter plot showing GFP/RFP distribution for the population. (E) Results from a model simulation showing CN distribution for incompatible plasmid pairs. (F) Results from a model simulation showing CN distribution for compatible plasmid pairs. (G) Bar chart showing relative plasmid CNs for the duplicate ori strain when grown in the presence of varying antibiotic concentrations. (H) Plate reader fluorescence for duplicate and different ori strains under different antibiotic concentrations.

ramphenicol or spectinomycin. As expected, the population shifted its plasmid CN distribution towards the favorable plasmid (the one with the relevant resistance gene), as determined by qPCR (Fig. 4.2G). Although absolute GFP and RFP fluorescence is likely affected by population health, the ratio of GFP to RFP is representative of the population's CN distribution between the two plasmids. Plate reader measurements of bulk GFP/RFP fluorescence agreed with the qPCR results showing the population shift towards the more beneficial plasmid in each growth condition (Fig. 4.2H).

When looking at the response of the Diff_Ori strain to growth on different antibiotic concentrations, we did not see a significant difference in relative GFP and RFP fluorescence levels measured with a plate reader, indicating that this strain likely did not undergo significant changes in relative CN in response to different selection conditions (Fig. 4.2H). In summary, we showed that plasmids carrying the same ori type have coupled CNs leading to increased population heterogeneity and the ability to undergo fitness-based environmental selection and adaptation.

4.3.2 Duplicate ori systems enable burden minimization and can increase plasmid stability due to buffering by non-essential plasmids

After showing fitness-based selection in response to antibiotic stress, we investigated whether duplicate ori strains could adapt to more biologically-relevant challenges, such as nutrient availability. It is well known that expression of metabolic pathway genes in *E. coli* is tightly regulated and dependent on metabolites in the surrounding environment. Furthermore, pathways for metabolizing nutrients can have complicated cost-benefit relationships, where cells must balance costly protein expression and enzyme activity with the benefit of increased nutrients for growth. For instance, Eames and Kortemme surprisingly found that for the lactose metabolizing operon of *E. coli*, lac permease activity is the most significant cost associated with operon expression and dictates cost/benefit trade-offs in lactose metabolism [145]. While native *E.*

E. coli carbon source operon CNs are essentially constant (at one copy), modification of CN is presumably one mechanism cells could use to balance metabolic costs and benefits. We wanted to see if CN flexibility enabled by duplicate ori plasmid pairs would allow a population of *E. coli* to tune enzyme expression levels for improved growth on different carbon sources.

To this end, we created an *E. coli* strain that had the full arabinose operon (araOp) on a RFP-expressing ColE1-type plasmid and the full lactose operon (lacOp) on a GFP-expressing plasmid with the same ColE1 ori (Dup_ori_met). We transformed these plasmids into an *E. coli* host (JS006) that has the native genomic versions of these operons knocked out [21].(Fig. 4.3A, Supplementary Fig. 4.8A). Naively, we expected the population to shift its CN distribution in favor of the essential carbon metabolizing plasmid while growing on that carbon source, for example increasing the CN of the araOp plasmid when grown on minimal media containing arabinose. However, when we grew this strain in batch culture in M9 media with different carbon sources we saw the opposite trend. Specifically, when grown on arabinose without antibiotic selection, we observed that GFP expression was significantly increased relative to growth on glucose or lactose and RFP expression was significantly decreased (Fig. 4.3B). When growing on arabinose, cells with fewer copies of the araOp likely had a fitness advantage over those with a higher plasmid operon CN. As a control, we created a strain that had the araOp on an sc101 ori plasmid and the lacOp on a ColE1 ori plasmid (Diff_ori_met), and thus should have no direct CN linkage. This effect was seen at a much smaller scale in the Diff_ori_met strain, but was just as pronounced in a duplicate ori strain with an MG1655 background that carries the genomic arabinose and lactose operons. Based on these results, we concluded that metabolic burden caused by induction of operon genes at high CN was the main driver of fitness-based adaptation in the batch culture, carbon metabolism experiments.

To further investigate CN adaptation to carbon source type, we continuously cultured the Dup_ori_met strain in a microfluidic device [146] that allowed us to vary the composition of growth media throughout the experiment (Fig. 4.3C). Cells were first cultured in M9 glucose,

followed by media switches to M9 lactose and then arabinose. No antibiotics were included in this experiment. When grown on lactose minimal media, the cell traps in the device consisted primarily of strongly-expressing RFP, weakly-expressing GFP cells indicating higher araOp CN relative to lacOp CN. Notably, many cell traps also had smaller sub-populations of cells with stronger GFP expression than RFP expression indicating higher lac operon CN. In response to a media switch to M9 arabinose, growth halted in all cell traps, but about 15% of 40 analyzed cell traps were able to resume growth. In the traps that resumed growth, the strongly-GFP expressing subpopulations rapidly took over the cell trap to become the dominant phenotype (Supplement Video 4.1). These results supported our interpretation of the batch culture results that population CN heterogeneity promoted adaptation to different nutrient conditions.

Each operon is naturally found in the genome at one copy and therefore is likely expressed optimally at low CN. We hypothesized that cells with higher CN of the essential plasmid had considerable burden when the operon was turned “on” as compared to cells with lower CN of the essential plasmid and a high CN of the non-essential and transcriptionally “off” plasmid. For example, when the Dup_ori_met strain is grown in arabinose, it requires at least one copy of the araOp plasmid to survive, but selects for cells with high lacOp plasmid CN. Since the lacOp plasmid genes are turned off when lactose is not present, this plasmid acts as a buffer to drive down the CN of the more burdensome araOp plasmid. We call this feature of coupled plasmid systems *plasmid buffering*, and we are the first group to our knowledge to describe it.

To confirm our hypothesis that maintaining low CN of an essential araOp plasmid optimizes growth rate in arabinose minimal media, we built a version of our ColE1 araOp plasmid with direct aTc-inducible CN (Supplementary Fig. 4.8B) based on a recent publication [138]. When transformed into *E. coli* MgG1655 Z1, induction of CN with aTc led to a dose-dependent decrease in growth rate, suggesting that cells with a higher CN experience higher burden (Fig. 4.3D). These results further suggest that the Dup_ori_met strain used plasmid buffering as a strategy to balance the cost and benefit of two carbon-metabolizing plasmids in different environments.

Systems with duplicate oris are always avoided in synthetic biology due to more rapid loss of one plasmid from the population. However, our previous results with plasmid buffering suggested that there are certain conditions where plasmids with the same ori may exhibit increased stability compared to plasmids with different oris. Specifically, we hypothesized that, when grown on arabinose-only media, the Dup_ori_met strain would retain the lacOp plasmid for longer than the Diff_ori_met strain. Remarkably, we saw that the fitness advantage conferred by plasmid buffering can stabilize non-essential plasmids in duplicate ori systems without the need for antibiotics. We found that when grown in M9 glucose, the Dup_ori_met strain lost the lacOp plasmid faster than the Diff_ori_met strain, but when the strains were grown on M9 arabinose, Dup_ori_met retained the lacOp plasmid for longer than the Diff_ori_met strain (Fig. 4.3E). Contradicting conventional wisdom regarding incompatible plasmids, in this situation, the non-essential buffer plasmid is protected from loss by indirectly reducing the burden of the essential plasmid. When we repeated this plasmid loss experiment on M9 lactose, we did not see increased stability in the Dup_ori_met strain compared to the Diff_ori_met strain (Supplementary Fig. 4.8D). We hypothesize that this is because the lacOp plasmid is not as burdensome as the araOp plasmid at high CN.

After demonstrating the general ability of our Dup_ori_met strain to buffer the burden of highly expressed metabolic operons, we tested the ability of duplicate ori systems to optimize their CN distribution in response to a gradient of resource availability. To do this, we cultured the strain in varied concentrations of lactose from 0.0125% to 0.1% (Fig. 4.3H). Our results indicate a decrease in the proportion of lacOp plasmid as lactose availability increased, suggesting reduced need for multiple copies of the lacOp plasmid. To separate the potential effects of metabolic need from lactose inducer burden, we also cultured the strain in the same lactose gradient but with 100uM IPTG, which ensures lacOp genes are maximally expressed. The gradient CN adaptation response to lactose availability remained present with IPTG and showed an overall reduction in GFP/RFP due to full expression of the operon. When we repeated this experiment with the

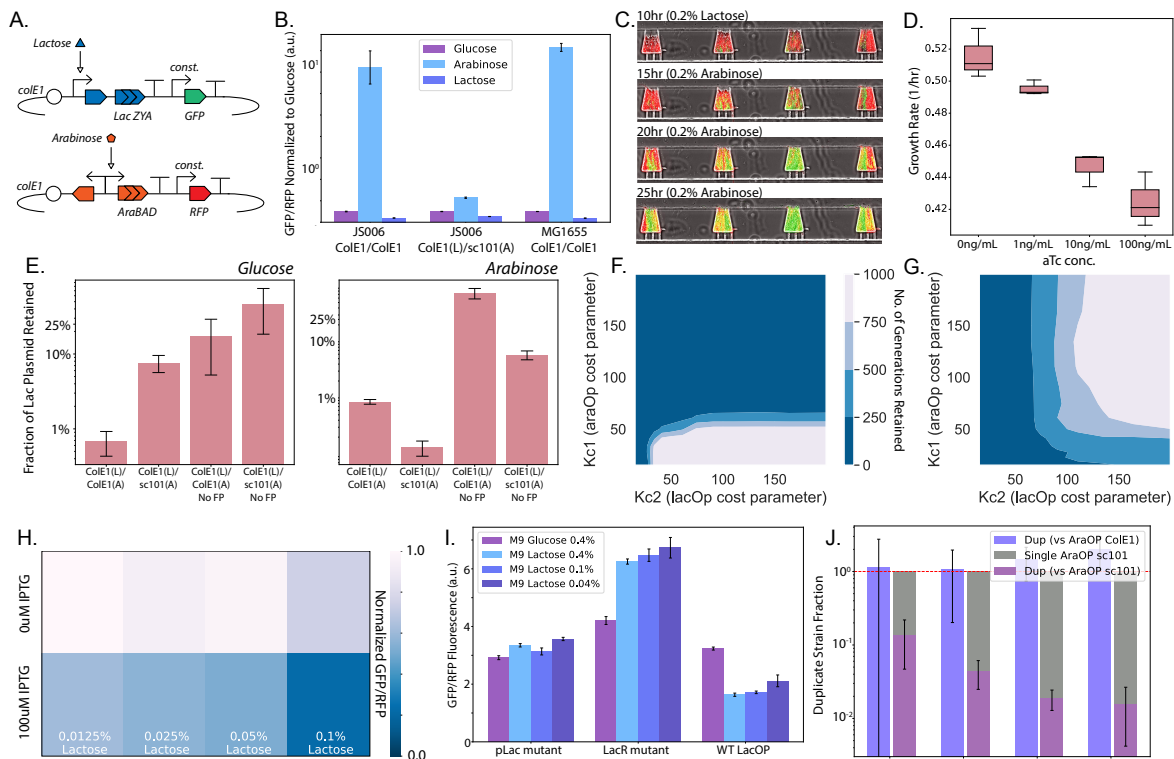


Figure 4.3: Duplicate origin plasmids allow burden-based adaptation to different nutrient environments and improve plasmid stability. (A) Circuit diagram for carbon source operon plasmids. GFP is expressed constitutively from the lactose operon-expressing plasmid and RFP is expressed constitutively from the arabinose operon-expressing plasmid. In the *Diff_ori_met* strain, the arabinose operon plasmid has the *sc101* ori. (B) Plate reader fluorescence data for *Dup_ori_met*, *Diff_ori_met*, and *Dup_ori_met_MG1655* strains for growth on different carbon sources in M9 minimal media. Error bars represent standard deviation of three separate cultures. (C) Representative fluorescence micrographs for the *Dup_ori_met* strain grown in a microfluidic device. Culture media carbon source was switched from lactose to arabinose at $t=10.5$ hours. (D) Growth rate averages for ipUC-Ara strain whose CN is directly induced with increasing aTC concentration. (E) Plasmid retention data for *Dup_ori_met* and *Diff_ori_met* strains grown on different carbon sources in M9 minimal media. Error bars represent standard deviation of three separate cultures. (F) Simulation of lactose plasmid retention when grown in arabinose for duplicate ori plasmids. Colormap corresponds to number of generations with plasmid still retained. (G) Same simulation for different ori plasmids. (H) Heatmap showing plate reader fluorescence data for the *Dup_ori_met* strain for different concentrations of lactose and IPTG in M9 media. Each square represents the mean value of three separate cultures. (I) Bar chart showing plate reader fluorescence data for different versions of the *Dup_ori_met* strain with mutated lac operons for different concentrations of lactose. Error bars represent standard deviation of three separate measurements (J) Proportion of *Dup_ori_met* strain in population when cultured over time in competition with single plasmid arabinose operon strain.

Diff_ori_met control strain, we did not see significant differences in GFP/RFP for different lactose concentration in the presence or absence of IPTG (Supplementary Fig. 4.8C).

In synthetic biology applications, plasmid constructs are usually not finely tuned to changing nutrient environments. Often it is hard to predict whether the expression level set by promoter choice is appropriate. In our WT version of the Dup_ori_met strain, lacOp expression was generally too costly. To investigate whether weakened versions of our metabolic constructs would optimize to a different CN point, we created two mutant versions of the lacOp plasmid, a pLac mutant known to decrease expression and a LacI mutant that also reduces operon expression [147]. These mutant lacOp ColE1 plasmids were co-transformed with a ColE1 ori araOp plasmid and the resulting strains were grown in various concentrations of lactose (Fig. 4.3H). Intuitively, both mutants with reduced operon expression had increased GFP/RFP, reflecting increased need for multiple copies of the weaker lacOp plasmid as compared to cells carrying the original plasmid. The LacI enhanced repression mutant also showed a gradient need for the lacOp that again increased with lowered lactose concentrations.

In summary, we have demonstrated the ability of duplicate ori strains to optimize the CN distribution between two carbon metabolizing constructs based on their expression strength and environmental growth condition. We also showed the benefits of plasmid buffering in reducing plasmid loss and improving strain fitness.

4.3.3 Minimal sister plasmid provides copy number flexibility and evidence of population memory

Following the discovery of plasmid buffering, we wanted to examine whether we could use it as a tool to characterize the cost-benefit balance of an arbitrary synthetic gene circuit as a function of environment. To realize this, we introduced the idea of a “sister plasmid” that shares the same ori as an essential plasmid, but only contains that ori and a selection marker to minimize its burden on the cell. We hypothesized that sister plasmids could impart CN flexibility and

thus promote sensitive adaptation to environment and also probe the environmentally determined cost-benefit function of an essential plasmid.

To test this idea, we co-transformed a ColE1 ori sister plasmid with a ColE1 plasmid carrying an AHL-inducible kanamycin resistance cassette (KanR) and constitutive GFP to make strain Dup_ori_kan (Fig. 4.4A). Using this setup, we directly varied the cost-benefit relationship of the plasmid in two directions by inducing different levels of KanR expression with AHL and also manipulating kanamycin concentrations in the culture media. In a plate reader experiment, we grew Dup_ori_kan in LB media containing 1x to 15x kanamycin working concentration and also 0nM to 100nM AHL. Convincingly, we saw that as kanamycin concentrations increased in the media, the KanR plasmid's CN went up as represented by increased GFP/OD. Conversely, as expression of KanR was increased via AHL, the CN went down to compensate for burden due to excess KanR expression (Fig. 4.4B). After passaging these cells into 1X kanamycin media, we incubated them in the reverse conditions of the initial selection. For example, cells previously incubated in 15x kanamycin and 0nM AHL were now cultured in 1x kanamycin and 100nM AHL. The resulting GFP/OD measurements matched expected CN adaptation, showing reversibility and secondary adaptation of Dup_ori_kan to a new environmental set point. When this same experiment was performed on a control strain with a minimal sc101 ori sister plasmid (strain Diff_ori_kan), we saw much smaller changes in GFP/OD in response to different selection conditions (Supplementary Fig. 4.9).

Based on these new results, we went back to improve our Dup_ori_met strain's growth on arabinose using a minimal sister plasmid. We replaced the lacOp plasmid in that strain with a minimal, ColE1 sister plasmid so that the strain could only grown on arabinose, but could still tune araOp copy number. To see if this new duplicate ori strain had a fitness advantage when compared to a single plasmid strain (containing only the araOp plasmid on either an sc101 or Cole1 backbone), we competed the two in co-culture on arabinose minimal media. By plating the culture on spectinomycin plates versus antibiotic-free plates, we quantified the proportion of the

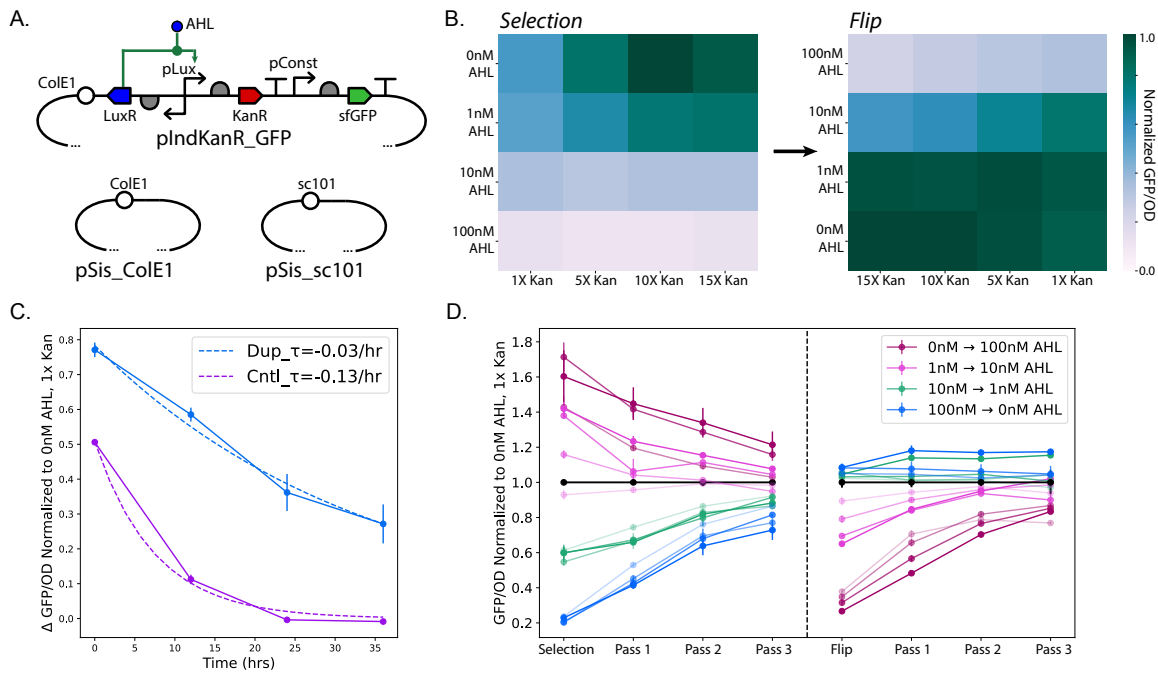


Figure 4.4: Incompatible “sister” plasmid buffering enables sensitive population adaptation and promotes long-term memory. (A) Circuit diagram of AHL-inducible KanR plasmid and accompanying minimal sister plasmids. (B) Heatmap showing plate reader fluorescence data for the Dup_ori.kan strain for different concentrations of AHL and kanamycin. Each square represents the mean of three separate cultures. Second heatmap shows fluorescence of cells following passage into “flipped” inducer conditions. (C) Representative plot of fluorescence decrease over time during passaging in non-selective media. Measurements of Dup_ori.kan and Diff_ori.kan strains are fit to exponential curve to estimate memory time constants. Error bars represent standard deviation of three separate cultures. (D) Plate reader fluorescence measurements for Dup_ori.kan in all inducer conditions over time, including non-selective passaging and subsequent flipped induction. Line opacity represents environmental kanamycin concentration with highest opacity corresponding to 15x Kan.

population that was the new Dup_ori_ara_sis strain over time. Over the course of 4 days, we saw that this Dup_ori_ara_sis strain out-competed a single ColE1 araOp plasmid strain while it had a moderate fitness disadvantage compared to a single sc101 araOp plasmid strain with lower CN than ColE1 (Fig. 4.3I).

We then hypothesized that the use of sister plasmid buffering not only enabled reversible adaptation of plasmid CN to environmental need, but could also generate population memory of CN state. In the inducible KanR experiment described previously, GFP/OD was also measured over three non-selective passaging time points after each selection phase. Rather than immediately losing CN shifts once selection is removed, the population retained memory of the selection event and returned to baseline gradually over many generations (Fig. 4.4D). The time scale of population memory for Dup_ori_kan (0.03/hr) was considerably longer than in a distinct ori control strain (0.13/hr) where some CN adjustment was seen but was then rapidly lost upon removal of selection (Fig. 4.4C).

In summary, the use of a minimal sister plasmid with a duplicate origin enables the cost-benefit characterization of synthetic constructs in different environments. In addition, plasmid coupling creates population memory of CN state without the need for additional circuit components.

4.3.4 Redundant ori plasmid systems promote generational population memory in response to engineered cell lysis in microfluidic culture.

To further investigate the temporal dynamics of population memory in continuous culture, we used a duplicate ori strain carrying two inducible lysis constructs on ColE1 plasmids (Dup_ori_lyt). Each plasmid rapidly triggers cell death via the E lysis gene from phage ϕ X174 in response to a small molecule inducer. This model system creates easily tunable bidirectional selection as well as short time scales for adaptation due to the all-or-none nature of lysis-based selection. Together these attributes make plasmid lysis circuits optimal to investigate CN dy-

namics and memory in continuous culture. The first plasmid codes for AHL-inducible lysis and constitutive GFP, while the second encodes arabinose-inducible lysis and constitutive RFP (Fig. 4.5A). After confirming successful CN adaptation of Dup_ori_lys against lysis pressure in plate reader experiments (Supplementary Fig. 4A), we then cultured the strain in a previously described microfluidic chip along a gradient of arabinose and AHL concentrations (Fig.4.5B and Supplementary Fig. 4.10C). In this device, small bacterial populations grow as monolayers in cell traps of different sizes [148]. The device has two inlet media sources connected to a set of branching fluidic channels that create a concentration gradient across the different cell traps of the device, allowing us to vary arabinose and AHL concentrations on a single microfluidic chip. When cultured in this system, the Dup_ori_lys strain adapted similarly to batch culture, with high GFP-expressing, pAHL_Lyse plasmid dominant populations taking over cell traps for high arabinose concentrations and high RFP-expressing, pAra_Lyse plasmid dominant populations taking over cell traps for high AHL concentrations. Resulting GFP and RFP fluorescence over a 24 hour run are summarized in Fig. 4.5B for inducer concentrations up to 100nM AHL or 0.017% Arabinose. When we repeated this experiment with a control strain (Diff_ori_lys) that had the pAra_lyse plasmid on an sc101 ori, we saw virtually no CN shifting to different arabinose and AHL conditions, further suggesting that ori redundancy enabled adaptation (Supplementary Fig. 4.10C and 4.11A)

We hypothesized that due to rapid selection in this system, CN adaptation would sensitively respond to the lysis expression strength of each plasmid. In particular, we had found that the original Dup_ori_lys strain had significant leaky expression of the lysis gene, most likely due to expression from the arabinose promoter even when uninduced (Supplementary Fig. 4.10B). To investigate the sensitivity of CN adaptation to lysis strength we developed a library of pAra_Lyse plasmids, each with different lysis gene expression strengths. This library was generated through site directed mutagenesis (SDM) of the ribosome binding site (RBS) before the E lysis gene on the original pAra_Lyse plasmid. Each library plasmid's lysis strength was assessed in response to

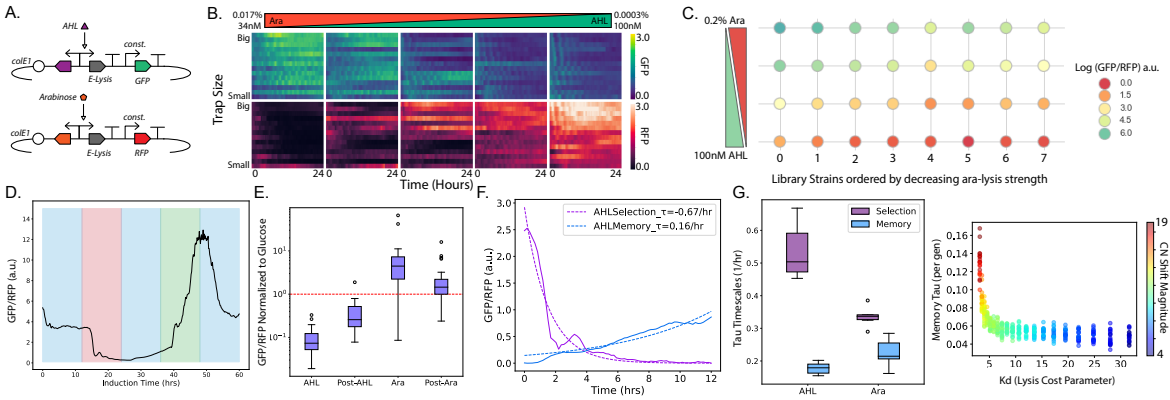


Figure 4.5: Inducible cell lysis triggers population CN shifting in duplicate ori systems. (A) Circuit diagram for inducible lysis plasmids. GFP is expressed constitutively from the AHL inducible lysis plasmid and RFP is expressed constitutively from the arabinose inducible lysis plasmid. In the *Diff_ori_lysis* strain, the arabinose inducible lysis plasmid has the *sc101* ori. (B) Heatmap showing mean fluorescence over time for the *Dup_ori_lysis* strain in a microfluidic device with different inducer concentrations and trap sizes. (C) Plate reader fluorescence of *Dup_ori_lysis* strain library with variant arabinose lysis strength across four inducer conditions. (D) Mean fluorescence over time for *Dup_ori_lysis* strain in a microfluidic device with five induction windows: 0.2% Glucose (non-selective), 100nM AHL (selective), Glucose, 0.02% Arabinose (selective), and Glucose. (E) Mean fluorescence of *Dup_ori_lysis* strain at the end of each induction window in previous panel. Mean and standard deviation of 24 individual traps are represented. (F) Representative mean fluorescence plot over time of one row of four traps during AHL selection and memory phases. Curves are fit to exponential function to estimate memory time constants. (G) Mean memory time constants for all 24 traps during each phase of microfluidic experiment. (H) Simulated relationship between memory time scale, CN shift magnitude, and lysis strength after 100 generations of selective growth and during 100 non-selective generations.

induction with 0.02% arabinose as described in the methods (Supplementary Fig. 4.12A). These library plasmids were then co-transformed with the original *pAHL_Lyse* plasmid and grown in various inducer concentrations in batch culture. A clear relationship between lysis expression strength and final GFP/RFP ratio was found in the 8 strains tested, with increasing arabinose lysis strength corresponding to a increase in GFP/RFP and therefore *pAHL_Lyse* CN across all inducer conditions (Fig. 4.5C and Supplementary Fig. 4.12B).

After confirming the rapid and fine-tuned adaptation of *Dup_ori_lysis* above, we characterized the strain's memory dynamics using time-lapse microscopy. Specifically, we grew our strain along with *Diff_ori_lysis* within a multi-strain microfluidic chip [146]. In 12 hour windows

we cultured the populations first in LB media supplemented with glucose followed by LB with 100nM AHL, LB with glucose, LB with 0.02% arabinose, and LB with glucose again (Fig. 4.5D and Supplementary Fig. 4D and 4E). Antibiotics were used throughout the experiment to ensure at least one copy of each plasmid was always maintained. The Dup_ori_lys strain responded to both selection windows showing reversible adaptation. Again, we saw that following non-selective growth for 12 hrs even in high turnover continuous culture, populations still retained CN memory of the prior selection event, as measured by GFP/RFP levels (Fig. 4.5E). Following the first AHL induction, population memory was especially striking with the relative time scale of return to baseline being over four times slower than that of the selection phase (Fig. 4.5F). While the difference between selection and memory time scales for the arabinose induction phase was less substantial, this is likely due to the population being biased toward higher CN of the RFP before switching to arabinose and therefore undergoing slowed selection towards the pAHL_Lyse GFP plasmid (Fig. 4.5G). The magnitude of GFP/RFP following arabinose selection still suggests memory is retained when compared to the initial glucose condition.

In summary, duplicate ori plasmids enable fast adaptation to engineered lysis burden in continuous culture experiments. The CN balance of these strains responds sensitively to the relative lysis gene expression strength of the plasmids and environmental conditions. By visualizing these populations over many generations in microfluidics, we could clearly demonstrate population CN memory following a selection event while still maintaining the ability to reversibly adapt. Overall this suggests the fundamental capability of plasmid coupling in producing population state memory over generational time scales without the need for added circuitry.

4.3.5 Engineered plasmid incompatibility enables coupled copy number tuning in two plasmid systems

While the previous experiments show that the population-average plasmid copy number in duplicate ori systems can readily change in response to different environmental pressures,

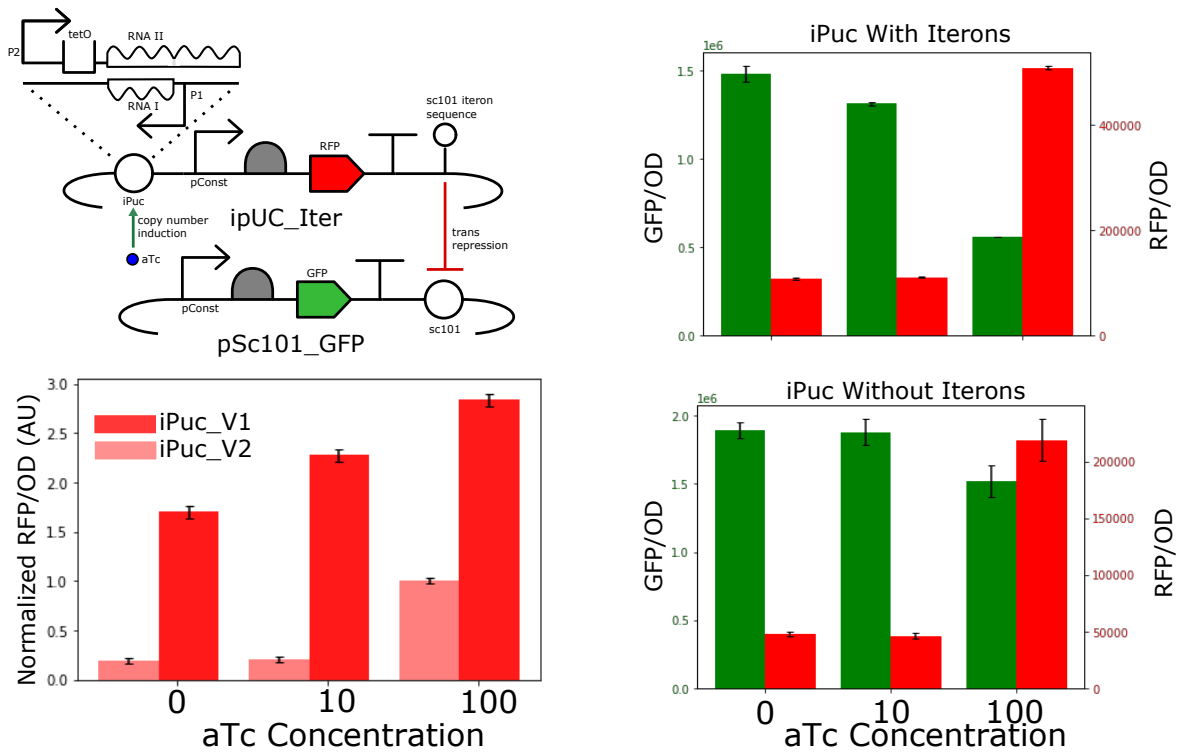


Figure 4.6: Engineered plasmid incompatibility enables coupled copy number tuning in two plasmid systems. (A) Circuit diagram of inducible copy number pUC plasmid (iPuc) coupled to an sc101 plasmid by using an iteron sequence. (B) Plate reader fluorescence data showing induction of iPuc plasmid copy number for different concentrations of aTc. Error bars represent standard deviation of three separate cultures. (C) Plate reader fluorescence data for a strain with iPuc plasmid with or without the iteron sequence co-transformed with an sc101 plasmid. Error bars represent standard deviation of three separate cultures.

we sought to show that the copy numbers of two plasmids from different compatibility groups could be linked by engineering tunable incompatibility between them (Fig. 4.6A). Specifically, we started with a pUC-ori plasmid with an aTc-inducible copy number (ipUC). To this plasmid, we added one copy of an iteron sequence from the pSC101 origin (ipUC-IT). Previous research has shown that high-copy, non-sc101 plasmids containing this iteron sequence have significant incompatibility toward WT pSC101 plasmids [149]. Thus, we hypothesized that when the ipUC-IT plasmid was co-transformed into *E. coli* with a pSC101-type plasmid, that the relative copy number of the two plasmids could be tuned by aTc. Specifically, since aTc increases the copy number of the ipUC-IT plasmid (and thus the number of iteron DNA sequences) it should decrease the copy number of the pSC101-type plasmid. In order to test this system, we co-transformed the ipUC-IT plasmid with a WT pSc101 plasmid into the *E. coli* strain MG1655 Z1, which constitutively expresses the tetracycline repressor protein, TetR. In response to aTc, we saw increased RFP expression indicating increased iPuc-IT plasmid copy number and decreased GFP expression indicating decreased pSc101 copy number (Fig. 4.6C). As a control, we looked at the effect of iPuc copy number induction on pSc101 copy number when the sc101 iteron sequence was removed for the iPuc plasmid. We found that full induction of the iPuc plasmid without iterons only slightly decreased GFP expression indicating a small decrease in sc101 copy number. This result confirmed that the placement of the iteron sequence on the iPuc plasmid was necessary for strong copy number linkage between these plasmids.

Discussion

Synthetic biology as a field strives for tight control of cellular phenotypes. Gene circuits are finely tuned for deployment, and any variability is seen as a negative feature. In the natural world, however, populations will often exploit noise and heterogeneity in the face of unpredictable environments to improve survival. In this work we took inspiration from natural systems to

create heterogeneous populations capable of environmental adaptation, burden minimization, and population memory. We used coupling between two plasmids of the same origin type to allow reversible copy number flexibility within a microbial population.

Previous work has shown that the expression level of metabolic proteins evolves towards an optimal level when cultured in a specific nutrient environment over time [150]. Here, we show optimization of protein expression strength based on environment by strains carrying duplicate origin plasmids that enable copy number adjustment rather than mutation to improve fitness. We introduced the concept of plasmid buffering where one essential plasmid driving population fitness is given a tunable copy number through the presence of a secondary non-essential plasmid with the same origin. Plasmid buffering in such systems allows for copy number adjustment in response to different growth environments. A recent study by Yang et al. created a synthetic circuit for eliminating gene dosage variation in individual mammalian cells [151]. Their method buffers plasmid CN variability in mammalian cells to reduce heterogeneity while we use plasmid CN flexibility to buffer circuit burden. Comparing these studies points out how copy number flexibility can be desirable sometimes, but copy number heterogeneity can be reduced if needed.

Recent work by the Ellis lab and others on both burden reporting and burden-responsive feedback control of synthetic circuits, highlights the importance of considering the effects of synthetic circuit burden on cellular fitness [31, 32]. Our study shows how plasmids with overlapping replication mechanisms can allow a cell to minimize burden caused by protein expression that is mismatched with the culture environment. In addition, we show that not only can plasmid buffering minimize burden, but it can also increase the stability of a non-essential plasmid by giving it an indirect benefit to the cell. Research on improving genetic stability of constructs has shown the effectiveness of reducing host mutational ability, overlapping sequences of essential and non-essential genes, and recoding translation among many other strategies [33]. Here we are able to enhance genetic stability specifically in duplicate origin systems. despite conventional wisdom regarding incompatible plasmids.

Plasmid incompatibility has been studied since the early 1970's and there are multiple, published models to understand the dynamics of plasmid loss between plasmids with shared replication mechanisms [152–154]. Specifically, the effects of different methods for choosing which plasmid to replicate and how to partition these plasmids to daughter cells has been investigated mathematically [155]. However, there is a lack of mathematical models that consider the cost and benefit associated with plasmid encoded functions and how these costs and benefits can change with environment. Here we show that a basic probabilistic model that uses Hill-like functions to simulate plasmid cost and benefit can recapitulate many features of incompatible plasmids seen experimentally. In the future the model could be improved by trying to get more precise parameters for plasmid replication rates, cell growth rates, and cost/benefit function parameters. We could also include a more complex framework for host-circuit burden coupling, like some recently proposed approaches [156].

While we are the first group to our knowledge to document adaptation due to duplicate ori plasmid pairs, a recent study by Tomanek et al. investigated a similar phenomenon of gene copy number adaptation [134]. Specifically, they describe a mechanism called amplification-mediated gene expression tuning (AMGET). While we showed that plasmid CN heterogeneity enables adaptation to variable environments, they “show that gene duplications and amplifications enable adaptation to fluctuating environments by rapidly generating copy-number and, therefore, expression-level polymorphisms.” The core idea of stochastic, copy number heterogeneity promoting population adaptation is shared between their study and ours. However, they describe different mechanisms for generating copy number variation. While we exploit the cell's inability to distinguish plasmids with the same origin, Tomanek et al. studied how gene duplication and amplification arising from homologous recombination between sister chromosomes leads to CN variation. This mechanism of generating copy number occurs naturally in cells without synthetic gene circuits, which begs the question: are plasmid systems with redundant replication mechanisms also utilized in nature to cope with varying environments?

Lastly, we demonstrate memory in cell populations containing duplicate origin plasmids following environmental selection. Researchers have created population-state memory in synthetic systems through the use of bistable genetic circuits, and more recently the development of a methylation-based epigenetic system within *E. coli* [157]. Here, we develop generational memory through plasmid inheritance of population copy number distribution. Studies on history-dependence of microbial populations have cited chromatin state, protein inheritance, metabolic history, and strong heterogeneity as potential mechanisms for memory of past environmental exposures [158]. In this work, we took inspiration from these natural mechanisms of population adaptation to demonstrate the broad use of duplicate origin plasmids as a tool to improve performance of synthetic microbial populations.

4.4 Supplemental Figures

Table 4.1: Bacterial strains used in chapter 4

Strain Name	Plasmids	Host Designation	Relevant Figure
Dup_ori	pSKAL001, pSKAL003	MG1655	2
Diff_ori	pSKAL002, pSKAL003	MG1655	2
Diff_ori_met	pSKAL006, pSKAL007	JS006	3
Dup_ori_met	pSKAL005, pSKAL006	JS006	3
Dup_ori_lys	pSKAL017, pSKAL019	MG1655	5
Diff_ori_lys	pSKAL017, pSKAL018	MG1655	5
Dup_ori_kan	pSKAL014, pSKAL015	MG1655	4
Diff_ori_kan	pSKAL014, pSKAL016	MG1655	4

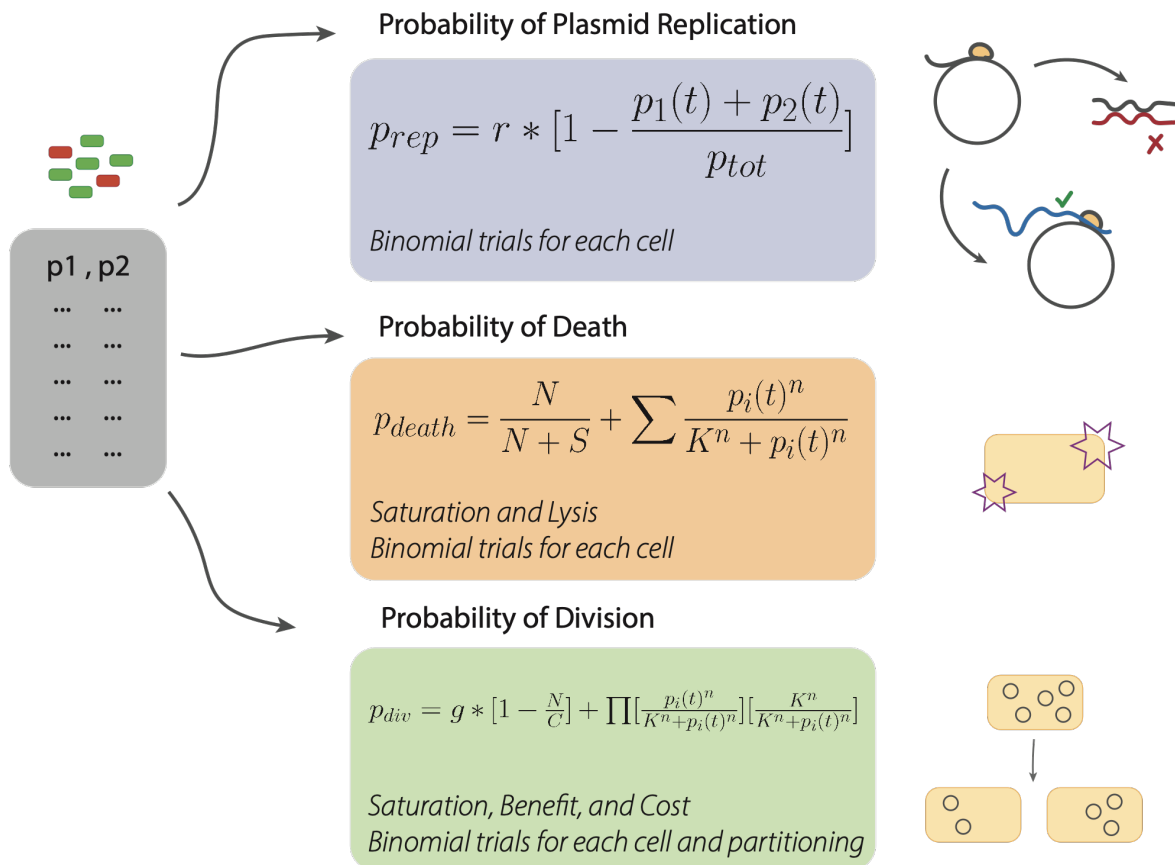


Figure 4.7: To study how the plasmid copy number distribution of a population changes over time, we created a stochastic model that considers the cost/benefit associated with a given plasmid. The model consists of cells containing two distinct plasmids that can have either the same or orthogonal mechanisms of replication and copy number maintenance. In each generation the following steps are carried out: 1) plasmids are replicated, 2) some members of the population die (due to plasmid encoded or effects of population saturation), 3) cells have the chance to divide based on plasmid-associated cost-benefit functions, and 4) for dividing cells, plasmids are partitioned to two daughter cells. See methods section for details on parameters. Modeling results are plotted in Figure panels 2E, 2F, 3F, 3G, and 5H.

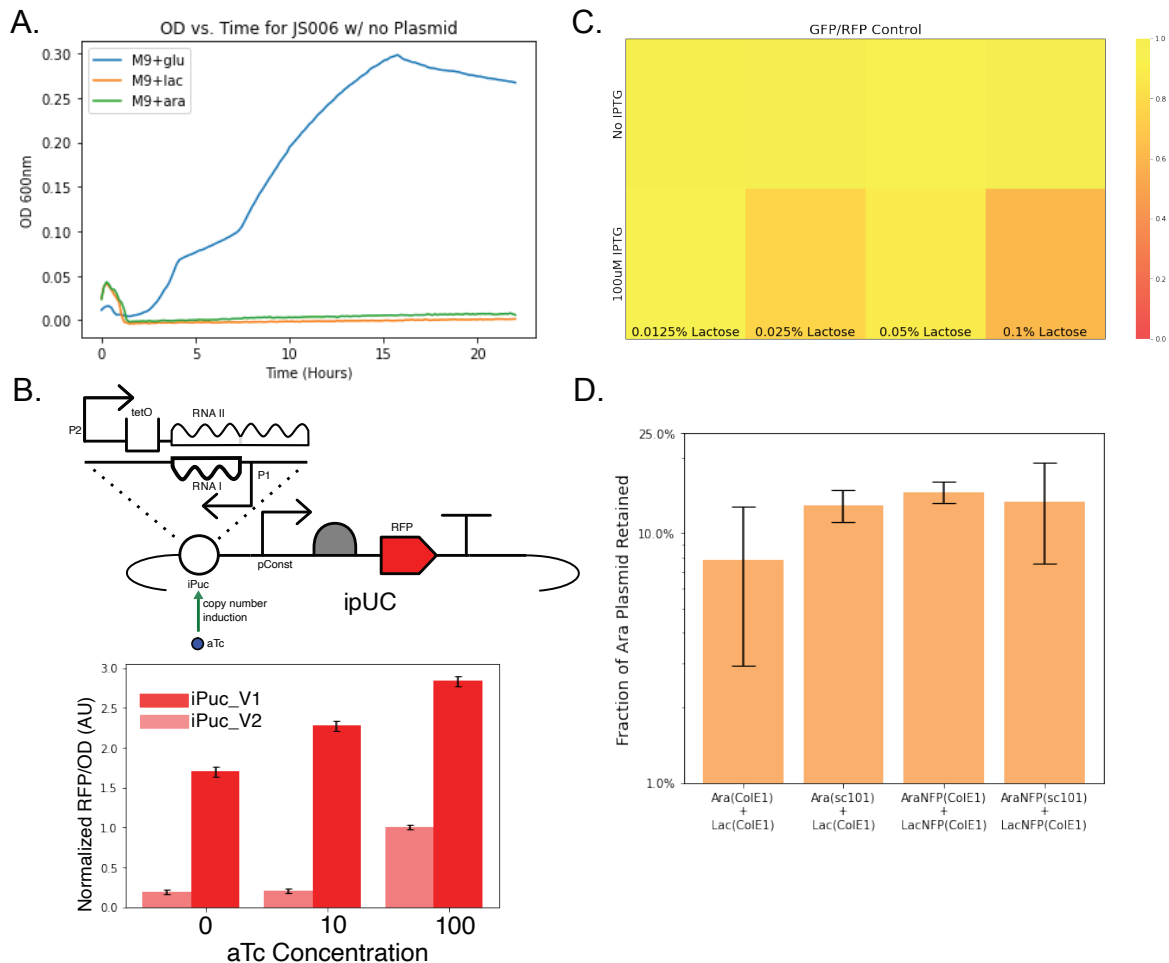


Figure 4.8: Supplementary material related to Figure 4.3. (A) Strain JS006 is unable to grow on minimal media with arabinose or lactose as the only carbon source unless operon genes are supplied on plasmids. (B) Proof of function for inducible copy number plasmid, Top: Circuit diagram for testing aTc-inducible pUC copy number. Bottom: Bar chart showing RFP fluorescence vs. aTc concentration for two different versions of the inducible pUC system with different tetO operator sequences. Error bars represent standard deviation of N=5 measurements. (C) Heatmap of GFP/RFP fluorescence values for the Diff_ori_met strain grown on different concentrations of lactose and IPTG. Comparison data for main Figure 4.3H. (D) Plasmid retention data for Dup_ori_met and Diff_ori_met strains grown on lactose minimal media. Comparison data for main Figure 4.3E.

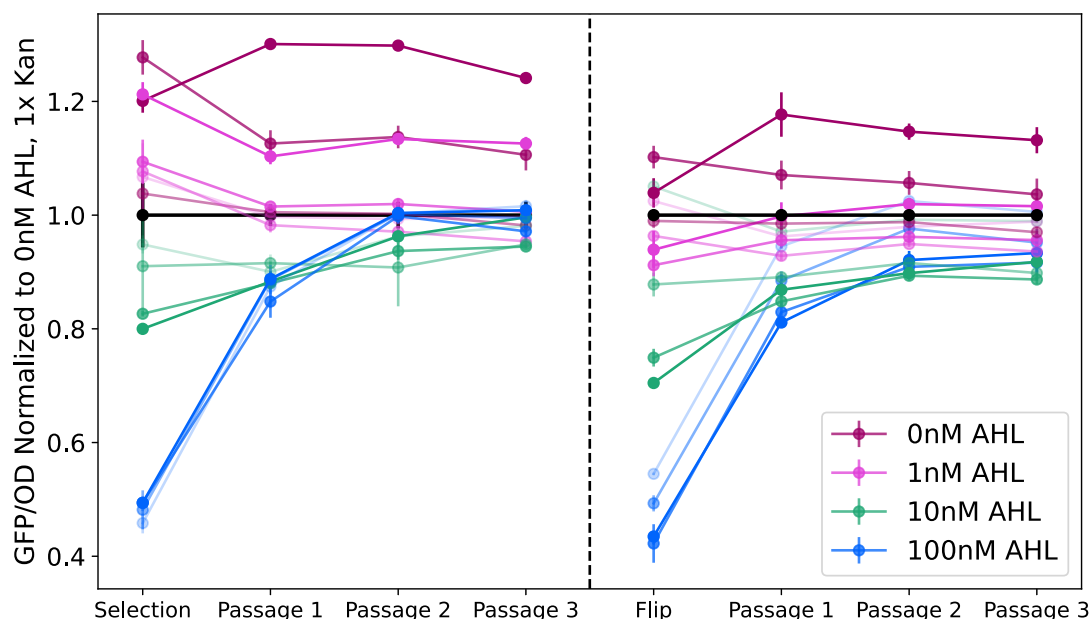


Figure 4.9: Supplementary material related to Figure 4.4. Plate reader fluorescence measurements for Diff_ori_kan in all inducer conditions over time during non-selective passaging with subsequent flipped induction. Comparison data for Figure 4.4D.

Table 4.2: Plasmids used in chapter 4

Plasmid ID	Resistance	Origin	Fluorescent Protein	Circuit	Relevant Figure(s)
pSKAL001	SpecR	ColE1	GFP	N/A	2
pSKAL002	SpecR	sc101	GFP	N/A	2
pSKAL003	CmR	ColE1	RFP	N/A	2
pSKAL004	CmR, SpecR	ColE1	GFP, RFP	N/A	2
pSKAL005	CmR	ColE1	RFP	araBAD operon	3
pSKAL006	SpecR	ColE1	GFP	Lac operon	3
pSKAL007	CmR	sc101	RFP	araBAD operon	3
pSKAL008	CmR	iPuc	RFP	araBAD operon	3
pSKAL009	CmR	ColE1	N/A	araBAD operon	3
pSKAL010	CmR	sc101	N/A	araBAD operon	3
pSKAL011	SpecR	ColE1	N/A	Lac operon	3
pSKAL012	SpecR	ColE1	GFP	Lac operon pLac mutant	3
pSKAL013	SpecR	ColE1	GFP	Lac operon LacI mutant	3
pSKAL014	SpecR, (KanR)	ColE1	GFP	AHL inducible KanR	4
pSKAL015	CmR	ColE1	N/A	N/A	4
pSKAL016	CmR	sc101	N/A	N/A	4
pSKAL017	SpecR	ColE1	GFP	AHL inducible lysis	5
pSKAL018	CmR	sc101	RFP	Arabinose inducible lysis	5
pSKAL019	CmR	ColE1	RFP	Arabinose inducible lysis	5
pSKAL020	CmR	iPuc	RFP	N/A	Supplement

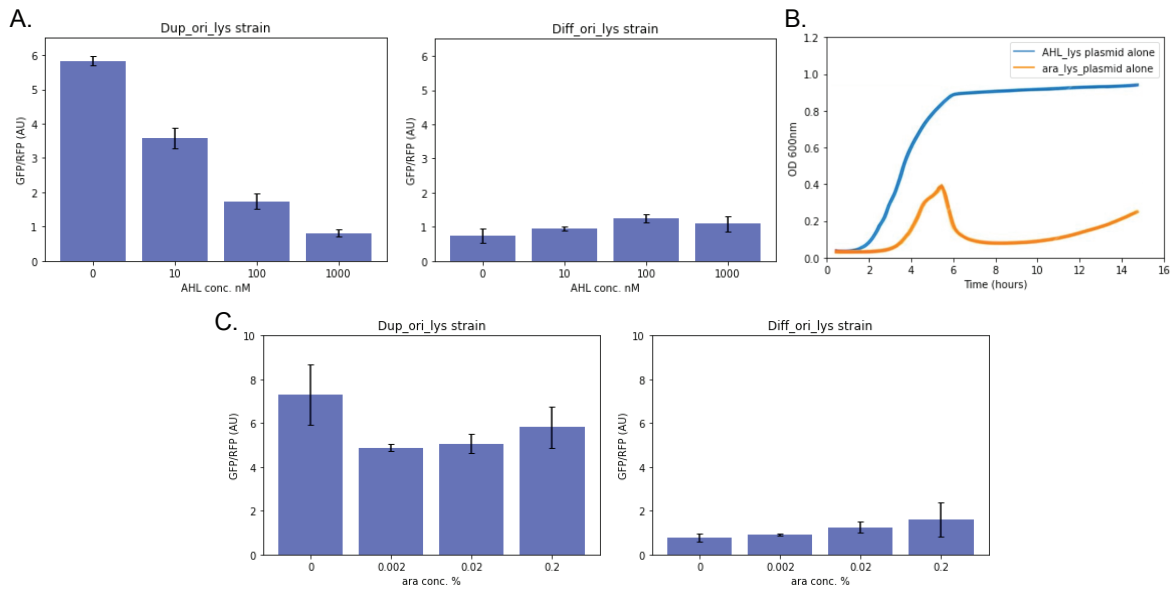


Figure 4.10: Supplementary material related to Figure 4.5. (A) Relative GFP/RFP fluorescence for the Dup_ori_lys and Diff_ori_lys strains grown in batch culture in different concentration of AHL. (B) Growth curves for strains containing either the pAHL_Lyse plasmid or the pAra_Lyse plasmid only. Even without inducer, the original pAra_Lyse plasmid causes cell death in LB as seen in the growth curve. (C) Relative GFP/RFP fluorescence for the Dup_ori_lys and Diff_ori_lys strains grown in batch culture in different concentration of arabinose.

Table 4.3: Primer sequences for qPCR

Primer Name	Sequence
GFP_fwd	GGGTGAAGGTGATGCTACAA
GFP_rev	GAACACCATAGGTCAGAGTAGTG
RFP_fwd	CACCCAGACCATGAGAATCAA
RFP_rev	TGGGTGTGGTTGATGAAGG
ColE1_fwd	CACGCTGTAGGTATCTCAGTTC
ColE1_rev	GGTTGGACTCAAGACGATAGTT
Chrom_fwd	GCGAGCGATCCAGAAGATCT
Chrom_rev	GGGTAAAGGATGCCACAGACA

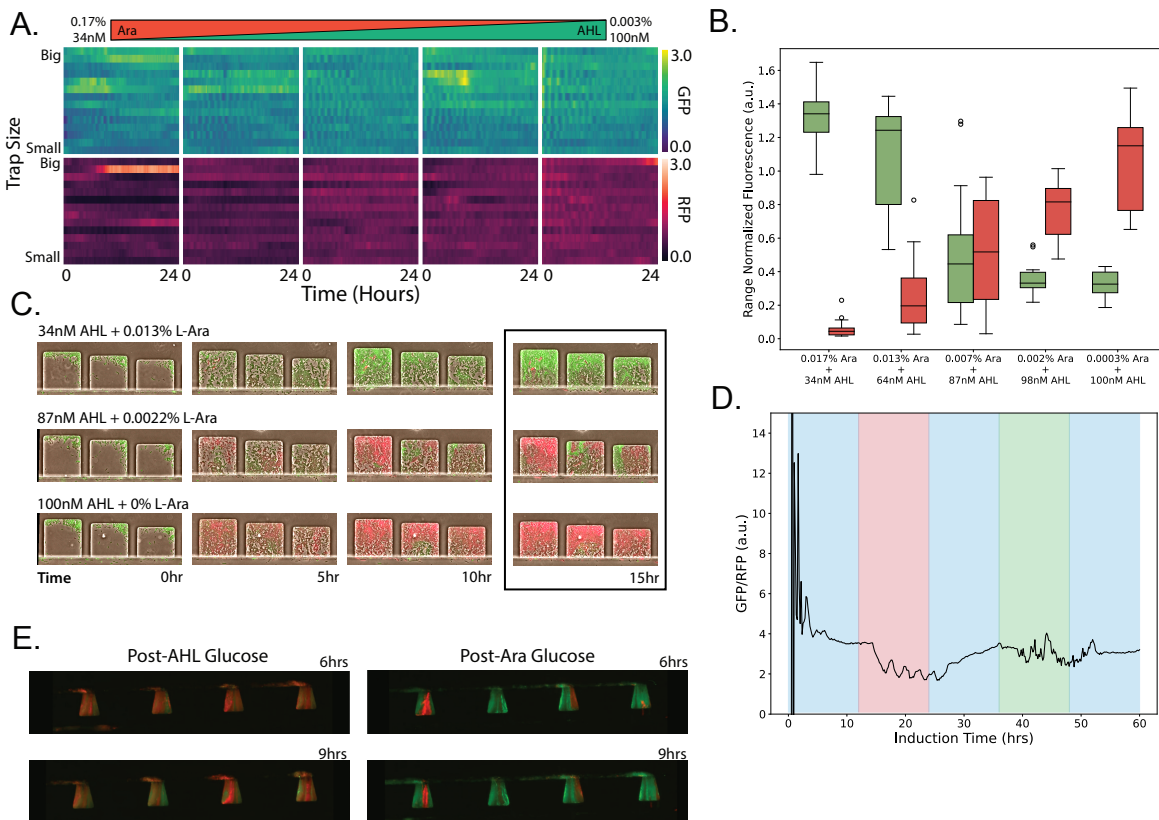


Figure 4.11: Supplementary material related to Figure 4.5. (A) Heatmap showing GFP and RFP fluorescence levels over time for the Diff_ori_lys strain grown in various concentration of AHL and arabinose in a microfluidic device. Comparison data for Figure 4.5B. (B) Boxplot showing final mean cell trap GFP/RFP fluorescence ratios for the Dup_ori_lys strain gradient microfluidic experiment. Associated with Figure 5B. (C) Representative microscope images from gradient microfluidic experiment with Dup_ori_lys strain. Images correspond to data shown in Figure 4.5B. (D) Mean fluorescence over time for Diff_ori_lys strain in a microfluidic device with five induction windows: 0.2% Glucose (non-selective), 100nM AHL (selective), Glucose, 0.02% Arabinose (selective), and Glucose. Comparison data for Figure 4.5D. (E) Representative fluorescence micrographs of the Dup_ori_lys strain grown in a microfluidic device over time in fluctuating environmental conditions. Microscope images correspond to data shown in Figure 4.5D-F.

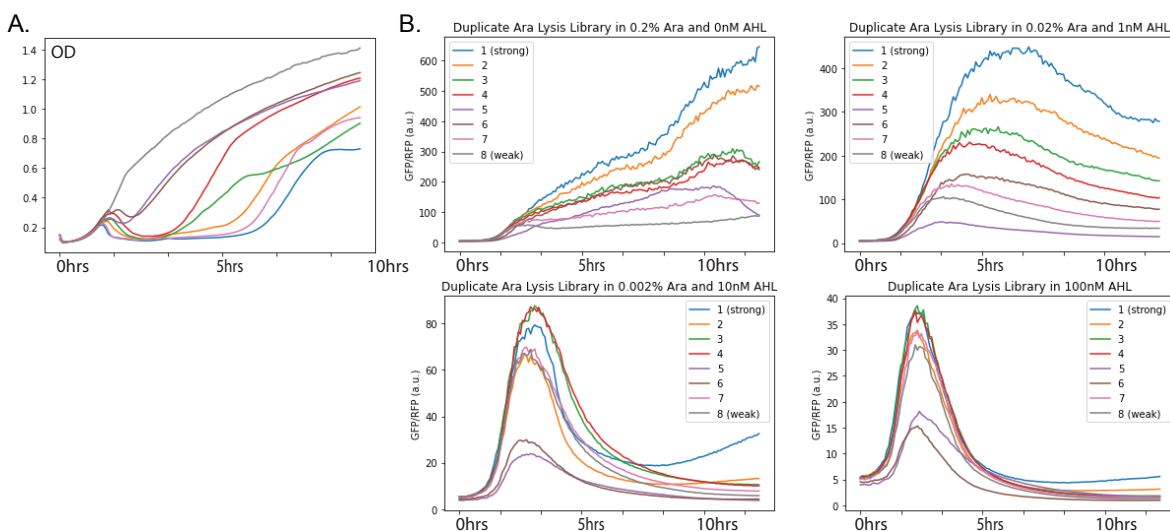


Figure 4.12: Supplementary material related to Figure 4.5. (A) Growth curves for 8 different strains grown in LB with 0.02% arabinose with various versions of the pAra_lyse plasmid. Each strain has a different RBS preceding the lysis gene, E. Data related to Figure 4.5C (B) Plate reader fluorescence data over time for the 8 different Dup_ori_lys library strains grown in different AHL and arabinose concentrations. Data related to Figure 4.5C.

4.5 Materials and Methods

4.5.1 Strains and plasmids

E. coli MG1655 (NCBI U00096.3) was used as the host strain for the majority of experiments except where noted. For experiments involving the lactose and arabinose operon strains, *E. coli* strain JS006 [?, 21] was used. This strain is derived from the *E. coli* Keio knockout collection parent strain, BW25113, and has the following relevant mutations: $\Delta(\text{araD-araB})567, \Delta\text{lacZ}4787(::\text{rrnB-3}), \Delta\text{lacI}, \Delta\text{araC}$. For experiments involving the inducible pUC copy number plasmids, the *E. coli* K-12 MG1655Z1 strain was used, which constitutively expresses lacI and tetR from the genome.

All plasmids were constructed by Gibson assembly using PCR amplified fragments of previously constructed plasmids from our group. The full *E. coli* lactose operon was amplified from the MG1655 strain genome. The full *E. coli* arabinose operon was also amplified from

the MG1665 strain genome. The inducible lysis library was created using a mutagenic primer targeting the ribosome binding site in front of its lysis gene.

4.5.2 Plate reader experiments for estimating average copy number in batch culture using fluorescence

For plate reader experiments assessing strain growth and bulk fluorescence, saturated overnight cultures of a given strain were diluted 1:100 into 200uL of fresh media and cultured in 96-well flat bottom plates at 37C with orbital shaking in a Tecan Infinite M200 Pro. Optical density (OD) and fluorescence measurements were taken every 5 minutes and the cultures were grown to saturation. GFP and RFP measurements were normalized by dividing by the culture OD at each time point. For use in comparative plots between conditions, final GFP/OD and RFP/OD were determined from when the OD maximized, or stopped increasing, a signal of early stationary phase.

4.5.3 Agarose pad slide preparation for single-cell imaging and analysis

To image live *E. coli* cells following growth in relevant media conditions, overnight cultures were diluted 10 fold in sterile water before 2uL were pipetted onto a glass coverslip. Cells were then sandwiched by placing an agar pad (1.5% agarose) on top to create a flat focal plane. Agar pads were made the depth of one coverslip using the method described in [159]. To analyze single cell fluorescence from images, a custom Matlab script was written that segmented single cells prior to recording their average fluorescent intensity. The segmentation workflow included image filtering, edge detection followed by object filling, and lastly individual cell classification and assignment using size and fluorescence thresholds.

4.5.4 Quantitative PCR for determination of average copy number

For direct quantification of plasmid copy number, saturated cell cultures were analyzed by qPCR. Following growth in relevant media conditions, cells were incubated at 95C for 10 min prior to freezing at -20C. Lysed cultures were then diluted 100 fold for use as final templates. Each qPCR reaction consisted of 10uL of SYBR green master mix, 4uL water, 5uL diluted template, and 0.5uL of each primer. Primers were designed to amplify approx. 100bp regions within the GFP gene, RFP gene, plasmid origin, and the *E. coli* chromosome. Reactions were run in triplicate using MicroAmp Fast Optical 96-well plates within the Applied Biosystems Quant 3 machine for comparative CT measurements. Resulting measurements were normalized to chromosomal control reactions.

4.5.5 Microfluidics and microscopy for carbon-source operon strains in multi-strain device

For time-lapse microscopy experiments with carbon-source operon strains, another previously developed device was used [146]. This device allows for observation of multiple strains within individual traps that are grown with the same inlet media source without cross-contamination. Carbon source experiments consisted of 24 hour induction periods with various supplemented M9 media.

4.5.6 Serial passaging and plating experiment to estimate plasmid loss rate for carbon-source operon strains

Carbon metabolizing operon strains were grown overnight in 3mL of LB media with chloramphenicol and spectinomycin directly from glycerol stocks. The next day, the overnight culture was washed twice in M9 minimal media and used to inoculate new cultures at a 1:100 dilution in M9 media that was supplemented with Wolfe's Vitamin Solution, MOPS for trace

minerals, and either 0.2% of glucose, arabinose, or lactose (with no antibiotics). The cultures were grown for around 24 hours and passaged 1:100 into fresh, supplemented M9 minimal media that contained the same carbon source that the strain was grown in on the previous day. After 5 passages, samples of the different cultures were plated on LB agar plates containing either no antibiotics, chloramphenicol, spectinomycin, or both antibiotics to determine colony forming units (CFUs). Specifically, to determine CFUs, 3uL droplets of different serial dilutions of the culture were spotted on the agar plates and left to dry before culturing the agar plates at 37C overnight. For each culture, all of the different serial dilutions were plated in triplicate. The following day, CFUs in the culture were determined by counting the number of colonies that formed for the serial dilution that led to between 10 and 30 colonies on average. The number of CFUs in the undiluted culture was then determined by multiplying the number of counted colonies by the dilution factor. Finally, CFUs in antibiotic were divided by the total CFUs found on just LB to determine plasmid retention.

4.5.7 Serial passaging and plating experiment to estimate population fraction of duplicate versus single carbon-source operon strains in competition

Duplicate origin carbon-source strains and single colE1 arabinose plasmid strains were grown separately overnight in supplemented M9 arabinose. They were then diluted 1:100 fold and co-cultured at an equal ratio in fresh M9 arabinose media with no antibiotics. Similar to the spot dilution method described for plasmid loss estimation, cultures were passaged every 24 hours and a sample was plated onto LB plates containing no antibiotic or spectinomycin. The next day colonies were counted to determine CFUs for all strains on LB or just the duplicate origin strain on LB-spectinomycin. Fraction of the population retaining the duplicate origin strains was then calculated each passaging day for 4 days.

4.5.8 Serial passaging and memory quantification of inducible Kan strains in plate reader

For memory experiments with inducible Kan strains, overnight cultures were diluted 1:100 into selective media conditions containing AHL (0-100nM) and Kanamycin (1-15x) within a 96-well plate. After 12 hrs of growth, cells were diluted into 1x kanamycin, 0nM AHL media in a fresh 96-well plate. Three non-selective passages of 12 hrs each were carried out prior to incubation of cells in flipped selective media conditions. This selective phase exposed each culture to the opposite condition as the initial selective phase, for example cultures first incubated at 100nM AHL, 1x Kan were now exposed to 0nM AHL, 15x Kan. Following this secondary selective incubation, three more non-selective passages of 12 hrs each were performed. GFP/OD measurements were then plotted over time and each non-selective memory phase was fit to an exponential curve to determine the memory time constant (return rate) following GFP response.

4.5.9 Microfluidics and microscopy for inducible lysis strains in concentration gradient device

For time-lapse microscopy experiments with the inducible cell lysis strains, a previously developed microfluidic device was used [17]. This device consists of separate arrays of small cell traps that are maintained at different inducer concentrations depending on the inducer concentrations in two upstream inlet channels of the device.

4.5.10 Image analysis of inducible lysis strain timelapse microscopy experiments

To quantify population fluorescence from microfluidics experiments, we developed a FIJI macro. This macro created ROIs around each individual trap, thresholded fluorescence in each

channel to select only healthy cells, merged these ROIs and measured mean intensity for each time slice. One value each for threshold minimum and maximum was set for an entire experiment to avoid non-cell background and also exclude unhealthy filamentous cells. Post processing of results also included background value subtraction for each trap and time slice.

4.5.11 Microfluidics and microscopy for inducible lysis strains in multi-strain device

For time-lapse microscopy experiments with inducible lysis strains for memory investigation, the multistrain chip described previously was used again. Lysis memory experiments consisted of 12 hour induction periods with either non-selective LB-0.2% glucose media, 100nM AHL media, or 0.02% arabinose media. Duplicate ori and different ori strains were imaged during the same experimental run.

4.5.12 Plasmid Copy Number Model

$$P_{rep} = r_2 \left(1 - \frac{p(t)}{p_{tot}}\right) \quad (4.1)$$

$$P_{death} = \frac{N^2}{N^2 + S^2} + d_{1max} \left(\frac{p_1^n}{p_1^n + K_{d1}^n}\right) + d_{2max} \left(\frac{p_2^n}{p_2^n + K_{d2}^n}\right) \quad (4.2)$$

$$P_{division} = g_{max} \left(1 - \frac{N}{C}\right) * \left(\frac{p_1^n}{K_{b1}^n + p_1^n}\right) \left(\frac{K_{c1}^n}{K_{c1}^n + p_1^n}\right) * \left(\frac{p_2^n}{K_{b2}^n + p_2^n}\right) \left(\frac{K_{c2}^n}{K_{c2}^n + p_2^n}\right) \quad (4.3)$$

To study how the plasmid copy number distribution of a population changes over time, we created a stochastic model that takes into account the cost/benefit associated with a given plasmid. The model consists of cells containing two distinct plasmids that can have either the

same or orthogonal mechanisms of replication and copy number maintenance. In each generation the following steps are carried out: 1) plasmids are replicated, 2) some members of the population die (due to plasmid encoded or effects of population saturation), 3) cells have the chance to divide based on plasmid-associated cost-benefit functions, and 4) for dividing cells, plasmids are partitioned to two daughter cells. We assume that the plasmid replication probability is given by Equation 4.1 where r_2 is the maximum replication probability, $p(t)$ is the current plasmid copy number and p_{tot} is the maximum plasmid copy number. For “incompatible plasmids”, p_{tot} is the same between plasmids whereas for compatible plasmids, each plasmid has its own maximum copy number. The number of plasmids that replicate in a given cycle is a random number from the binomial distribution with probability P_{rep} and $p(t)$ trials.

Equation 4.2 describes the probability for a given cell to die based off its current plasmid copy numbers. The first term represents death probability due to general saturation effects as the population size approaches the carrying capacity C . The parameter S represents the population size where the death probability due to culture saturation is half maximal. The two subsequent terms represent death probability due to lysis gene expression from plasmids p_1 and p_2 respectively. Death probability due to plasmid gene expression is assumed to follow the Hill Equation where K_d represents the plasmid copy number that leads to half-maximal death probability and d_{max} represents the maximum death probability.

Division probability is calculated in a similar manner to death probability as shown in Equation 4.3. In this equation, we assume logistic growth of the bacterial population where g_{max} is the maximum division probability and C is the carrying capacity. Each plasmid p_1 and p_2 is assumed to have a potential benefit and cost that can increase or decrease the division probability. The Hill Equation is used to model plasmid cost-benefit effects where for each plasmid K_b represents the plasmid copy number that leads to half-maximal benefit and K_c represents the plasmid copy number leading to half-maximal cost. A cell divides if a number of one is randomly chosen from a binomial distribution with probability $P_{division}$ and one trial. If a cell is chosen to

divide, its plasmids are partitioned to two daughter cells binomially.

4.6 Supplementary Videos

4.6.1 Supplementary Video 4.1

Representative time-lapse microscopy images for duplicate origin carbon operon strain grown in multi-strain microfluidic device with different media types.

4.7 Acknowledgments

This chapter contains material being prepared for submission as: Lezia, Andrew*, Kumar, Shalni*, and Hasty, Jeff. “Burden-minimizing Adaptation of Populations with Duplicate Origin Plasmid Pairs”. (*equal contribution) The dissertation author was one of the primary authors and researchers of this material.

Chapter 5

A standardized set of MoClo-compatible inducible promoter systems for tunable gene expression in yeast

5.1 Abstract

Small-molecule control of gene expression underlies the function of numerous engineered gene circuits that are capable of environmental sensing, computation and memory. While many recently developed inducible promoters have been tailor-made for bacteria or mammalian cells, relatively few new systems have been built for *S. cerevisiae*, limiting the scale of synthetic biology work that can be done in yeast. To address this, we created the yeast Tunable Expression Systems Toolkit (yTEST), which contains a set of three extensively characterized inducible promoter systems regulated by the small-molecules doxycycline, abscisic acid, and asunaprevir/grazoprevir. Assembly was made to be compatible with the modular cloning yeast toolkit (MoClo-YTK) to enhance ease of use and provide a framework to benchmark and standardize each system. Using this approach, we built multiple systems with maximal expression levels greater than those of the

strong constitutive TDH3 promoter and fold changes as high as nearly 300. Thus, yTEST provides a reliable, diverse and customizable set of inducible promoters to modulate gene expression in yeast for applications in synthetic biology, metabolic engineering and basic research.

5.2 Introduction

Inducible promoters are versatile and widely-used molecular tools. By allowing gene expression to be extrinsically and dynamically controlled, these systems can be applied to perturb endogenous regulatory networks [160,161] and build complex genetic devices [50,162]. Inducible promoters for *S. cerevisiae* include a number of native and non-native systems that are responsive to small molecules [160,163–169], however, many have significant drawbacks that limit their utility. While native promoters such as pGAL1 and pCUP1 are often used [44] to control downstream genes with galactose [170] or copper [171], respectively, the use of nutrients as inducers can lead to unwanted pleiotropic effects on cellular physiology [172,173]. Likewise, although bacterial repressors can be used to create inducible systems in eukaryotes by blocking transcription from constitutive promoters in the absence of small molecules that inhibit their DNA binding activity to operator sequences [165,166,174,175], these systems are challenging to tune and can have high basal expression levels. Despite recent work by Chen et al. [165], which expanded the ability of bacterial repressors to function in yeast, many accessible and broadly used inducible systems in *S. cerevisiae* still employ synthetic transcription factors with both DNA binding (DB) and transcriptional activation (TA) domains that turn on gene expression from synthetic minimal promoters [161]. These systems include two categories: Inducer-OFF activators, which initiate gene expression in the absence of inducer, and Inducer-ON activators, which initiate gene expression in the presence of inducer.

In yeast, multiple Inducer-OFF and Inducer-ON systems have been made with components from bacteria, viruses and human cells. Fusing bacterial repressors such as TetR or PhIF to one

or more repeats of the herpes simplex virus VP16 TA domain produces Inducer-OFF activators where gene expression is inversely correlated with the level of tetracycline or doxycycline (Dox) [176, 177] and 2,4-diacetylphloroglucinol (DAPG) [164, 165] respectively. The Dox-responsive system, referred to as Tet-Off, was one of the earliest systems of this kind, and its transcription factor is known as the tetracycline transactivator (tTA) [177]. Through mutagenesis-based approaches [176] Inducer-OFF activators that use bacterial repressors as their DNA binding and inducer sensing elements have been converted into Inducer-ON activators. Notably, mutations to the TetR component of tTA resulted in the reverse tetracycline transactivator (rtTA) and thereby Tet-On [176, 178], an Inducer-ON system where gene expression is activated by the addition of Dox, instead of by its removal. Recently, mutations introduced into two other bacterial transcription factors, PhlF and LuxR, have successfully yielded Inducer-ON activators responsive to DAPG and N-(β -Ketocaproyl)-L-homoserine lactone (HSL), respectively [164].

In addition to mutating bacterial repressors, it is also possible to create Inducer-ON activators via rational design by utilizing the natural functions of certain proteins. The yeast beta-estradiol inducible systems [167–169, 179] are prominent examples of the successes of this strategy. Here, transcriptional activators were engineered to be beta-estradiol inducible by fusing a human estrogen receptor between their DB and TA domains [167–169, 179]. Binding of beta-estradiol to the receptor domain causes the synthetic transcription factor to translocate from the cytoplasm into the nucleus where it then activates gene expression [169]. This function mimics the natural ability of beta-estradiol to bind to and regulate nuclear localization of proteins containing its hormone-binding domain in human cells [179]. As an inducible system in yeast, the beta-estradiol system has gone through multiple design iterations [167–169, 180], and has been used in numerous applications [160, 167, 181]. In addition, a similar inducible activator responsive to human hormone progesterone was recently made [167]. Together, these features further underscore the potential of the rational design approach in creating Inducer-ON activators and highlight how natural proteins or even synthetic systems originally designed for use in

higher eukaryotes can be redesigned to function in yeast. Indeed, further application of these approaches is needed as improving existing inducible systems and creating new ones would be highly beneficial for several reasons.

Firstly, some inducers of the recently reported Inducer-ON systems may be toxic to yeast at relevant concentrations. For the HSL-On [164] and DAPG-On [164, 166] systems, their inducers, HSL and DAPG, have been shown to alter yeast budding patterns [182] and negatively impact mitochondrial metabolism and growth [183], respectively, although these effects of DAPG have been mild in other studies [166], despite it being an antifungal agent [183]. Secondly, as even seemingly benign molecules like Dox can impact cells [176, 184], there is an opportunity to expand the number of available Tet-On systems in yeast as several next-generation or advanced rtTA variants with greater sensitivities [176] have been reported for mammalian cells. Thirdly, different inducers may be ill-suited for certain applications. For example, beta-estradiol and progesterone systems may not function within polydimethylsiloxane (PDMS) microfluidic devices, as PDMS rapidly sequesters hydrophobic molecules such as hormones [185]. Fourthly, expanding the number of orthogonal inducible activators for yeast—thereby emulating earlier efforts in bacteria [186]—would enable small-molecule control of more individual genes and facilitate the construction of larger genetic circuits, which often use inducible promoters as “sensors” that act as inputs [50, 162, 165]. Finally, using and comparing different published systems is often complicated by a lack of standardization [187], since disparate promoters, terminators, fluorescent reporters, genome integration sites and yeast strains can be used for their construction and testing. For these reasons, it is clear that there is a need to increase both the quantity and accessibility of inducible promoter systems, and that doing so would offer greater flexibility for yeast researchers to select the system that best suits their experimental needs.

Here we address the shortcomings in available options for inducible promoter systems in *S. cerevisiae* by developing the yeast Tunable Expression Systems Toolkit (yTEST). By using the existing literature to identify cutting-edge inducible promoter systems for mammalian

cells, we redesign several of them to achieve robust performance in budding yeast. The three systems included in this kit consist of advanced rtTA variants regulated by Dox as well as inducible promoters regulated by the plant hormone abscisic acid (ABA) and antiviral compounds asunaprevir and grazoprevir (ASV/GZV). By increasing the number of inducible promoters for *S. cerevisiae*, yTEST can potentially facilitate new applications in molecular and synthetic biology.

5.3 Results

5.3.1 A Modular Cloning Framework for Constructing Standardized Inducible Systems

To expand the catalog of inducible activators for budding yeast, we leveraged the comparatively larger list of these systems created for use in Chinese hamster ovary (CHO) or human cells. As previously mentioned, several new rtTA variants with improved basal and maximal expression levels [176] are now frequently used in mammalian cells, although, to our knowledge, many of these new variants have not been systematically tested in yeast. Indeed, this is true of many novel Inducer-ON systems recently developed for mammalian cells, which rely on small-molecule inducers such as ABA [188–190], caffeine [191], rapamycin [192] and the antiviral compounds ASV/GZV [189, 193]. Given the functionality and robustness demonstrated by these systems in higher eukaryotes, we set out to systematically and quantitatively test their effectiveness in budding yeast. Since caffeine and rapamycin are known to inhibit growth in *S. cerevisiae* [194], we focused on creating Dox inducible systems with three of the most advanced rtTA variants, as well ABA and ASV/GZV inducible systems.

To optimize these systems for yeast, we utilized the modular cloning (MoClo) yeast toolkit (YTK) made by Lee et al [44]. The MoClo yeast toolkit, or MoClo-YTK, contains a diverse set of 8 different categories of parts—including constitutive promoters, terminators and

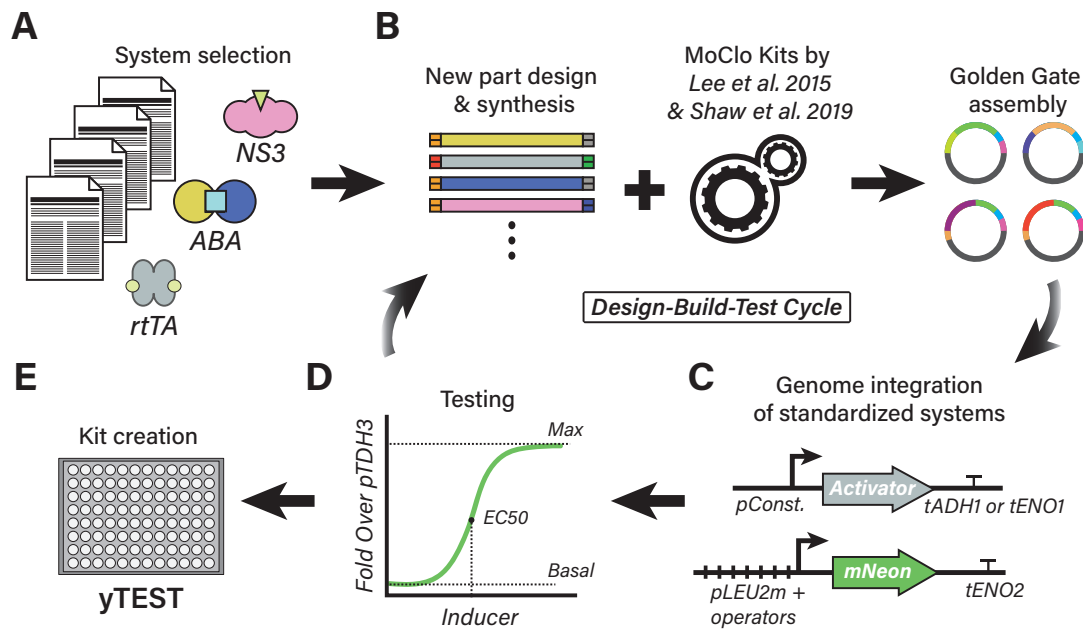


Figure 5.1: Workflow for developing yTEST. (A) Candidate inducible promoters were identified in the literature from recently reported mammalian cell systems. Three advanced rtTA variants, the ABA system and the NS3 system were selected for testing in yeast. Doxycycline, abscisic acid and asunaprevir/grazoprevir, respectively, are the small molecules that control these systems. (B) Parts for each system were yeast codon optimized, formatted as the appropriate MoClo-YTK part type and synthesized. New parts were combined with existing MoClo-YTK parts (Lee et al. [44]) and parts from the Yeast GPCR-sensor Toolkit (Shaw et al. [180]), through Golden Gate assembly reactions to form cassette plasmids. (C) Each followed a standard format: constitutive promoters (pConst.) expressed the inducible activators, a minimal LEU2 promoter [180] with operator sites (pLEU2m+operators) drove the mNeonGreen (mNeon) reporter gene, ADH1 or ENO1 terminators were used for cassettes containing activators and the ENO2 terminator was used in mNeon reporter cassettes. All constructs were chromosomally integrated. (D) Promoters were tested in yeast and induction curve properties were quantified. Induction fluorescence was expressed relative to pTDH3-mNeon- tENO2. Systems were improved via a design-build-test build cycle at this stage. (E) yTEST contains the validated parts, expression cassettes and plasmids from this process.

plasmid backbones— that are referred to as Types and each contain unique 4 bp overhangs that enable them to be combined via the Golden Gate reaction-based modular cloning system [61]. Further, new parts can be formatted in this way and used interchangeably with other parts in the kit, enabling the creation of entirely new MoClo-YTK-based kits for specific applications, such as the Yeast GPCR-sensor Toolkit made by Shaw et al. [180], which provides parts for engineering GPCR signaling networks. Thus, MoClo-YTK provides an expandable foundation that enables rapid cloning, testing, and troubleshooting of customizable genetic constructs; ideal features for creating and tuning novel inducible promoter systems. Using MoClo-YTK as our basis, we sought a standardized approach for designing and benchmarking inducible activators. All components needed for the inducible promoters relying on Dox, ABA and ASV/GZV were first identified from recently published work (Figure 5.1A). Following MoClo-YTK guidelines, we designed and created new parts needed for testing each of these three systems, then cloned them, along with other necessary parts from MoClo-YTK and the Yeast GPCR-sensor Toolkit, into cassette plasmids (Figure 5.1B). We used a consistent design format for each cassette and integrated them into the genome (Figure 5.1C) in order to minimize variability and enable comparisons within and between the three systems after measuring the response of each to its inducer (Figure 5.1D). For analysis, fluorescence values were expressed relative to those of the TDH3 promoter driving mNeon (pTDH3-mNeon-tENO2), as pTDH3 is a commonly used strong promoter and Lee et al. found it to be the strongest constitutive promoter in the MoClo-YTK. After testing and verification, all components needed to use these systems were aggregated to create yTEST and facilitate broader use (Figure 5.1E).

The individual parts included in yTEST consist of major protein coding and DNA binding sequences that fall into the part Types 2A, 3, 3A, 3B and 4A. (Figure 5.2). As noted above, since yTEST was designed to work within the MoClo-YTK framework and alongside similar kits, complete assembly from individual parts of the three inducible systems described here also requires parts from MoClo-YTK and the Yeast GPCR-sensor Toolkit. Importantly, this includes

rtTA systems		ABA systems		NS3 systems		Reporter	
Part	Type	Part	Type	Part	Type	Part	Type
rtTA3	3	phlfO7	2A	NS3	3B	mNeonGreen	3
rtTA-v10	3	PhlF-NES	3A	VP48	4A	pLEU2m	2B
rtTA-v16	3	NLS-VP48	3A	VP48-2XOaf1	4A		
tetO7-pLEU2m	2	NLS-VP48-1XOaf1	3A	lexAO6	2A		
		NLS-VP48-2XOaf1	3A	LexA-NLS	3A		
		ABI	3B				
		PYL1	3B				

Part from Yeast-GPCR Sensor Toolkit

Part from Yeast-GPCR Sensor Toolkit

Parts from Yeast-GPCR Sensor Toolkit

Part from Yeast-GPCR Sensor Toolkit

Figure 5.2: Parts included in yTEST. The Dox inducible rtTA systems consist of parts for DNA binding (Type 2A) that contain 7 repeats of the Tet operator sequence (tetO7) and several advanced rtTA variants (Type 3). The abscisic acid (ABA) inducible systems use Type 2A parts with 7 repeats of the PhlF operator sequence (phlfO7), DB (PhlF-NES) and TA (NLS-VP48, NLS-VP48-1XOaf1, NLS-VP48-2XOaf1) domain Type 3A parts and Type 3B parts for controllable heterodimerization (ABI and PYL1). The NS3 systems use a Type 3B NS3 domain for inducible control with asunaprevir/grazoprevir and Type 4A parts for TA domains (VP48, VP48-2XOaf1). The NS3 system requires two parts from the Yeast GPCR-sensor Toolkit by Shaw et al.²³, the Type 2A parts with 6 repeats of the LexA operator sequence (lexAO6) and the Type 3A LexA-NLS part for DNA binding. For testing all systems, a Type 3 mNeonGreen fluorescent reporter was used and the Type 2B pLEU2m from the Shaw et al. Yeast GPCR-sensor Toolkit was used as the core promoter for all three systems. Where noted NLS and NES indicate nuclear localization and nuclear export sequences added to parts, respectively.

the minimal LEU2 promoter [180] (pLEU2m) from the Yeast GPCR-sensor Toolkit, which we use as the core promoter for each system, as Shaw et al. demonstrated that pLEU2m exhibits superior induction properties compared to other minimal promoters, including the often-used CYC1 minimal promoter.

5.3.2 Doxycycline Inducible Systems with Advanced rtTA Variants

The rtTA component of the Tet-On system has been in a continual state of improvement in mammalian cells. While Roney et al. [195] adapted the rtTA-M2 variant for use in yeast, which includes several mutations that improve its functionality relative to the original rtTA [196], and produced multiple variants with mutations further enhancing its function, there has been no direct comparison among the most advanced systems used in mammalian cells. These principally

include the variants rtTA3, based on work by Das et al. [197], and rtTA-v10 (also known as Tet-3G19) and rtTA-v16 from Zhou et al [198], which contain different mutations and, in the case of rtTA3, different TA domains (Fig. 5.7). Therefore, we set out to systematically test each of these variants in yeast and evaluate the tradeoffs each provides in terms of sensitivity to Dox, basal expression, maximal expression, and fold change.

To tune each system, we placed rtTA3, rtTA-v10 and rtTA-v16 under the control of constitutive promoters of various strengths (Fig. 5,8) and tested the induction properties of each configuration using tetO7-pLEU2m driving mNeon (Figure 5.3A). We started with the medium strength constitutive promoter pRPL18B, and found that all three systems showed increases in expression of the mNeon reporter as Dox levels increased (Figure 5.3B), as expected. The rtTA3 and rtTA-v10 systems exhibited relatively low basal expression levels in the absence of Dox that were 1.2 and 5.1X higher than background levels in BY4741 strains without any fluorescent proteins (Figure 5.3E) and had maximal expression levels 1.2 and 2.1X that of pTDH3-mNeon (Figure 5.3B, E and F), respectively. Meanwhile, the rtTA-v16 system exhibited both high maximal and basal expression levels, with the latter even exceeding the levels achieved by pTDH3-mNeon (Figure 5.3B, E and F). Indeed, similar results for this system were previously obtained in mammalian cells, where cells transiently transfected with non-integrating plasmids exhibited high basal expression levels [176]. As a result, we decided to further test each of the three variants by increasing the strengths of the promoters expressing rtTA3 and rtTA-v10, and decreasing the strength of the promoter expressing rtTA-v16.

To accomplish this, we used pTDH3 to drive rtTA3 and rtTA-v10, and the weak promoters pRNR2 and pRAD27 to drive rtTA-v16. Using pTDH3 led to only modest increases in maximal expression relative to pRPL18B: 20.6% for rtTA3 and 4.2% for rtTA-v10. However, this change in promoter had large effects on basal expression levels, which increased approximately 10-fold for rtTA3 and 2-fold for rtTA-v10 (Figure 5.3C, E and F). On the other hand, the use of either pRNR2 or pRAD27 in combination with rtTA-v16 substantially reduced basal expression levels

for this system by more than 20-fold compared to when used with pRPL18B (Figure 5.3E). Further, maximal expression levels remained high, with both promoters allowing rtTA-v16 to still achieve approximately 2X higher maximal levels than pTDH3-mNeon. In total, pRPL18B-rtTA3 resulted in the system with the greatest fold change, reaching maximal levels nearly 120 times that of its basal levels (Figure 5.3G). The pRNR2-rtTA-v16 and pRPL18B-rtTA-v10 systems also had high fold changes of 38 and 47-fold, respectively (Figure 5.3G). In terms of sensitivity to Dox, the rtTA-v16 and rtTA-v10 systems were able to respond to much lower Dox concentrations than the rtTA3 systems (Figure 5.3H). The EC₅₀ value for the most sensitive rtTA system (excluding pRPL18B-rtTA-v16), pRNR2-rtTA-v16, was 27.5 nM while the EC₅₀ for the least sensitive system, pRPL18B-rtTA3, was 136.1 nM, nearly a 5-fold increase.

When considered together, the Dox inducible systems described here offer a spectrum of choices where systems with multiple induction properties can be utilized. For example, the highly Dox sensitive pRNR2-rtTA-v16 system would likely be most useful for applications requiring prolonged continuous induction, such as replicative aging experiments which are carried out over the course of several days in microfluidic devices [199], in order to limit the amount of Dox that cells are exposed to while still offering tight control and strong maximal expression. Alternatively, pRPL18B-rtTA3 would be preferred when limiting basal expression is paramount, such as cases where even low levels of a gene can produce a large effect. As an example, in the genome-wide screen performed by Arita et al [160], they found that basal expression levels from their beta-estradiol inducible system were high enough that when certain essential genes were placed under inducible control, growth was permitted even in the absence of beta-estradiol. This promoted them to redesign their beta-estradiol system to reduce its basal expression. Thus, having multiple options, even for systems using the same inducer, can be highly useful.

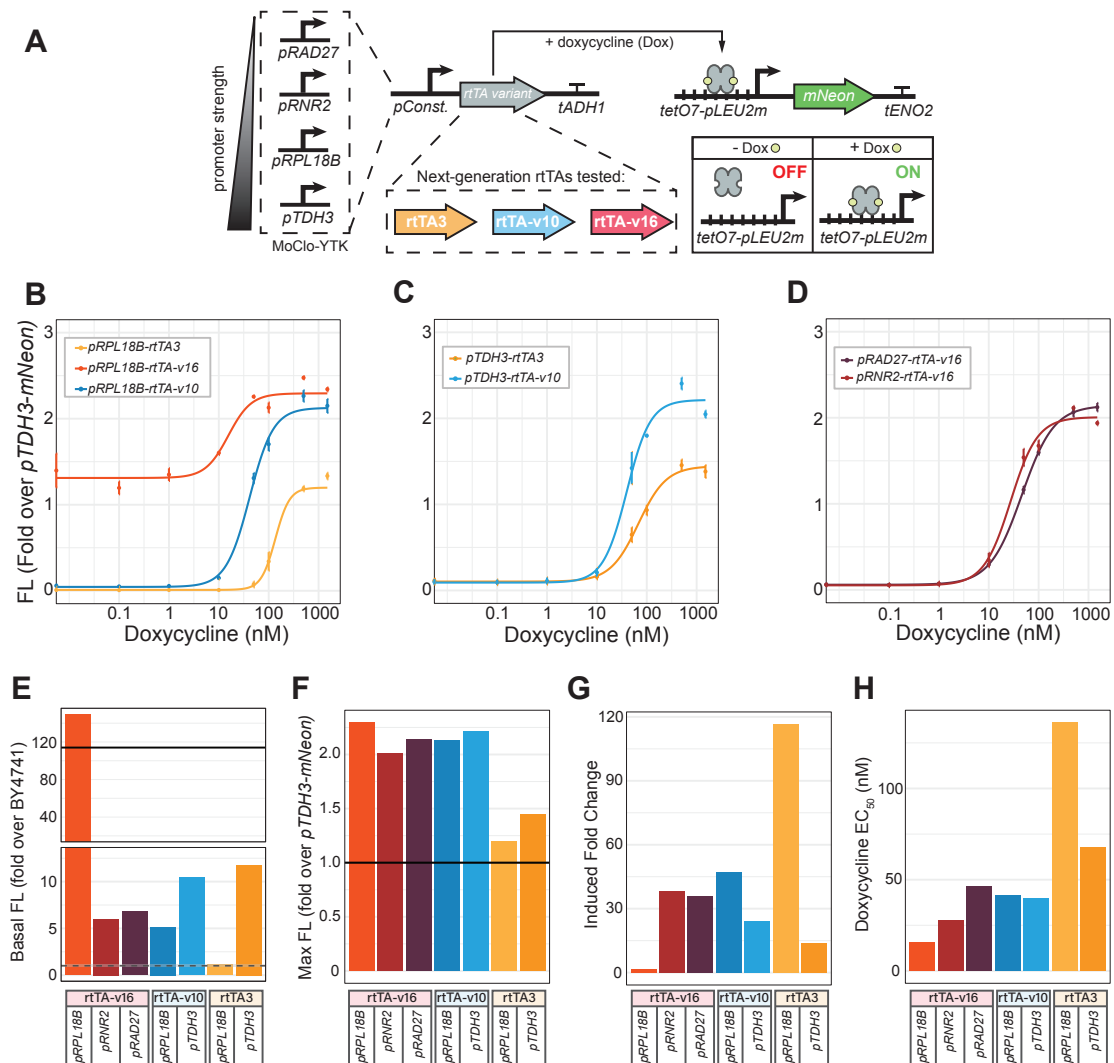


Figure 5.3: Design and induction properties of rtTA Dox inducible systems. (A) The advanced rtTA variants rtTA3, rtTA-v10 and rtTA-v16 are tested by tuning their expression levels with MoClo-YTK promoters pRAD27, pRNR2, pRPL18B and pTDH3. Binding of Dox to the rtTA variants allows them to bind to tetO7-pLEU2m and express the mNeon fluorescent reporter. (B) Induction curves of the three variants driven by pRPL18B. (C) Induction curves of rtTA3 and rtTA-v10 driven by pTDH3. (D) Induction curves of rtTA-v16 driven by pRAD27 and pRNR2. Fluorescence (FL) values for each induction were normalized relative to mNeon fluorescence when constitutively expressed by pTDH3 (pTDH3-mNeon). Circles represent mean values from $n=3$ replicates and error bars represent standard deviation (SD). (E) Basal FL levels of all tested rtTA systems expressed relative to the BY4741 strain not expressing any fluorescent protein. Mean BY4741 FL was normalized to 1 and is indicated by the dashed line. The shaded region represents one s.d. above and below the mean. pTDH3-mNeon FL is indicated by the solid black line. (F) Maximal expression levels of each rtTA system expressed relative to pTDH3-mNeon (solid black line). (G) Fold change values for each rtTA system, calculated by dividing the maximal expression level by the basal expression level. (H) EC₅₀ values for each rtTA system, the Dox concentration at half-maximal expression, indicating the sensitivity of each system to Dox.

5.3.3 ABA Inducible Systems based on ABI and PYL1 Heterodimerization

Having demonstrated that rtTA variants can be efficiently tuned in yeast with a MoClo-YTK-based approach, we wanted to use similar methods to design, build and test ABA inducible systems. ABA is a plant hormone that induces heterodimerization of the proteins ABI and PLY144. Notably, Chang et al. [188] used these properties to create an ABA inducible promoter system in CHO cells that exhibited induction properties similar to those of rtTA3. Their design utilized two constitutively expressed chimeric proteins. One consisted of PhlF, serving as the DB domain, fused to ABI as well as a nuclear export signal (NES), while the other protein contained a nuclear localization signal (NLS), PYL1 and the VP16 TA domain. Given the strong performance of this system in CHO cells, we reasoned that similar performance could be achieved in yeast.

The design of our ABA inducible promoter system generally followed the Chang et al. [188] organization of parts (Figure 5.4A). In order to modulate the induction properties of the ABA system, we tested three different activation domains, starting with VP48, which consists of three repeats of the minimal VP16 TA domain [200]. In this first configuration, a functional inducible promoter was built that responded to micromolar concentrations of ABA (Figure 5.4B and H), exhibited basal expression levels in the absence of ABA that were virtually indistinguishable from BY4741 background fluorescence (Figure 5.4E) and had maximal expression that was 33% of pTDH3 \rightarrow mNeon (Figure 5.4B and F). Despite having maximal expression levels well below pTDH3 \rightarrow mNeon, the system had a 74X fold change (Figure 5.4G) due to its low basal expression levels. The EC50 value of this system was 10.8 μ M (Figure 5.4H).

Moving forward, we reasoned that we could improve this system by increasing the strength of the activation domain. To do this, we fused one or two copies of the activation domain of the yeast transcription factor Oaf1 to VP48, which we denote as VP48-1XOaf1 and VP48-2XOaf1 (Fig. 5.9), respectively. We selected the Oaf1 activation domain because of its potency and compactness; a recent screen by Sanborn et al. [201] identified Oaf1 as having one of the strongest TA domains in yeast, and it was previously shown to consist of just 27

amino acids in its C-terminus [202, 203]. When the VP48-1XOaf1 and VP48-2XOaf1 variants were tested, we noted marked increases in not only the maximal expression levels reached, but also in the sensitivities to ABA (Figure 5.4C and D). Basal expression levels for VP48-1XOaf1 remained nearly identical to the original ABA system using VP48 as well as to the background fluorescence levels measured for BY4741 (Figure 5.4E), while maximal levels were 1.5X higher than pTDH3-mNeon (Figure 5.4F), yielding a fold change of nearly 300X for this system and representing a more than 350% improvement in fold change relative to the ABA system using only VP48. For the VP48-2XOaf1 system, basal expression was 3.3X higher than BY4741 background levels (Figure 5.4E) and maximum expression was 1.7X that of pTDH3-mNeon (Figure 5.4F), resulting in a fold change of 77. In terms of sensitivity to ABA, when compared to the original VP48 system, the addition of 1XOaf1 or 2XOaf1 to the activation domain decreased the EC50 values by 96% and 98%, respectively, (Figure 4H). The EC50 of the VP48-2XOaf1 variant (190 nM) was less than half that of the VP48-1XOaf1 variant (403 nM).

From these results, it is clear that robust ABA inducible promoters can be built in yeast and that tuning the strength of the activation domain allows a wide range of dose-response properties to be realized. Further, by holding all parts of the system constant and only increasing the strength of the TA domain, we demonstrated that tradeoffs can exist between maximal expression, sensitivity and basal expression. While the addition of 1XOaf1 to VP48 dramatically improved the maximal expression and sensitivity at little cost to the basal expression levels (a 13.5% increase), further improvement of VP48-1XOaf1 by adding an additional Oaf1 TA domain resulted in a 10.5% increase in the max and 52.8% decrease in the EC50 but concomitantly increase the basal expression by more than 320%. These findings underscore the need for a multitude of easily customizable inducible systems to be made widely available, as it is unlikely that a single system possesses ideal characteristics across all performance metrics.

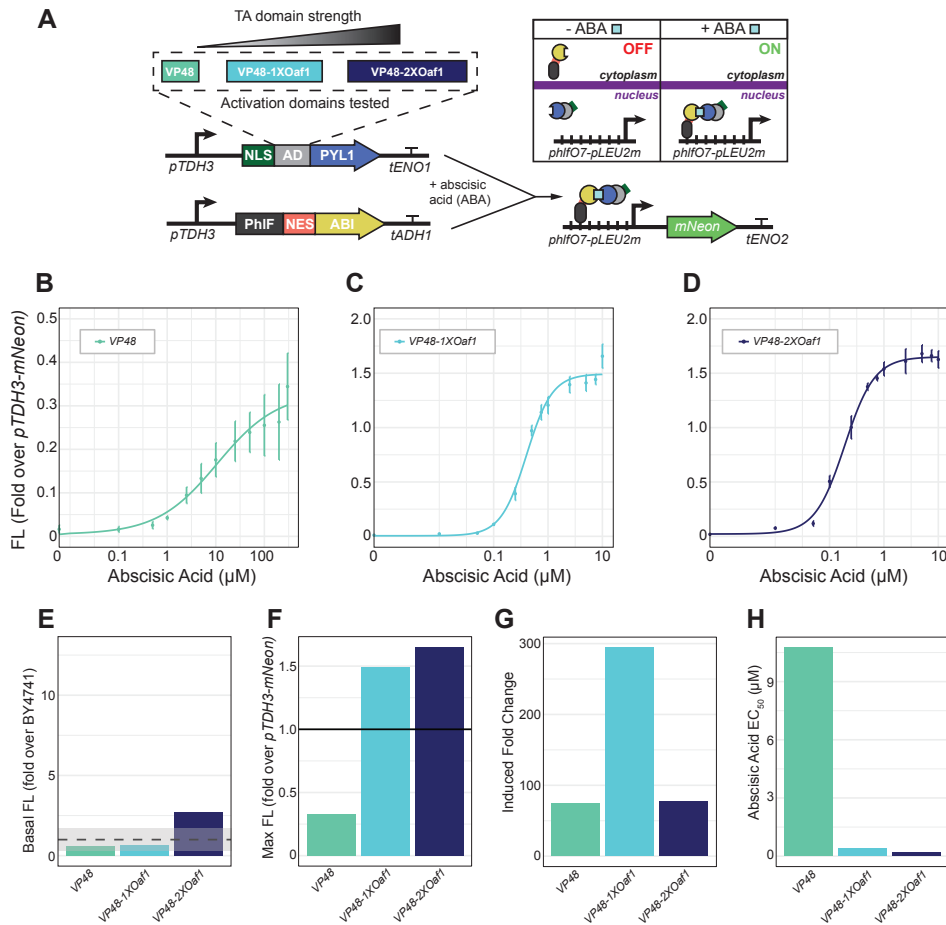


Figure 5.4: Design and induction properties of ABA inducible systems. (A) Two fusion proteins, one composed of PhlF an NES and ABI and the other composed of an NLS, PYL1 and a TA domain, were placed under the control of pTDH3. The NES on the ABI fusion protein promotes its export from the nucleus in the uninduced state, limiting its interactions with the PYL1 fusion protein which harbors an NLS and localizes to the nucleus. For expression of mNeon, pLEU2m fused to 7 repeats of the PhlF operator sequence (phlF07-pLEU2m) was used. ABA promotes heterodimerization of the ABI and PYL1 chimeric proteins, allowing the complex to bind to phlF07-pLEU2m and express mNeon. Three different activation domains were tested: VP48, VP48-1XOaf1 and VP48-2XOaf1. (B) Induction curve of the ABA system with VP48 as the activation domain. (C) Induction curve of the ABA system with VP48-1XOaf1 as the activation domain. (D) Induction curve of the ABA system with VP48-2XOaf1 as the activation domain. Fluorescence (FL) values for each induction were normalized relative to mNeon when constitutively expressed by pTDH3 (pTDH3-mNeon). Circles are mean values from n=4 replicates and error bars are SD. (E) Basal FL levels of ABA systems with each of the three different activation domains tested and expressed relative to the BY4741 strain not expressing any fluorescent protein. Mean BY4741 FL (dashed line) was normalized to 1. The shaded region represents one SD above and below the mean. (F) Maximal expression levels of each ABA system expressed relative to pTDH3-mNeon (solid black line). (G) Fold change values for each ABA system (maximal expression divided by basal expression). (H) EC₅₀ values for each system.

5.3.4 ASV and GZV Inducible Systems based on Controllable NS3 Proteolytic Cleavage

To create a third inducible system that was orthogonal to the rtTA and ABA systems, we built upon work by Tague et al. [193] that used the NS3 serine protease from the hepatitis C virus (HCV) as the basis for constructing an inducible activator in mammalian cells. NS3 denotes a domain within the HCV nonstructural (NS) polyprotein that internally cleaves multiple recognition sites to produce the NS4 and NS5 proteins inside host cells [204]. Several antiviral small-molecules, including ASV and GZV, have been developed to block this critical step in HCV infection and work by binding to NS3 and inhibiting its proteolytic activity [193, 205, 206]. To create an inducible promoter system with these molecules, Tague et al. [193] designed a synthetic transcription factor with NS3 fused to a DB domain on its N-terminus and a TA domain on its C-terminus. Immediately flanking the NS3 domain are its two cleavage sites, termed NS4A/4B and NS5A/5B, which are cut in the absence of antiviral drugs, thereby stopping the association of the DB and TA domains of the transcription factor and preventing it from activating gene expression. However, when the antivirals are added to this system they enable NS3 to act as a ligand-inducible connector, as cleavage at the NS4A/4B and NS5A/5B sites is inhibited and the intact transcription factor can successfully switch on gene expression.

To port this system into yeast, we designed a Type 3B part that includes a yeast codon optimized version of the NS3 domain and flanking NS4A/4B and NS5A/5B cut sites from Tague et al. (Fig. 5.10). For the TA and DB domains, we used VP48-2XOaf1 (validated for the aforementioned ABA system) and the bacterial LexA transcription factor from the Yeast GPCR-sensor Toolkit, respectively (Figure 5.5A). Upstream of pLEU2m driving the mNeon fluorescent reporter, we used lexAO6, featuring six copies of the LexA operator sequence, a Type 2A part that also came from the Yeast GPCR-sensor Toolkit (as did pLEU2m). After assembling these parts into cassettes and integrating them into yeast, we tested the performance of the NS3 system

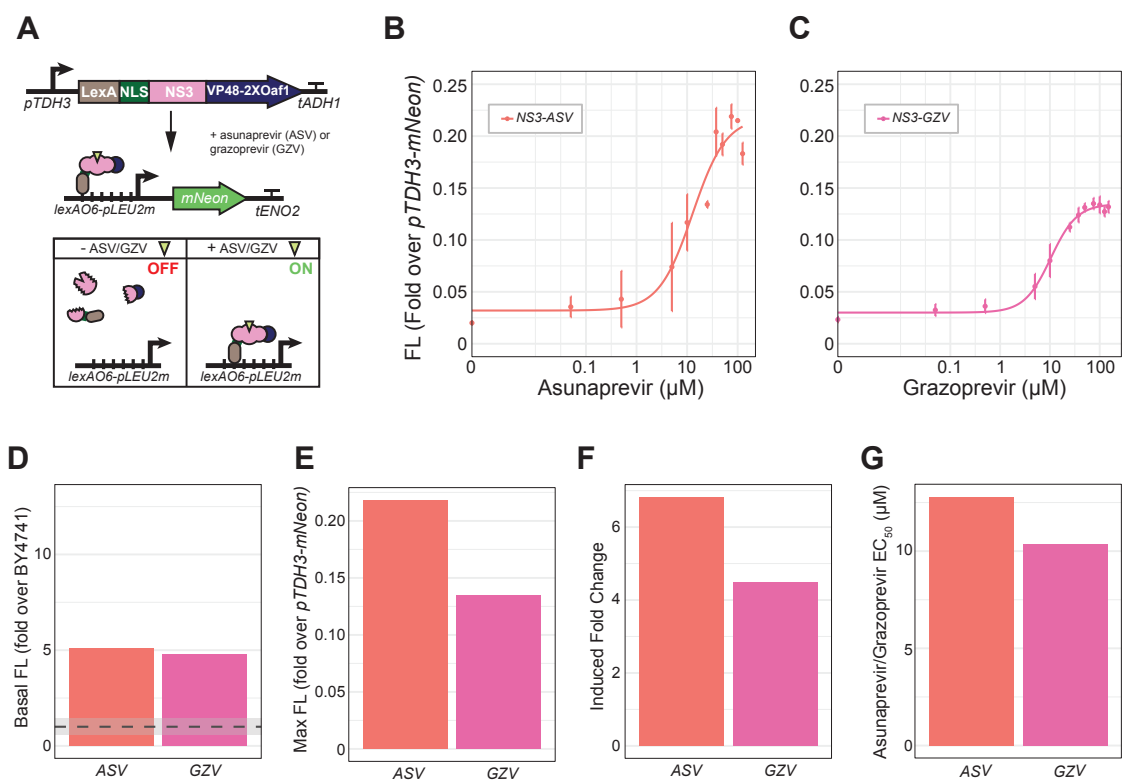


Figure 5.5: Design and induction properties of NS3 inducible system. (A) The transcriptional factor for the NS3 system consisted of LexA-NLS (from the Yeast GPCR-sensor Toolkit [180]) as the DB domain and VP48-2XOaf1 as the TA domain. Responsiveness to ASV and GZV was made by placing NS3, its cofactor NS4A, and its two cut sites, NS5A/5B and NS4A/4B, between the DB and TA domains. In the absence of ASV or GZV, NS3 cleaves the NS5A/5B and NS4A/4B sites towards its N-terminus and C-terminus, respectively, severing the transcription factor and preventing transcription of mNeon from *lexAO6-pLEU2m* (from Yeast GPCR-sensor Toolkit). (B) Induction curve of the NS3 system with ASV as the inducer (n=3 replicates). (C) Induction curve of the NS3 system with GZV as the inducer (n=4 replicates). Fluorescence (FL) values for each induction were normalized relative to pTDH3-mNeon. Circles are mean values and error bars are SD. (E) Basal FL levels of the NS3 system when induced by ASV and GZV and expressed relative to the BY4741 strain not expressing any fluorescent protein. Mean BY4741 FL (dashed line) was normalized to 1. The shaded region represents one SD above and below the mean. (F) Maximal expression levels of the NS3 system when induced by ASV and GZV (relative to pTDH3-mNeon indicated by the solid black line). (G) Fold change values for the NS3 system when induced by ASV and GZV (maximal expression divided by basal expression). (H) EC₅₀ values for the NS3 system for ASV and GZV induction.

using two antiviral small-molecule drugs, ASV and GZV, and saw increased mNeon fluorescence in response to increased concentration of both compounds (Figure 5.5B and C). As expected, basal levels were nearly identical (Figure 5.5D) since the same NS3 system was used in each experiment, with only the type of inducer changed. Maximum values reached by both systems were considerably lower than those achieved by the rtTA and ABA systems, reaching only 0.22X that of pTDH3-mNeon for induction with ASV and 0.13X that of pTDH3-mNeon for induction with GZV (Figure 5.5E). As a result, fold changes of only 6.8 and 4.5 were obtained when using ASV and GZV, respectively (Figure 5.5F). In terms of sensitivity to the two different inducers, use of ASV resulted in an EC₅₀ of 12.8 μ M, which was reduced nearly 20% to 10.4 μ M when GZV was used (Figure 5.5G).

While these results demonstrate that it is possible to design an NS3-based inducible promoter system in yeast, the maximal expression levels achieved for this system were considerably lower than those obtained for the best performing rtTA and ABA system variants. For example, pRNR2-rtTA_{v16} and ABA system with VP48-2XOaf1 had maximum levels of 2X and 1.7X those of pTDH3-mNeon, while the highest value for the NS3 system was only 0.22X of pTDH3-mNeon when ASV was used as the inducer. One possible explanation for the lower expression levels observed in the NS3 systems is that the protease activity of NS3 is not fully suppressed in yeast by the ASV and GZV inducers. Indeed, a similar observation was made by Chung et al. [206], who created an NS3-based controllable degron system for protein tagging and degradation termed SMASh (small molecule-assisted shutoff) and found that this system experienced higher levels of NS3 proteolytic activity in yeast than in mammalian cells, even in the presence of ASV. However, the authors were able to ameliorate this problem by using only the NS4A/4B cleavage site in their system, which is cut more slowly by NS3 than the NS5A/5B site, and noted that a potential reason why this change reduced basal expression in yeast when no such change was needed in mammalian cells was that the proteolytic activity of NS3 maybe be higher at 30°C than at 37°C. Therefore, these findings suggest that the maximal expression levels of the NS3 system designed

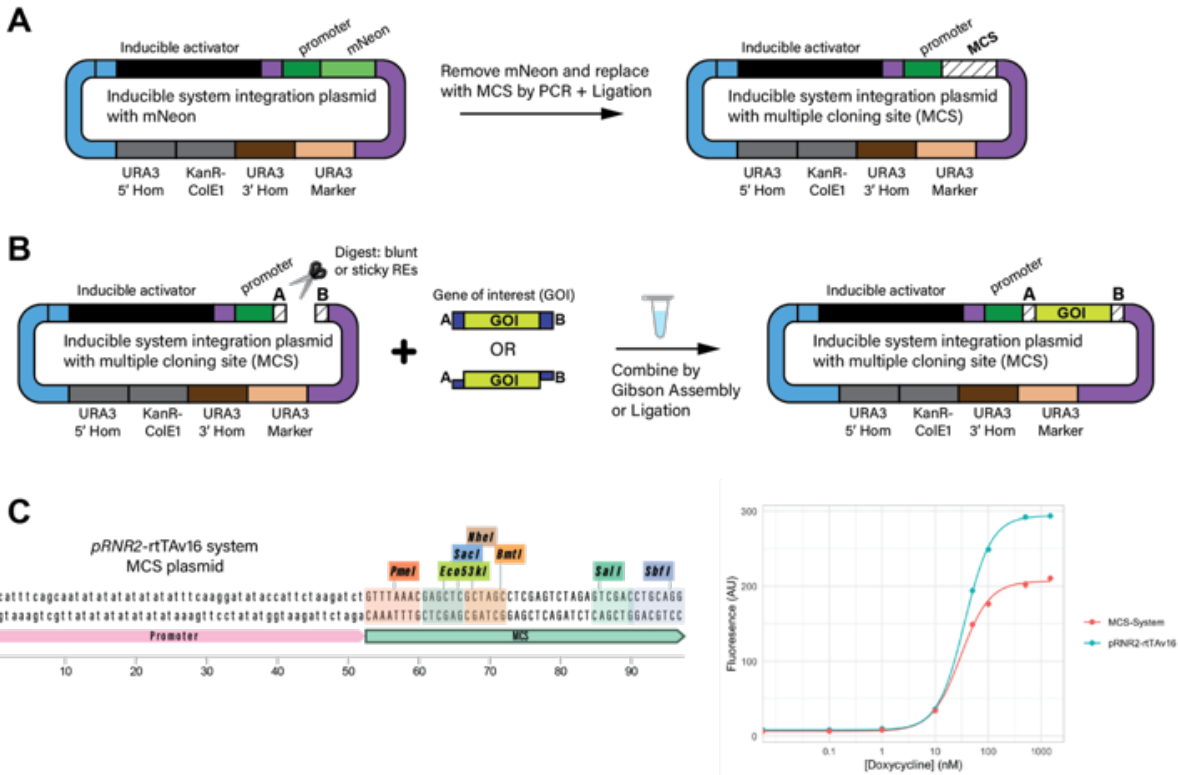


Figure 5.6: Construction and validation of MCS inducible system integration plasmids. (A) For selected systems, mNeon was replaced in the multigene integration plasmid, which contained the inducible activator and promoter, and was replaced by an MCS. (B) MCS plasmids allow restriction enzymes that produced both blunt and sticky ends to be used to insert a gene of interest (GOI) into the plasmid so that its expression can be controlled by the upstream inducible system. Both Gibson Assembly and standard restriction-ligation cloning can be used to insert the GOI. (C) Design of a pRNR2-rtTav16 MCS integration plasmid (left) and validating its function by reinserting mNeon and testing the induction properties of the MCS version of this system compared to the original.

here could potentially be improved by removing the NS5A/5B site in our construct and using two NS4A/4B cleavage sites.

5.3.5 Multiple Cloning Site Plasmids for Rapid and Customizable use of Inducible Systems

While yTEST includes the parts need to assemble inducible systems and modify them to express genes of interest, we realized that some groups may want a simplified method for placing

a gene of their choice under the control of Dox, ABA or ASV/GZV. To address this, we also created versions of the multigene inducible system integration plasmids where a multiple cloning site (MCS) is included in place of mNeon (Figure 5.6A). These MCS integration plasmids make it simple to insert a desired gene by restriction-ligation cloning or Gibson Assembly (Figure 5.6B) and was done for the following systems: pRNR2-rtTAv16, pRPL18B-rtTA3, the ABA system with VP48-2XOaf1 and the NS3 system (Fig. 5.11).

To validate this approach, we re-inserted mNeon into the pRNR2-rtTAv16 MCS integration plasmid by digesting the MCS plasmid with the blunt-end restriction enzyme PmeI, followed by a Gibson Assembly reaction to insert mNeon into the linearized plasmid. We then integrated the resulting construct into yeast and tested its behavior. As expected, we found that the pRNR2-rtTAv16 system was able to express mNeon upon the addition of Dox, however, we saw a smaller maximal response compared to the original plasmid system (Figure 6C). This is potentially due to changes in the 5' UTR from leftover base pairs of the MCS. Existing research suggests that modifications to the 5' UTR can have significant impacts on gene expression levels from synthetic promoters in yeast [207]. Nonetheless, our results suggest that the MCS versions of the inducible system integration plasmids will be a useful tool for researchers who wish to quickly utilize an inducible system in yTEST to control the expression of target gene in yeast.

5.4 Discussion

Inducible promoter systems are widely used by yeast researchers in both molecular and synthetic biology research. However, currently available systems are few in number and lack standardization. Here, we detail the development and characterization of yTEST, an extension of the MoClo-YTK which includes parts for constructing yeast inducible promoter systems with broad ranges of dose-responses to three different small-molecule inducers. Thus, by choosing different systems included in yTEST, different sensitivities to inducers as well as different basal


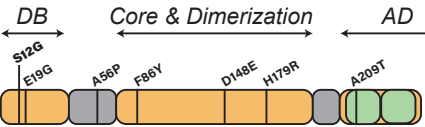




and maximal expression levels can be achieved. This is a critical feature of this kit, as different applications can require very high expression levels of transgenes, digital or analog-like responses to inducers, or tight control of gene expression with minimal leakiness.

The yTEST kit presented here represents part of a growing list of recently reported MoClo-based kits with parts for CRISPR/Cas9 genome engineering [208], optogenetics [209] and signaling pathway modulation [180] in yeast. Future work can further build upon and expand yTEST to include additional inducible promoter systems as well as include other modes of inducible regulation. Further, we also envision that a similar kit for small molecule-controlled protein degradation could be designed for yeast which could include the auxin [210] and thrimethoprim (TMP) [211] inducible protein degradation systems.

Ultimately, we designed and built yTEST with the goal of helping to expand what is possible in yeast synthetic biology. As more extensions of the MoClo-YTK are developed, we expect that the accessible and plug-and-play nature of this assembly framework will result in many innovations that use and combine parts from different kits in unique ways. As a result, *S. cerevisiae* may become increasingly used for synthetic biology applications of the future.

5.5 Supplemental Figures

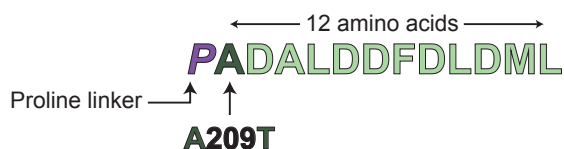
A

Advanced rtTA Variant	Mutations from Original rtTA Protein (Gossen et al., Science 1995)	Sequence References Used
		<ul style="list-style-type: none"> - Das et al., Curr. Gene Ther. 2016 - Das et al., J Biol Chem 2004 - Busskamp et al., Mol. Syst. Biol. 2014, from pTRIPZ Vector (Thermo Fisher Scientific) - Sim et al., Methods Mol. Biol. 2015 - Chang et al., Nat. Chem. Biol. 2019 - Kang et al., J. Anim. Sci. Biotechnol. 2019
		<ul style="list-style-type: none"> - Das et al., Curr. Gene Ther. 2016 - Zhou et al., Gene Ther. 2006 - Liu et al., Cell Stem Cell. 2018 - Dalvai et al., Cell Rep. 2015 - Kang et al., J. Anim. Sci. Biotechnol. 2019
		<ul style="list-style-type: none"> - Das et al., Curr. Gene Ther. 2016 - Zhou et al., Gene Ther. 2006 - Watakabe et al., Front Neural Circuits. 2014

B

 = Minimal VP16 Activation Domain (12 a.a.):

Baron et al., Nucleic Acids Res. 1997:



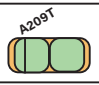
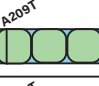
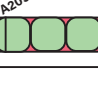
Variant	AD	Description
rtTA3		2X min. VP16 AD
rtTA-v10		3X min. VP16 AD
rtTA-v16		3X min. VP16 AD

Figure 5.7: Comparison of advanced rtTA variants used in this study. (A) Sequences of and mutations in rtTA3, rtTA-v10 and rtTA-v16 with associated references where these variants were either constructed, used or described. (B) Makeup of the activation domains, consisting of two or three repeats of the 12 amino acid VP16 minimal activation domain (min. AD), for each advanced rtTA variant. The first V16 min. AD for each of the three variants tested in this study contains the A209T mutation.

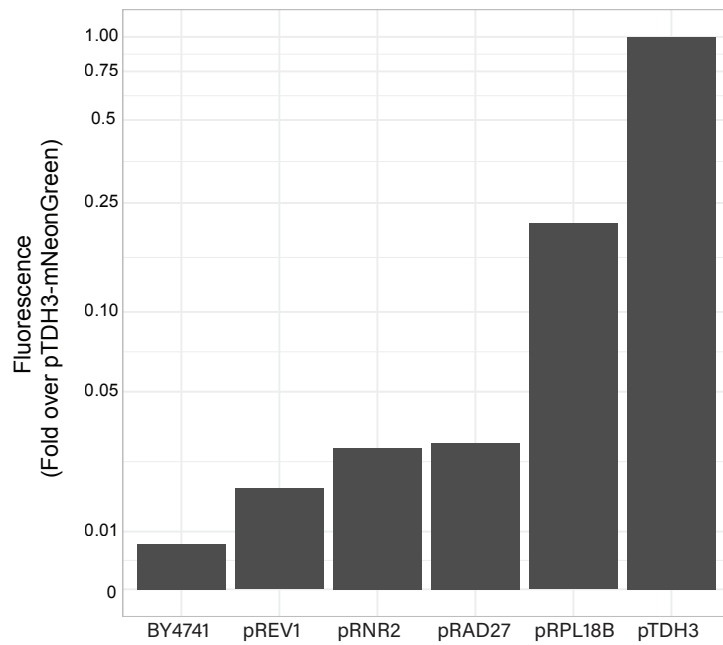


Figure 5.8: Promoter characterization. Fluorescence measurements for the *pTDH3*, *pRPL18B*, *pRAD27*, *pRNR2*, and *pREV1* promoters driving mNeonGreen relative to the expression level of pTDH3-mNeonGreen. BY4741 is the background strain without any fluorescent protein expression.

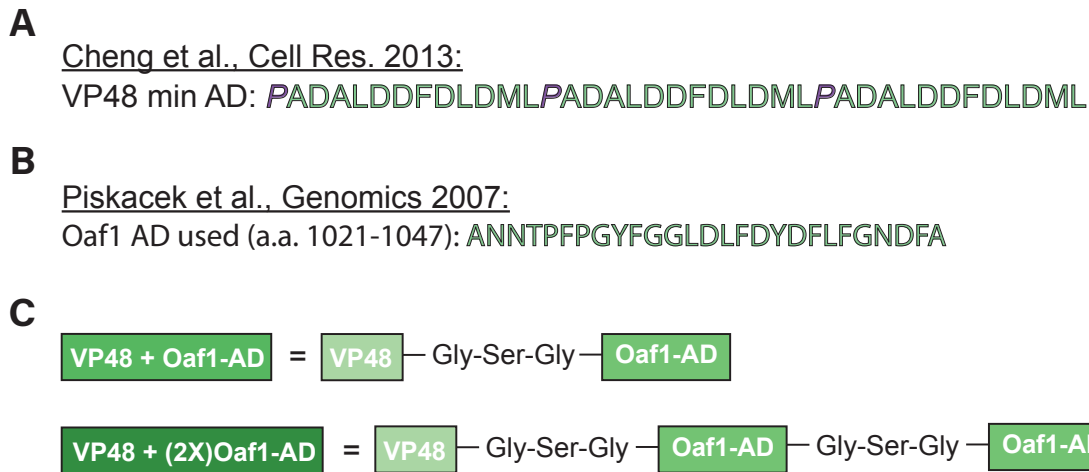


Figure 5.9: Design of activation domains. (A) Sequence of VP48 minimal activation domain protein sequence from Cheng et al. [200]. (B) Core Oaf1 activation domain protein sequence from Piskacek et al. [203]. (C) Design of VP48 minimal AD fused to one or two repeats of the core Oaf1 AD used in this study. Glycine and serine sequences were inserted as linkers.

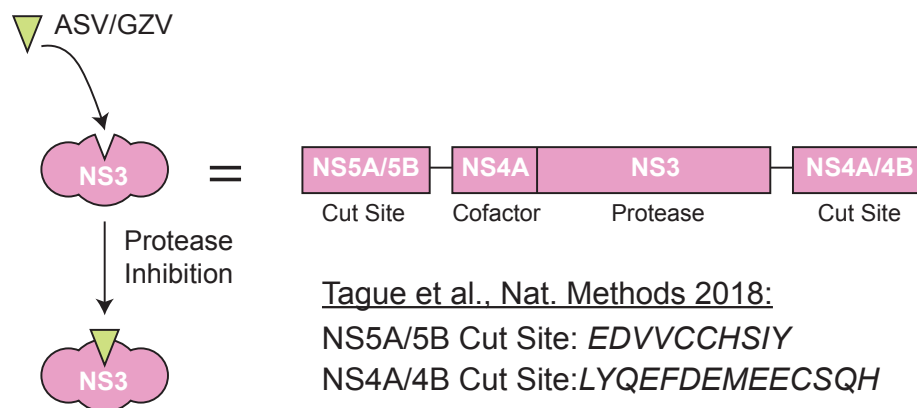


Figure 5.10: Core components of the NS3 protease sequence.

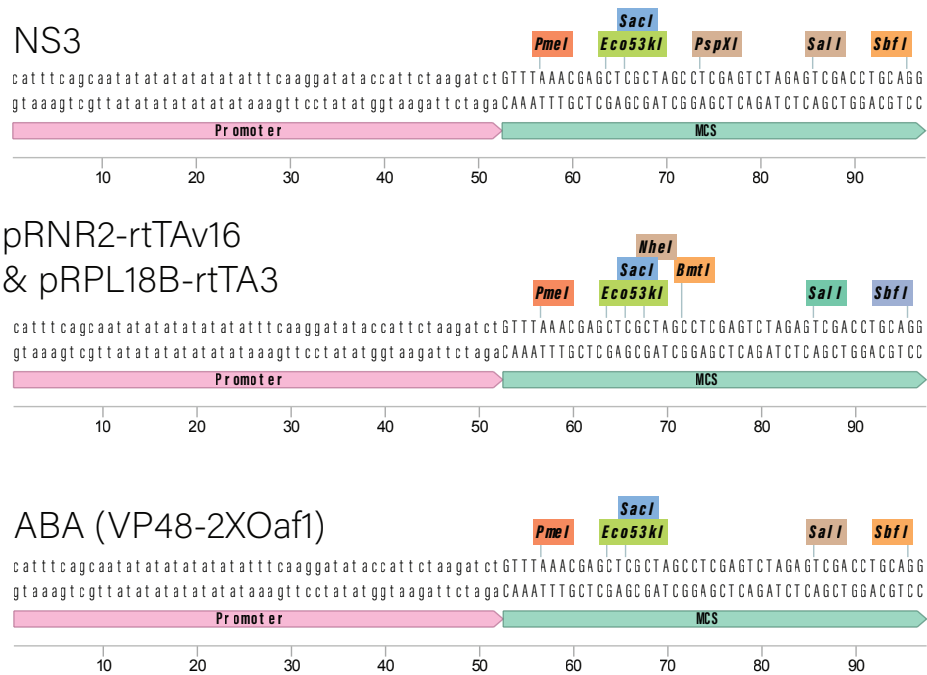


Figure 5.11: Multiple-cloning site (MCS) plasmids. For each of the three kinds of inducible systems, MCS plasmids were constructed. In yTEST we have included MCS plasmids for the NS3 system, pRNR2-rtTA_v16 and pRPL18B-rtTA₃ systems as well as the VP48-2XOaf1 ABA system. The layout of the restriction enzyme cut sequences for inserting genes for inducible control under each of these systems is shown.

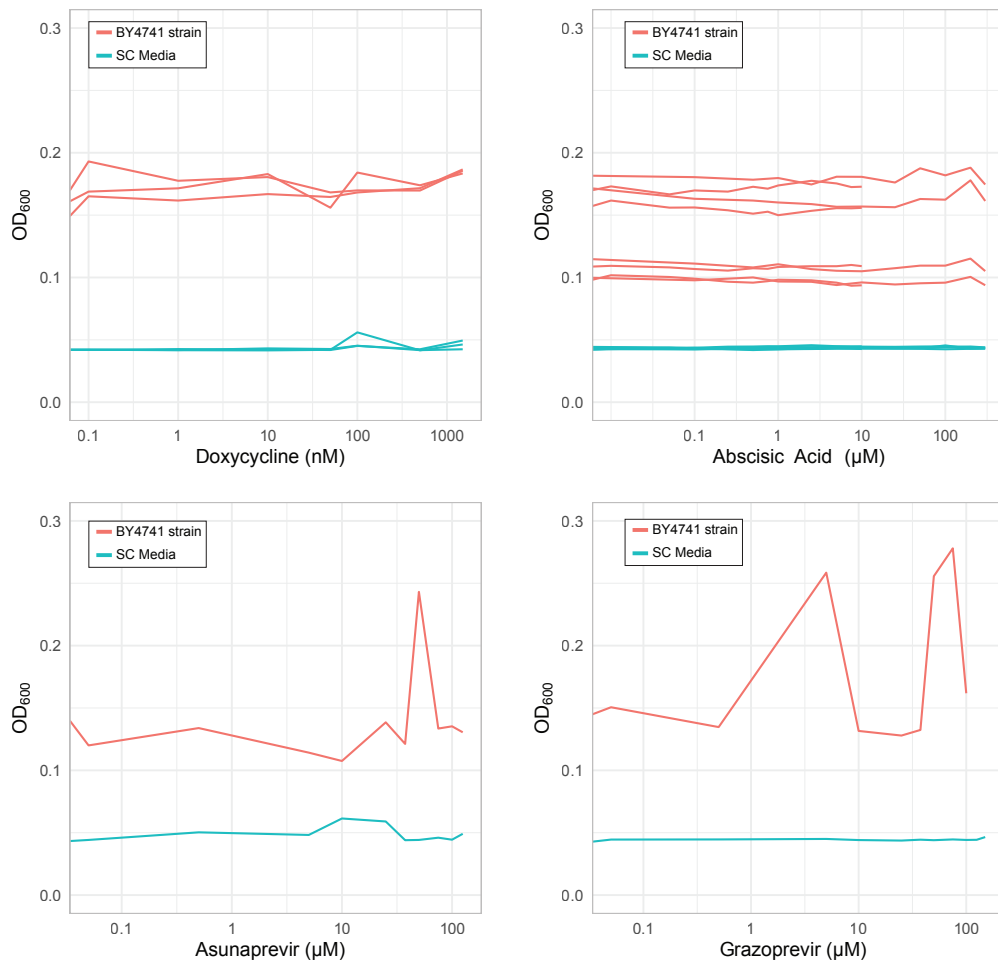


Figure 5.12: Background BY4741 strain growth vs. inducer concentration.

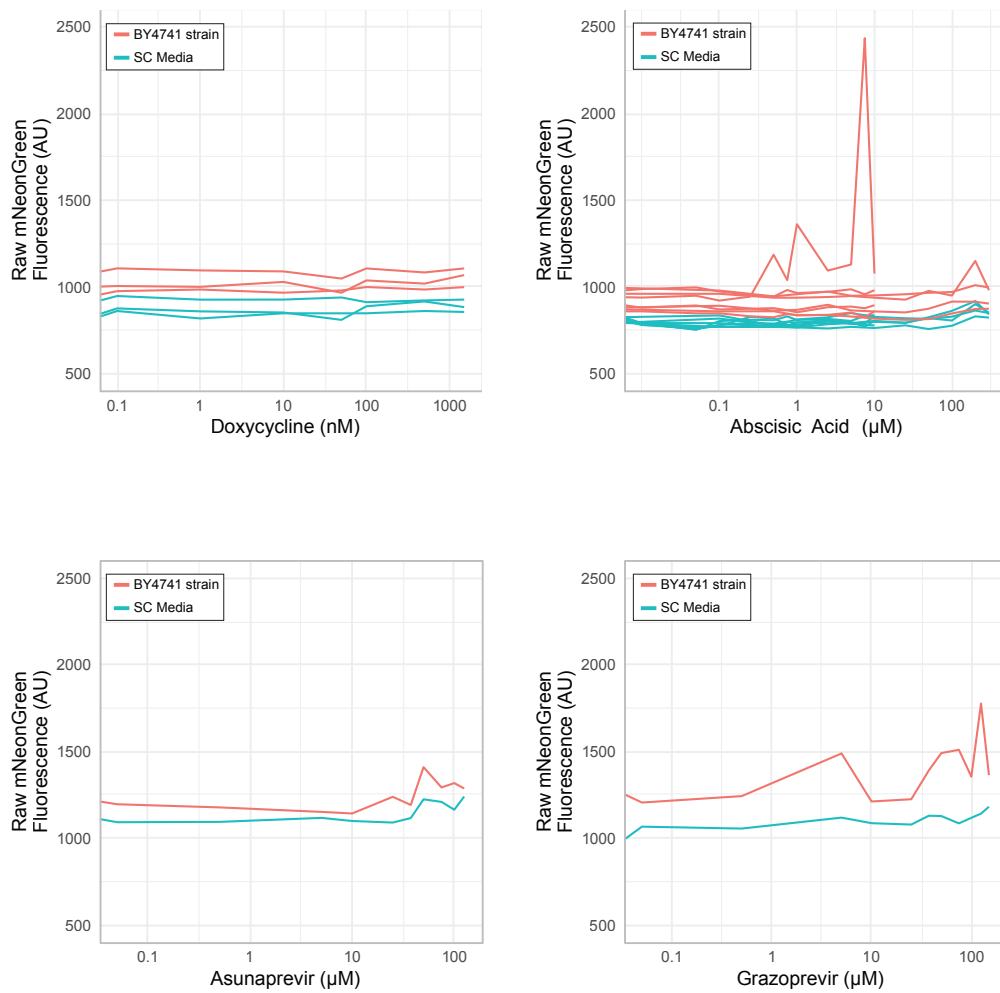


Figure 5.13: Background BY4741 strain growth vs. inducer concentration.

5.6 Methods

5.6.1 Yeast Strains and Transformations

The BY4741 strain (MATa his3 Δ 1 leu2 Δ 0 met15 Δ 0 ura3 Δ 0, from the Nan Hao Lab at UCSD) was used for all experiments. For transforming yeast strains with linearized cassettes we used the “Super-High Efficiency” yeast transformation protocol by William Shaw (<https://benchling.com/protocols/hYSdel7a/yeast-transformation-super-high-efficiency>) with some minor changes made. Briefly, a single BY4741 colony from a YPD agar plate was inoculated liquid YPD media and grown overnight at 30°C. This culture was then diluted 1:50 into 50 mL of YPD the following day and grown at 30°C for 5-6 hours. After this growth period, cells were placed in 50 mL Falcon tubes and spun down in a centrifuge for 10 minutes at 2000 rpm. YPD media was then replaced with 0.1 M lithium acetate (25 mL) and the pellet was resuspended then centrifuged again and then resuspended in 1 mL of fresh 0.1 M lithium acetate (LiOAc). From this 1 mL of cells in LiOAc, we used 100 μ L for individual transformations and this volume was aliquoted into Eppendorf tubes. To begin, 10 μ L of salmon sperm carrier DNA (boiled for 8 minutes at 100°C and then cooled on ice while cells were being centrifuged) was added to each tube of cells at room temperature (RT) and a half hour later 900 μ L of a mixture of 30% PEG-3350 (Sigma-Aldrich), 0.1 M lithium acetate and 10% DMSO was added and mixed with cells by gently pipetting up and down. After resting at RT for a half hour a heat shock at 42°C for 14 minutes was done and then the cells were centrifuged for 2 minutes at 8000 rpm so that the transformation mix could be removed with a pipet. Then, cells were gently mixed with 250 μ L of 5 mM calcium chloride and allowed to incubate at RT for 10 minutes before being plated on synthetic complete (SC) agar plates with the appropriate nutrient selection. After colonies were visible, they were re-streaked onto YPD plates and yeast colony PCR was done to verify which colonies had been properly transformed. For creating -80°C glycerol stocks of correctly transformed colonies, we followed the McClean lab proto-

col ([https://openwetware.org/wiki/McClean:_Glycerol_stocks_\(yeast\)](https://openwetware.org/wiki/McClean:_Glycerol_stocks_(yeast))) and combined 900 μ l of overnight yeast culture with 900 μ l of 30% glycerol.

5.6.2 Golden Gate Assembly Protocol

For Golden Gate cloning we followed the protocol established by Lee et al. 2015 for MoClo-YTK [44]. Generally, we often combined parts at 20 fmol and used vector backbones at 10 fmol for Golden Gate assemblies. For 10 μ L reactions, these components were added to PCR tubes with 0.5 μ L T7 DNA Ligase (New England BioLabs Inc (NEB)), 1 μ L T4 DNA Ligase (NEB), 0.5 μ L BsmBI-v2 or BsaI (2000 U/ μ L) (both from NEB) and filtered dH₂O was added to reach the 10 μ L volume. We used the following thermocycler protocol: digestion for 2 minutes at 42°C for 25 cycles and ligation for 5 minutes at 16°C, followed by a final digestion step for 10 minutes at 60°C and a heat inactivation step for 10 minutes at 80°C.

5.6.3 Construction of Parts and Plasmids.

yTEST parts were designed by sourcing the DNA sequences of needed parts from the literature and/or Addgene and then yeast codon optimizing them using the Integrated DNA Technologies (IDT) codon optimization tool. For each part type the appropriate MoClo-YTK overhangs were added to the sequence. When needed, the sequence of a part was in certain cases changed from the codon optimized version in order to remove restriction sites for BsmBI, BsaI and NotI. These DNA sequences were then ordered as gBlocks from IDT or ordered from Genewiz. Parts were then cloned into the MoClo-YTK entry vector pYTK001 by BsmBI mediated Golden Gate assembly and transformed into DH5 α E. coli, and plated on chloramphenicol LB plates. Colonies on these plates were sequenced (Sanger sequencing) to verify the presence of a correctly formed construct and these plasmids were then used for assembly of inducible systems. For single-gene cassettes parts were assembled by BsaI Golden Gate reactions into the

vector pYTK095, while multigene cassettes were formed from BsmBI Golden Gate reactions using pYTK096, the pre-assembled MoClo-YTK URA3 integration plasmid. DH5 α competent cells were used to transform these constructs and kanamycin or ampicillin selection on LB agar plates was used where appropriate. Colony PCR was used to verify correctly assembled cassettes, which were then grown in LB containing ampicillin or kanamycin and plasmids were minipreped (Qiagen). RE digestion of the plasmids was performed to verify that constructs were of the expected length.

5.6.4 Characterization of Inducible Promoters

For testing strains, colonies were first streaked out on YPD plates and grown at 30°C. A protocol similar to those done by Lee et al.¹² and Shaw et al. [180] was followed. Once colonies were of a large enough size they were added to 500 μ L of SC media in 96-well plates (deep, round-bottom), covered with Breathe-Easier Sealing Film (Diversified Biotech) and grown at 30°C overnight for approximately 18hrs, shaking at 750 RPM on a Scilogex MX-M Microplate Mixer. After this time, cultures were diluted 1:100 in fresh SC media in the same 96-well plates and small-molecule inducers were added at this time. Cells were grown for 6 more hours (at 30°C and 750 RPM) in the presence of each inducer. Doxycycline was diluted in water to 100X the concentration needed in the most concentrated well, then serially diluted and added to each well at 1:100 when doing the dilution. The stock we worked off of was 2 mM doxycycline in water. ABA was diluted in SC with NaOH (for solubility) and then serial dilutions were made in SC+NaOH (so NaOH levels were constant across all levels of inducer) and then added to the plates. The main stock used was 500 μ M ABA in SC with 0.04% v/v 1N NaOH. GZV and ASV master stocks were created by adding DMSO directly to 5mg grazoprevir/asunaprevir to achieve a final concentration of 10mM. This master stock was used to make 100X stocks of GZV/ASV for use in experiments. After the 6-hour induction and growth period, mNeon and OD600 levels were measured. To do this we added 200 μ l of culture from each well and added

it to the well of a black-walled and clear bottom plate (Tecan). In addition, these plates also had wells with a strain expressing pTDH3-mNeonGreen, a BY4741 strain not expressing any fluorescent protein and blank SC media wells containing no yeast cells. These wells were also tested with each concentration of inducer. For wells with BY4741 without a fluorescent protein, mNeon fluorescence values for all inducer concentrations were average together this value was used to subtract a background strain fluorescence from the strains containing inducible systems. OD600 values were processed in the same manner and mNeon fluorescence was divided by the OD600 for each strain. A Tecan Infinite 200 microplate reader was used to perform fluorescence measurements and mNeon fluorescence was measured with an excitation value of 499 nm and emission value at 533 nm.

5.6.5 Analysis of Induction Curves

To analyze induction curves for each inducible system we used the DRC package [212] in R. First, we calculate mean fluorescence and OD for all blank media wells in the run. We then subtracted the mean blank fluorescence and OD from mean background (BY4741 strain) fluorescence and OD. For every other well we then subtracted the mean blank fluorescence from that well's fluorescence, subtracted the mean blank OD from that well's OD, and divided that well's new fluorescence by its new OD. This is normalized fluorescence. Next, we calculate the mean normalized fluorescence for pTDH3-mNeonGreen (yRO163 strain) and divided each measurement by the mean normalized fluorescence for it. We then fit all measurements for each strain, across different concentrations of inducer, to a four-parameter log-logistic model. Finally, we extracted parameters for hill coefficient, half-maximal dose (EC50), maximum expression, and basal expression from the model. For plots where expression was displayed in terms of fold-change over background, we divided each measurement by the normalized fluorescence for the background (BY4741 strain) instead of the normalized fluorescence for pTDH3-mNeonGreen (yRO163 strain). Fold change was calculated by taking the maximal expression level and dividing

it by the basal expression level.

5.6.6 Creation of Inducible System Integration Plasmids with Multiple Cloning Site

To create versions of the NS3, ABA VP48-2XOaf1, pRNR2-rtTAv16 and pRPL18B-rtTA3 multigene, yeast-integration plasmids where the mNeonGreen CDS was replaced with a MCS sequence (GTTTAAACGAGCTCGCTAGCCTCGAGTCTAGAGTCGACCTGCAGG), we PCR-amplified the plasmids with Q5 DNA polymerase (NEB) in a 50uL reaction with the following primers: 5'-TCGAGTCTAGAGTCGACCTGCAGGtaactcgagagtgcctttaactaagaatta-3' and 5'-GGCTAGCGAGCTCGTTTAAACagatcttagaatggatatccttgaatata-3'. Following PCR amplification, Template DNA was removed by adding 1uL DPNI directly to PCR and incubating at 37C for 30 min. The PCR fragments were then run on an agarose gel and extracted. The linear, gel extracted fragments were re-circularized by ligation in a 10uL reaction. 1uL of DNA was mixed with 7uL H₂O, 1uL T4 Ligase Buffer, 0.5uL T4 PNK, and 0.5uL T4 DNA Ligase and incubated at 37C for 30 minutes followed by incubation at room temperature for 2 hours. 5uL of the ligation reaction mix was used to transform 100uL chemically competent DH5alpha E. coli. The MCS-containing plasmids were then verified by Sanger Sequencing. To ensure that the MCS could be used to clone new genes into the inducible systems, we placed the mNeon-Green back into the pRO248-MCS plasmid using the MCS. The pRO248-MCS was digested with the blunt-end restriction enzyme P_{MEI}. 1ug of DNA was digested in a 50uL reaction. To create a linearized mNeonGreen CDS with Gibson-assembly compatible overhangs for assembly with the P_{MEI} digested pRO248-MCS plasmid, mNeonGreen was PCR amplified with Q5 DNA polymerase in a 50uL reaction with the following primers: 5'-taccattctaagatctgtttatgGTTTCAAAGGGGAG-3' and 5'-cgaggctagcgagctcgcttttaGGATCCCTTATAACAATTC-3'. This PCR product was digested with DPNI and gel extracted. The mNeonGreen PCR product and P_{MEI} digested pRO248-MCS plasmid were mixed at a 3:1 molar ratio of insert to vector and assembled in a 10uL

Gibson Assembly reaction mix using Gibson Assembly Master Mix from NEB. The reaction was incubated at 50C for 1 hour prior to transformation into chemically competent DH5alpha by heat shock. The final assembled plasmid was verified by Sanger Sequencing.

5.7 Acknowledgments

This chapter contains material submitted for publication at ACS Synthetic Biology as: O’Laughlin, Ricky*, Tran, Quoc*, Lezia, Andrew*, and Hasty Jeff. “A standardized set of MoClo-compatible inducible promoter systems for tunable gene expression in yeast” (*equal contribution)

Bibliography

- [1] Ron Milo, Shai Shen-Orr, Shalev Itzkovitz, Nadav Kashtan, Dmitri Chklovskii, and Uri Alon. Network motifs: simple building blocks of complex networks. *Science*, 298(5594):824–827, 2002.
- [2] Mingqi Xie and Martin Fussenegger. Designing cell function: assembly of synthetic gene circuits for cell biology applications. *Nature Reviews Molecular Cell Biology*, 19(8):507–525, 2018.
- [3] D Ewen Cameron, Caleb J Bashor, and James J Collins. A brief history of synthetic biology. *Nature Reviews Microbiology*, 12(5):381–390, 2014.
- [4] Martin M Hanczyc. Engineering life: A review of synthetic biology. *Artificial life*, 26(2):260–273, 2020.
- [5] Michael B Elowitz and Stanislas Leibler. A synthetic oscillatory network of transcriptional regulators. *Nature*, 403(6767):335–338, 2000.
- [6] Timothy S Gardner, Charles R Cantor, and James J Collins. Construction of a genetic toggle switch in escherichia coli. *Nature*, 403(6767):339–342, 2000.
- [7] Tasuku Kitada, Breanna DiAndreth, Brian Teague, and Ron Weiss. Programming gene and engineered-cell therapies with synthetic biology. *Science*, 359(6376), 2018.
- [8] Edward F McCarthy. The toxins of william b. coley and the treatment of bone and soft-tissue sarcomas. *The Iowa orthopaedic journal*, 26:154, 2006.
- [9] Shibin Zhou, Claudia Gravekamp, David Bermudes, and Ke Liu. Tumour-targeting bacteria engineered to fight cancer. *Nature Reviews Cancer*, 18(12):727–743, 2018.
- [10] Cecilia A Silva-Valenzuela, Prerak T Desai, Roberto C Molina-Quiroz, David Pezoa, Yong Zhang, Steffen Porwollik, Ming Zhao, Robert M Hoffman, Inés Contreras, Carlos A Santiviago, et al. Solid tumors provide niche-specific conditions that lead to preferential growth of salmonella. *Oncotarget*, 7(23):35169, 2016.

- [11] Mai Thi-Quynh Duong, Yeshan Qin, Sung-Hwan You, and Jung-Joon Min. Bacteria-cancer interactions: bacteria-based cancer therapy. *Experimental & molecular medicine*, 51(12):1–15, 2019.
- [12] Tal Danino, Justin Lo, Arthur Prindle, Jeff Hasty, and Sangeeta N Bhatia. In vivo gene expression dynamics of tumor-targeted bacteria. *ACS synthetic biology*, 1(10):465–470, 2012.
- [13] M Omar Din, Tal Danino, Arthur Prindle, Matt Skalak, Jangir Selimkhanov, Kaitlin Allen, Ellixis Julio, Eta Atolia, Lev S Tsimring, Sangeeta N Bhatia, et al. Synchronized cycles of bacterial lysis for in vivo delivery. *Nature*, 536(7614):81–85, 2016.
- [14] Sreyan Chowdhury, Samuel Castro, Courtney Coker, Taylor E Hinchliffe, Nicholas Arpaia, and Tal Danino. Programmable bacteria induce durable tumor regression and systemic antitumor immunity. *Nature medicine*, 25(7):1057–1063, 2019.
- [15] Candice R Gurbatri, Ioana Lia, Rosa Vincent, Courtney Coker, Samuel Castro, Piper M Treuting, Taylor E Hinchliffe, Nicholas Arpaia, and Tal Danino. Engineered probiotics for local tumor delivery of checkpoint blockade nanobodies. *Science translational medicine*, 12(530), 2020.
- [16] Michael J Liao, M Omar Din, Lev Tsimring, and Jeff Hasty. Rock-paper-scissors: Engineered population dynamics increase genetic stability. *Science*, 365(6457):1045–1049, 2019.
- [17] Arianna Miano, Michael J Liao, and Jeff Hasty. Inducible cell-to-cell signaling for tunable dynamics in microbial communities. *Nature communications*, 11(1):1–8, 2020.
- [18] Fahriye Duzagac, Gloria Saorin, Lorenzo Memeo, Vincenzo Canzonieri, and Flavio Rizzolio. Microfluidic organoids-on-a-chip: Quantum leap in cancer research. *Cancers*, 13(4):737, 2021.
- [19] Garrett Graham, Nicholas Csicsery, Elizabeth Stasiowski, Gregoire Thouvenin, William H Mather, Michael Ferry, Scott Cookson, and Jeff Hasty. Genome-scale transcriptional dynamics and environmental biosensing. *Proceedings of the National Academy of Sciences*, 117(6):3301–3306, 2020.
- [20] Scott Cookson, Natalie Ostroff, Wyming Lee Pang, Dmitri Volfson, and Jeff Hasty. Monitoring dynamics of single-cell gene expression over multiple cell cycles. *Molecular Systems Biology*, 1(1):2005–0024, 2005.
- [21] Jesse Stricker, Scott Cookson, Matthew R Bennett, William H Mather, Lev S Tsimring, and Jeff Hasty. A fast, robust and tunable synthetic gene oscillator. *Nature*, 456(7221):516–519, 2008.
- [22] Matthew R Bennett and Jeff Hasty. Microfluidic devices for measuring gene network dynamics in single cells. *Nature Reviews Genetics*, 10(9):628–638, 2009.

- [23] Mike S Ferry, Ivan A Razinkov, and Jeff Hasty. Microfluidics for synthetic biology: from design to execution. In *Methods in enzymology*, volume 497, pages 295–372. Elsevier, 2011.
- [24] Martin Kolnik, Lev S Tsimring, and Jeff Hasty. Vacuum-assisted cell loading enables shear-free mammalian microfluidic culture. *Lab on a chip*, 12(22):4732–4737, 2012.
- [25] Arthur Prindle, Phillip Samayoa, Ivan Razinkov, Tal Danino, Lev S Tsimring, and Jeff Hasty. A sensing array of radically coupled genetic ‘biopixels’. *Nature*, 481(7379):39–44, 2012.
- [26] Yang Li, Meng Jin, Richard O’Laughlin, Philip Bittihn, Lev S Tsimring, Lorraine Pillus, Jeff Hasty, and Nan Hao. Multigenerational silencing dynamics control cell aging. *Proceedings of the National Academy of Sciences*, 114(42):11253–11258, 2017.
- [27] Hao Song, Stephen Payne, Cheemeng Tan, and Lingchong You. Programming microbial population dynamics by engineered cell–cell communication. *Biotechnology journal*, 6(7):837–849, 2011.
- [28] Philip Bittihn, M Omar Din, Lev S Tsimring, and Jeff Hasty. Rational engineering of synthetic microbial systems: from single cells to consortia. *Current opinion in microbiology*, 45:92–99, 2018.
- [29] Ye Chen, Jae Kyoung Kim, Andrew J Hirning, Krešimir Josić, and Matthew R Bennett. Emergent genetic oscillations in a synthetic microbial consortium. *Science*, 349(6251):986–989, 2015.
- [30] Nicolas E Grandel, Kiara Reyes Gamas, and Matthew R Bennett. Control of synthetic microbial consortia in time, space, and composition. *Trends in Microbiology*, 2021.
- [31] Francesca Ceroni, Rhys Algar, Guy-Bart Stan, and Tom Ellis. Quantifying cellular capacity identifies gene expression designs with reduced burden. *Nature methods*, 12(5):415–418, 2015.
- [32] Francesca Ceroni, Alice Boo, Simone Furini, Thomas E Goroehowski, Olivier Borkowski, Yaseen N Ladak, Ali R Awan, Charlie Gilbert, Guy-Bart Stan, and Tom Ellis. Burden-driven feedback control of gene expression. *Nature methods*, 15(5):387–393, 2018.
- [33] Shalni Kumar and Jeff Hasty. Stability, robustness, and containment: preparing synthetic biology for real-world deployment. *Current Opinion in Biotechnology*, 79:102880, 2023.
- [34] Michael B Elowitz, Arnold J Levine, Eric D Siggia, and Peter S Swain. Stochastic gene expression in a single cell. *Science*, 297(5584):1183–1186, 2002.
- [35] Lucia Bandiera, Simone Furini, and Emanuele Giordano. Phenotypic variability in synthetic biology applications: dealing with noise in microbial gene expression. *Frontiers in Microbiology*, 7:479, 2016.

- [36] Eric L Haseltine and Frances H Arnold. Synthetic gene circuits: design with directed evolution. *Annu. Rev. Biophys. Biomol. Struct.*, 36:1–19, 2007.
- [37] Andrew Currin, Steven Parker, Christopher J Robinson, Eriko Takano, Nigel S Scrutton, and Rainer Breitling. The evolving art of creating genetic diversity: From directed evolution to synthetic biology. *Biotechnology Advances*, 50:107762, 2021.
- [38] Daniel G Gibson, Lei Young, Ray-Yuan Chuang, J Craig Venter, Clyde A Hutchison, and Hamilton O Smith. Enzymatic assembly of dna molecules up to several hundred kilobases. *Nature methods*, 6(5):343–345, 2009.
- [39] Stefan Werner, Carola Engler, Ernst Weber, Ramona Gruetzner, and Sylvestre Marillonnet. Fast track assembly of multigene constructs using golden gate cloning and the moclo system. *Bioengineered*, 3(1):38–43, 2012.
- [40] Carola Engler, Ramona Gruetzner, Romy Kandzia, and Sylvestre Marillonnet. Golden gate shuffling: a one-pot dna shuffling method based on type iis restriction enzymes. *PloS one*, 4(5):e5553, 2009.
- [41] Simon J Moore, Hung-En Lai, Richard JR Kelwick, Soo Mei Chee, David J Bell, Karen Marie Polizzi, and Paul S Freemont. Ecoflex: a multifunctional moclo kit for e. coli synthetic biology. *ACS Synthetic Biology*, 5(10):1059–1069, 2016.
- [42] Ravendran Vasudevan, Grant AR Gale, Alejandra A Schiavon, Anton Puzorjov, John Malin, Michael D Gillespie, Konstantinos Vavitsas, Valentin Zulkower, Baojun Wang, Christopher J Howe, et al. Cyanogate: A modular cloning suite for engineering cyanobacteria based on the plant moclo syntax. *Plant Physiology*, 180(1):39–55, 2019.
- [43] Sonya V Iverson, Traci L Haddock, Jacob Beal, and Douglas M Densmore. Cidar moclo: improved moclo assembly standard and new e. coli part library enable rapid combinatorial design for synthetic and traditional biology. *ACS synthetic biology*, 5(1):99–103, 2016.
- [44] M. E. Lee, W. C. DeLoache, B. Cervantes, and J. E. Dueber. A highly characterized yeast toolkit for modular, multipart assembly. *ACS Synth Biol*, 4(9):975–986, 2015.
- [45] W.M. Shaw, H. Yamauchi, J. Mead, G.F. Gowers, D.J. Bell, D. Oling, N. Larsson, M. Wigglesworth, G. Ladds, and T. Ellis. Engineering a model cell for rational tuning of gpcr signaling. *Cell*, 177(3):782–796.e727, 2019.
- [46] Carola Engler, Mark Youles, Ramona Gruetzner, Tim-Martin Ehnert, Stefan Werner, Jonathan DG Jones, Nicola J Patron, and Sylvestre Marillonnet. A golden gate modular cloning toolbox for plants. *ACS synthetic biology*, 3(11):839–843, 2014.
- [47] Alessandro Occhialini, Agnieszka A Piatek, Alexander C Pfothenhauer, Taylor P Frazier, C Neal Stewart Jr, and Scott C Lenaghan. Mochlo: a versatile, modular cloning toolbox for chloroplast biotechnology. *Plant physiology*, 179(3):943–957, 2019.

- [48] João Pedro Fonseca, Alain R Bonny, G Renuka Kumar, Andrew H Ng, Jason Town, Qiu Chang Wu, Elham Aslankoochi, Susan Y Chen, Galen Dods, Patrick Harrigan, et al. A toolkit for rapid modular construction of biological circuits in mammalian cells. *ACS synthetic biology*, 8(11):2593–2606, 2019.
- [49] Eric L Haseltine and Frances H Arnold. Synthetic gene circuits: design with directed evolution. *Annu. Rev. Biophys. Biomol. Struct.*, 36:1–19, 2007.
- [50] Alec AK Nielsen, Bryan S Der, Jonghyeon Shin, Prashant Vaidyanathan, Vanya Paralanov, Elizabeth A Strychalski, David Ross, Douglas Densmore, and Christopher A Voigt. Genetic circuit design automation. *Science*, 352(6281), 2016.
- [51] Domitilla Del Vecchio. Modularity, context-dependence, and insulation in engineered biological circuits. *Trends in biotechnology*, 33(2):111–119, 2015.
- [52] Eleni Karamasioti, Claude Lormeau, and Jörg Stelling. Computational design of biological circuits: putting parts into context. *Molecular Systems Design & Engineering*, 2(4):410–421, 2017.
- [53] Yohei Yokobayashi, Ron Weiss, and Frances H Arnold. Directed evolution of a genetic circuit. *Proceedings of the National Academy of Sciences*, 99(26):16587–16591, 2002.
- [54] Jeff Hasty. Design then mutate. *Proceedings of the National Academy of Sciences*, 99(26):16516–16518, 2002.
- [55] Huanting Liu and James H Naismith. An efficient one-step site-directed deletion, insertion, single and multiple-site plasmid mutagenesis protocol. *BMC biotechnology*, 8(1):1–10, 2008.
- [56] Ryan R Gallagher, Zhe Li, Aaron O Lewis, and Farren J Isaacs. Rapid editing and evolution of bacterial genomes using libraries of synthetic dna. *nature protocols*, 9(10):2301–2316, 2014.
- [57] Fanli Zeng, Suhua Zhang, Zhimin Hao, Shixin Duan, Yanan Meng, Pan Li, Jingao Dong, and Yibin Lin. Efficient strategy for introducing large and multiple changes in plasmid dna. *Scientific reports*, 8(1):1–12, 2018.
- [58] Shakked O Halperin, Connor J Tou, Eric B Wong, Cyrus Modavi, David V Schaffer, and John E Dueber. Crispr-guided dna polymerases enable diversification of all nucleotides in a tunable window. *Nature*, 560(7717):248–252, 2018.
- [59] Kevin M Esvelt, Jacob C Carlson, and David R Liu. A system for the continuous directed evolution of biomolecules. *Nature*, 472(7344):499–503, 2011.
- [60] David L Alexander, Joshua Lilly, Jaime Hernandez, Jillian Romsdahl, Christopher J Troll, and Manel Camps. Random mutagenesis by error-prone pol plasmid replication in escherichia coli. In *Directed Evolution Library Creation*, pages 31–44. Springer, 2014.

- [61] Ernst Weber, Carola Engler, Ramona Gruetzner, Stefan Werner, and Sylvestre Marillonnet. A modular cloning system for standardized assembly of multigene constructs. *PLoS one*, 6(2):e16765, 2011.
- [62] Pankaj C Jain and Raghavan Varadarajan. A rapid, efficient, and economical inverse polymerase chain reaction-based method for generating a site saturation mutant library. *Analytical biochemistry*, 449:90–98, 2014.
- [63] Yolanda Schaerli and Mark Isalan. Building synthetic gene circuits from combinatorial libraries: screening and selection strategies. *Molecular BioSystems*, 9(7):1559–1567, 2013.
- [64] George Emanuel, Jeffrey R Moffitt, and Xiaowei Zhuang. High-throughput, image-based screening of pooled genetic-variant libraries. *Nature methods*, 14(12):1159–1162, 2017.
- [65] Michael J Lawson, Daniel Camsund, Jimmy Larsson, Özden Baltekin, David Fange, and Johan Elf. In situ genotyping of a pooled strain library after characterizing complex phenotypes. *Molecular systems biology*, 13(10):947, 2017.
- [66] Daniel Camsund, Michael J Lawson, Jimmy Larsson, Daniel Jones, Spartak Zikrin, David Fange, and Johan Elf. Time-resolved imaging-based crispr screening. *Nature methods*, 17(1):86–92, 2020.
- [67] Scott Luro, Laurent Potvin-Trottier, Burak Okumus, and Johan Paulsson. Isolating live cells after high-throughput, long-term, time-lapse microscopy. *Nature methods*, 17(1):93–100, 2020.
- [68] Alan T Bull. The renaissance of continuous culture in the post-genomics age. *Journal of Industrial Microbiology and Biotechnology*, 37(10):993–1021, 2010.
- [69] Ming-Ru Wu, Barbara Jusiak, and Timothy K Lu. Engineering advanced cancer therapies with synthetic biology. *Nature Reviews Cancer*, 19(4):187–195, 2019.
- [70] Gregory D Sepich-Poore, Laurence Zitvogel, Ravid Straussman, Jeff Hasty, Jennifer A Wargo, and Rob Knight. The microbiome and human cancer. *Science*, 371(6536), 2021.
- [71] Spencer R Scott, M Omar Din, Philip Bittihn, Liyang Xiong, Lev S Tsimring, and Jeff Hasty. A stabilized microbial ecosystem of self-limiting bacteria using synthetic quorum-regulated lysis. *Nature microbiology*, 2(8):1–9, 2017.
- [72] Amin Espah Borujeni, Anirudh S Channarasappa, and Howard M Salis. Translation rate is controlled by coupled trade-offs between site accessibility, selective rna unfolding and sliding at upstream standby sites. *Nucleic acids research*, 42(4):2646–2659, 2014.
- [73] Alexander C Reis and Howard M Salis. An automated model test system for systematic development and improvement of gene expression models. *ACS Synthetic Biology*, 9(11):3145–3156, 2020.

- [74] Howard M Salis, Ethan A Mirsky, and Christopher A Voigt. Automated design of synthetic ribosome binding sites to control protein expression. *Nature biotechnology*, 27(10):946–950, 2009.
- [75] Michael G Napolitano, Matthieu Landon, Christopher J Gregg, Marc J Lajoie, Lakshmi Govindarajan, Joshua A Mosberg, Gleb Kuznetsov, Daniel B Goodman, Oscar Vargas-Rodriguez, Farren J Isaacs, et al. Emergent rules for codon choice elucidated by editing rare arginine codons in escherichia coli. *Proceedings of the National Academy of Sciences*, 113(38):E5588–E5597, 2016.
- [76] Thomas G Bernhardt, William D Roof, and Ry Young. Genetic evidence that the bacteriophage ϕ x174 lysis protein inhibits cell wall synthesis. *Proceedings of the National Academy of Sciences*, 97(8):4297–4302, 2000.
- [77] Leo Baumgart, William Mather, and Jeff Hasty. Synchronized dna cycling across a bacterial population. *Nature genetics*, 49(8):1282–1285, 2017.
- [78] Tal Danino, Octavio Mondragón-Palomino, Lev Tsimring, and Jeff Hasty. A synchronized quorum of genetic clocks. *Nature*, 463(7279):326–330, 2010.
- [79] Peter Orth, Dirk Schnappinger, Wolfgang Hillen, Wolfram Saenger, and Winfried Hinrichs. Structural basis of gene regulation by the tetracycline inducible tet repressor–operator system. *Nature structural biology*, 7(3):215–219, 2000.
- [80] Danielis Rutkauskas, Hongli Zhan, Kathleen S Matthews, Francesco S Pavone, and Francesco Vanzi. Tetramer opening in lacI-mediated dna looping. *Proceedings of the National Academy of Sciences*, 106(39):16627–16632, 2009.
- [81] David Lepzelter, Haidong Feng, and Jin Wang. Oscillation, cooperativity, and intermediates in the self-repressing gene. *Chemical physics letters*, 490(4-6):216–220, 2010.
- [82] James E Ferrell Jr and Sang Hoon Ha. Ultrasensitivity part iii: cascades, bistable switches, and oscillators. *Trends in biochemical sciences*, 39(12):612–618, 2014.
- [83] JChristopher Anderson, John E Dueber, Mariana Leguia, Gabriel C Wu, Jonathan A Goler, Adam P Arkin, and Jay D Keasling. Bglbricks: A flexible standard for biological part assembly. *Journal of biological engineering*, 4(1):1–12, 2010.
- [84] Guillermo Rodrigo, Thomas E Landrain, and Alfonso Jaramillo. De novo automated design of small rna circuits for engineering synthetic riboregulation in living cells. *Proceedings of the National Academy of Sciences*, 109(38):15271–15276, 2012.
- [85] Stephanie J Doong, Apoorv Gupta, and Kristala LJ Prather. Layered dynamic regulation for improving metabolic pathway productivity in escherichia coli. *Proceedings of the National Academy of Sciences*, 115(12):2964–2969, 2018.

- [86] Stephanie K Aoki, Gabriele Lillacci, Ankit Gupta, Armin Baumschlager, David Schwein-gruber, and Mustafa Khammash. A universal biomolecular integral feedback controller for robust perfect adaptation. *Nature*, 570(7762):533–537, 2019.
- [87] Arturo Urrios, Eva Gonzalez-Flo, David Canadell, Eulalia de Nadal, Javier Macia, and Francesc Posas. Plug-and-play multicellular circuits with time-dependent dynamic re-sponses. *ACS synthetic biology*, 7(4):1095–1104, 2018.
- [88] Felix Moser, Amin Espah Borujeni, Amar N Ghodasara, Ewen Cameron, Yongjin Park, and Christopher A Voigt. Dynamic control of endogenous metabolism with combinatorial logic circuits. *Molecular systems biology*, 14(11):e8605, 2018.
- [89] Matthew Scott, Carl W Gunderson, Eduard M Mateescu, Zhongge Zhang, and Terence Hwa. Interdependence of cell growth and gene expression: origins and consequences. *Science*, 330(6007):1099–1102, 2010.
- [90] Mehmet U Caglar, John R Houser, Craig S Barnhart, Daniel R Boutz, Sean M Carroll, Aurko Dasgupta, Walter F Lenoir, Bartram L Smith, Viswanadham Sridhara, Dariya K Sydykova, et al. The e. coli molecular phenotype under different growth conditions. *Scientific reports*, 7(1):1–15, 2017.
- [91] Chris N Takahashi, Aaron W Miller, Felix Ekness, Maitreya J Dunham, and Eric Klavins. A low cost, customizable turbidostat for use in synthetic circuit characterization. *ACS synthetic biology*, 4(1):32–38, 2015.
- [92] Boyang Zhang, Anastasia Korolj, Benjamin Fook Lun Lai, and Milica Radisic. Advances in organ-on-a-chip engineering. *Nature Reviews Materials*, 3(8):257–278, 2018.
- [93] Roberto Rusconi, Melissa Garren, and Roman Stocker. Microfluidics expanding the frontiers of microbial ecology. *Annual review of biophysics*, 43:65–91, 2014.
- [94] M. S. Ferry, I. A. Razinkov, and J. Hasty. Chapter fourteen - Microfluidics for Synthetic Biology: From Design to Execution. In Chris Voigt, editor, *Synthetic Biology, Part A*, volume 497 of *Methods in Enzymology*, pages 295–372. Academic Press, 2011. ISSN: 0076-6879.
- [95] Gregory D Poore, Evguenia Kopylova, Qiyun Zhu, Carolina Carpenter, Serena Fraraccio, Stephen Wandro, Tomasz Kosciolk, Stefan Janssen, Jessica Metcalf, Se Jin Song, et al. Microbiome analyses of blood and tissues suggest cancer diagnostic approach. *Nature*, 579(7800):567–574, 2020.
- [96] Jan Claesen and Michael A Fischbach. Synthetic microbes as drug delivery systems. *ACS synthetic biology*, 4(4):358–364, 2015.
- [97] Gabriele RM Kleiner-Grote, Joe M Risse, and Karl Friebs. Secretion of recombinant proteins from e. coli. *Engineering in Life Sciences*, 18(8):532–550, 2018.

- [98] Tetsuhiro Harimoto, Zakary S Singer, Oscar S Velazquez, Joanna Zhang, Samuel Castro, Taylor E Hinchliffe, William Mather, and Tal Danino. Rapid screening of engineered microbial therapies in a 3d multicellular model. *Proceedings of the National Academy of Sciences*, 116(18):9002–9007, 2019.
- [99] Marta Kapalczynska, Tomasz Kolenda, Weronika Przybyla, Maria Zajkaczowska, Anna Teresiak, Violetta Filas, Matthew Ibbs, Renata Bli'zniak, Lukasz Luczewski, and Katarzyna Lamperska. 2d and 3d cell cultures—a comparison of different types of cancer cell cultures. *Archives of Medical Science*, 14(4):910–919, 2018.
- [100] JungHo Ahn, Yoshitaka J Sei, Noo Li Jeon, and YongTae Kim. Tumor microenvironment on a chip: the progress and future perspective. *Bioengineering*, 4(3):64, 2017.
- [101] Laura C McCaughey, Inokentij's Josts, Rhys Grinter, Paul White, Olwyn Byron, Nicholas P Tucker, Jacqueline M Matthews, Colin Kleanthous, Cynthia B Whitchurch, and Daniel Walker. Discovery, characterization and in vivo activity of pyocin sd2, a protein antibiotic from pseudomonas aeruginosa. *Biochemical Journal*, 473(15):2345–2358, 2016.
- [102] Bryan J Berube and Juliane Bubeck Wardenburg. Staphylococcus aureus α -toxin: nearly a century of intrigue. *Toxins*, 5(6):1140–1166, 2013.
- [103] Fatemeh Shafiee, Marc G Aucoin, and Ali Jahanian-Najafabadi. Targeted diphtheria toxin-based therapy: a review article. *Frontiers in microbiology*, 10:2340, 2019.
- [104] Haniyeh Abuei, Abbas Behzad-Behbahani, Fatemeh Faghihi, Ali Farhadi, Gholam Reza Rafiei Dehbidi, Mohammad Pirouzfard, and Farahnaz Zare. The effect of bacterial peptide p28 on viability and apoptosis status of p53-null hela cells. *Advanced Pharmaceutical Bulletin*, 9(4):668, 2019.
- [105] ROBERT H Hall and BS Drasar. Vibrio cholerae hlyA hemolysin is processed by proteolysis. *Infection and immunity*, 58(10):3375–3379, 1990.
- [106] Marta Michalska and Philipp Wolf. Pseudomonas exotoxin a: optimized by evolution for effective killing. *Frontiers in microbiology*, 6:963, 2015.
- [107] H Smith and J Keppie. Observations on experimental anthrax: demonstration of a specific lethal factor produced in vivo by bacillus anthracis. *Nature*, 173(4410):869–870, 1954.
- [108] David Šmajš, Lenka Micenková, Jan Šmarda, Martin Vrba, Alena Ševčíková, Zuzana Vališová, and Vladana Woznicová. Bacteriocin synthesis in uropathogenic and commensal escherichia coli: colicin e1 is a potential virulence factor. *BMC microbiology*, 10(1):1–10, 2010.
- [109] Lucie Dardevet, Dipti Rani, Tarek Abd El Aziz, Ingrid Bazin, Jean-Marc Sabatier, Mahmoud Fadl, Elisabeth Brambilla, and Michel De Waard. Chlorotoxin: a helpful natural scorpion peptide to diagnose glioma and fight tumor invasion. *Toxins*, 7(4):1079–1101, 2015.

- [110] Fiorenzo Stirpe, Sjur Olsnes, and Alexander Pihl. Gelonin, a new inhibitor of protein synthesis, nontoxic to intact cells. isolation, characterization, and preparation of cytotoxic complexes with concanavalin a. *Journal of Biological Chemistry*, 255(14):6947–6953, 1980.
- [111] Neil R Wyborn, Angela Clark, Ruth E Roberts, Stuart J Jamieson, Svetomir Tzokov, Per A Bullough, Timothy J Stillman, Peter J Artymiuk, James E Galen, Licheng Zhao, et al. Properties of haemolysin e (hlye) from a pathogenic escherichia coli avian isolate and studies of hlye export. *Microbiology*, 150(5):1495–1505, 2004.
- [112] Nicolas Puillandre and Mandë Holford. The terebridae and teretoxins: Combining phylogeny and anatomy for concerted discovery of bioactive compounds. *BMC Chemical Biology*, 10:1–12, 2010.
- [113] Maria P Ikonomopoulou, Manuel A Fernandez-Rojo, Sandy S Pineda, Pablo Cabezas-Sainz, Brit Winnen, Rodrigo AV Morales, Andreas Brust, Laura Sánchez, Paul F Alewood, Grant A Ramm, et al. Gomesin inhibits melanoma growth by manipulating key signaling cascades that control cell death and proliferation. *Scientific reports*, 8(1):1–14, 2018.
- [114] Yifan Han, Zhibin Cui, Yen-Hsing Li, Wei-Hsuan Hsu, and Bao-Hong Lee. In vitro and in vivo anticancer activity of pardaxin against proliferation and growth of oral squamous cell carcinoma. *Marine Drugs*, 14(1):2, 2015.
- [115] Ciara Duffy, Anabel Sorolla, Edina Wang, Emily Golden, Eleanor Woodward, Kathleen Davern, Diwei Ho, Elizabeth Johnstone, Kevin Pflieger, Andrew Redfern, et al. Honeybee venom and melittin suppress growth factor receptor activation in her2-enriched and triple-negative breast cancer. *NPJ precision oncology*, 4(1):24, 2020.
- [116] Stewart A Thompson, Kazuo Tachibana, Koji Nakanishi, and Ichiro Kubota. Melittin-like peptides from the shark-repelling defense secretion of the sole pardachirus pavoninus. *Science*, 233(4761):341–343, 1986.
- [117] Michelle C Callegan, Bradley D Jett, Lynn E Hancock, and Michael S Gilmore. Role of hemolysin bl in the pathogenesis of extraintestinal bacillus cereus infection assessed in an endophthalmitis model. *Infection and immunity*, 67(7):3357–3366, 1999.
- [118] Huiqiong Xie, Miao Huang, Qiping Hu, Kejian Sun, Huayu Wu, Wei Shu, Xiaolong Li, and Ling Fang. Agkihpin, a novel svtle from gloydius halys pallas, promotes platelet aggregation in vitro and inhibits thrombus formation in vivo in murine models of thrombosis. *Toxicon*, 122:78–88, 2016.
- [119] Marcela Manrique-Moreno, Gloria A Santa-González, and Vanessa Gallego. Bioactive cationic peptides as potential agents for breast cancer treatment. *Bioscience reports*, 41(12):BSR20211218C, 2021.

- [120] Xin Pan, Yu-Qin Zhao, Fa-Yuan Hu, Chang-Feng Chi, and Bin Wang. Anticancer activity of a hexapeptide from skate (*raja porosa*) cartilage protein hydrolysate in hela cells. *Marine Drugs*, 14(8):153, 2016.
- [121] Elda E Sánchez, Alexis Rodríguez-Acosta, Rene Palomar, Sara E Lucena, Sajid Bashir, Julio G Soto, and John C Pérez. Colombistatin: a disintegrin isolated from the venom of the south american snake (*bothrops colombiensis*) that effectively inhibits platelet aggregation and sk-mel-28 cell adhesion. *Archives of toxicology*, 83:271–279, 2009.
- [122] LP Billen, A Shamas-Din, and DW Andrews. Bid: a bax-like bh3 protein. *Oncogene*, 27(1):S93–S104, 2008.
- [123] Annette Fagerlund, Toril Lindbäck, Anne K Storset, Per Einar Granum, and Simon P Hardy. *Bacillus cereus* nhe is a pore-forming toxin with structural and functional properties similar to the clyA (hlyE, sheA) family of haemolysins, able to induce osmotic lysis in epithelia. *Microbiology*, 154(3):693–704, 2008.
- [124] Venkatesh S Shirure, Ye Bi, Matthew B Curtis, Andrew Lezia, Madeleine M Goedegebuure, S Peter Goedegebuure, Rebecca Aft, Ryan C Fields, and Steven C George. Tumor-on-a-chip platform to investigate progression and drug sensitivity in cell lines and patient-derived organoids. *Lab on a Chip*, 18(23):3687–3702, 2018.
- [125] Monika Kijanska and Jens Kelm. In vitro 3d spheroids and microtissues: Atp-based cell viability and toxicity assays. *Assay guidance manual [Internet]*, 2016.
- [126] Garrett W Roell, Jian Zha, Rhiannon R Carr, Mattheos A Koffas, Stephen S Fong, and Yinjie J Tang. Engineering microbial consortia by division of labor. *Microbial cell factories*, 18(1):1–11, 2019.
- [127] Finn Stirling, Lisa Bitzan, Samuel O’Keefe, Elizabeth Redfield, John WK Oliver, Jeffrey Way, and Pamela A Silver. Rational design of evolutionarily stable microbial kill switches. *Molecular cell*, 68(4):686–697, 2017.
- [128] Paul V Dunlap and EP Greenberg. Control of *vibrio fischeri* lux gene transcription by a cyclic amp receptor protein-luxr protein regulatory circuit. *Journal of bacteriology*, 170(9):4040–4046, 1988.
- [129] Domitilla Del Vecchio, Yili Qian, Richard M Murray, and Eduardo D Sontag. Future systems and control research in synthetic biology. *Annual Reviews in Control*, 45:5–17, 2018.
- [130] Catherine R Armbruster, Calvin K Lee, Jessica Parker-Gilham, Jaime de Anda, Aiguo Xia, Kun Zhao, Keiji Murakami, Boo Shan Tseng, Lucas R Hoffman, Fan Jin, et al. Heterogeneity in surface sensing suggests a division of labor in *pseudomonas aeruginosa* populations. *Elife*, 8:e45084, 2019.

- [131] Leila M Reyes Ruiz, Caitlin L Williams, and Rita Tamayo. Enhancing bacterial survival through phenotypic heterogeneity. *PLoS Pathogens*, 16(5):e1008439, 2020.
- [132] Jessica Grote, Dagmar Krysciak, and Wolfgang R Streit. Phenotypic heterogeneity, a phenomenon that may explain why quorum sensing does not always result in truly homogenous cell behavior. *Applied and environmental microbiology*, 81(16):5280–5289, 2015.
- [133] Ard Jan Grimbergen, Jeroen Siebring, Ana Solopova, and Oscar P Kuipers. Microbial bet-hedging: the power of being different. *Current opinion in microbiology*, 25:67–72, 2015.
- [134] Isabella Tomanek, Rok Grah, M Lagator, AMC Andersson, Jonathan P Bollback, Gašper Tkačik, and Calin C Guet. Gene amplification as a form of population-level gene expression regulation. *Nature ecology & evolution*, 4(4):612–625, 2020.
- [135] Mark S Aronson, Chiara Ricci-Tam, Xinwen Zhu, and Allyson E Sgro. Exploiting noise to engineer adaptability in synthetic multicellular systems. *Current Opinion in Biomedical Engineering*, 16:52–60, 2020.
- [136] Roy D Dar and Ron Weiss. Perspective: Engineering noise in biological systems towards predictive stochastic design. *APL bioengineering*, 2(2):020901, 2018.
- [137] Joshua T Kittleson, Sherine Cheung, and JChristopher Anderson. Rapid optimization of gene dosage in e. coli using dial strains. *Journal of biological engineering*, 5(1):1–7, 2011.
- [138] Miles V Rouches, Yasu Xu, Louis Brian Georges Cortes, and Guillaume Lambert. A plasmid system with tunable copy number. *Nature communications*, 13(1):1–12, 2022.
- [139] Shivang Hina-Nilesh Joshi, Chentao Yong, and Andras Gyorgy. Inducible plasmid copy number control for synthetic biology in commonly used e. coli strains. *Nature communications*, 13(1):6691, 2022.
- [140] Chenyi Li, Yusong Zou, Tian Jiang, Jianli Zhang, and Yajun Yan. Harnessing plasmid replication mechanism to enable dynamic control of gene copy in bacteria. *Metabolic engineering*, 70:67–78, 2022.
- [141] Gloria Del Solar and Manuel Espinosa. Plasmid copy number control: an ever-growing story. *Molecular microbiology*, 37(3):492–500, 2000.
- [142] Manel Camps. Modulation of cole1-like plasmid replication for recombinant gene expression. *Recent Patents on DNA & Gene Sequences (Discontinued)*, 4(1):58–73, 2010.
- [143] Nileena Velappan, Daniele Sblattero, Leslie Chasteen, Peter Pavlik, and Andrew RM Bradbury. Plasmid incompatibility: more compatible than previously thought? *Protein Engineering, Design and Selection*, 20(7):309–313, 2007.

- [144] Billy TC Lau, Per Malkus, and Johan Paulsson. New quantitative methods for measuring plasmid loss rates reveal unexpected stability. *Plasmid*, 70(3):353–361, 2013.
- [145] Matt Eames and Tanja Kortemme. Cost-benefit tradeoffs in engineered lac operons. *Science*, 336(6083):911–915, 2012.
- [146] Andrew Lezia, Nicholas Csicsery, and Jeff Hasty. Design, mutate, screen: Multiplexed creation and arrayed screening of synchronized genetic clocks. *Cell Systems*, 13(5):365–375, 2022.
- [147] Pallavi Penumetcha, Kin Lau, Xiao Zhu, Kelly Davis, Todd T Eckdahl, and A Malcolm Campbell. Improving the lac system for synthetic biology. *Bios*, 81(1):7–15, 2010.
- [148] Arianna Miano, Michael J Liao, and Jeff Hasty. Inducible cell-to-cell signaling for tunable dynamics in microbial communities. *Nature communications*, 11(1):1–8, 2020.
- [149] Christine A Miller and Stanley N Cohen. The partition (par) locus of psc101 is an enhancer of plasmid incompatibility. *Molecular microbiology*, 9(4):695–702, 1993.
- [150] Erez Dekel and Uri Alon. Optimality and evolutionary tuning of the expression level of a protein. *Nature*, 436(7050):588–592, 2005.
- [151] Jin Yang, Jihwan Lee, Michelle A Land, Shujuan Lai, Oleg A Igoshin, and François St-Pierre. A synthetic circuit for buffering gene dosage variation between individual mammalian cells. *Nature communications*, 12(1):4132, 2021.
- [152] Richard P Novick. Plasmid incompatibility. *Microbiological reviews*, 51(4):381–395, 1987.
- [153] Richard P Novick, Royston C Clowes, Stanley N Cohen, R Curtiss 3rd, Naomi Datta, and Stanley Falkow. Uniform nomenclature for bacterial plasmids: a proposal. *Bacteriological reviews*, 40(1):168–189, 1976.
- [154] José Carlos Ramón Hernández-Beltrán, Alvaro San Millán, Ayari Fuentes-Hernández, and Rafael Peña-Miller. Mathematical models of plasmid population dynamics. *Frontiers in Microbiology*, page 3389, 2021.
- [155] Kazushige Ishii, Tamotsu Hashimoto-Gotoh, and Kenichi Matsubara. Random replication and random assortment model for plasmid incompatibility in bacteria. *Plasmid*, 1(4):435–445, 1978.
- [156] Evangelos-Marios Nikolados, Andrea Y Weiße, and Diego A Oyarzún. Prediction of cellular burden with host–circuit models. *Synthetic Gene Circuits: Methods and Protocols*, pages 267–291, 2021.
- [157] Johannes AH Maier, Raphael Möhrle, and Albert Jeltsch. Design of synthetic epigenetic circuits featuring memory effects and reversible switching based on dna methylation. *Nature communications*, 8(1):15336, 2017.

- [158] Lieselotte Vermeersch, Lloyd Cool, Anton Gorkovskiy, Karin Voordeckers, Tom Wenseleers, and Kevin J Verstrepen. Do microbes have a memory? history-dependent behavior in the adaptation to variable environments. *Frontiers in Microbiology*, 13:4052, 2022.
- [159] Samuel O Skinner, Leonardo A Sepúlveda, Heng Xu, and Ido Golding. Measuring mrna copy number in individual escherichia coli cells using single-molecule fluorescent in situ hybridization. *Nature protocols*, 8(6):1100–1113, 2013.
- [160] Y. Arita, G. Kim, Z. Li, H. Friesen, G. Turco, R. Y. Wang, D. Climie, M. Usaj, M. Hotz, E. H. Stoops, et al. A genome-scale yeast library with inducible expression of individual genes. *Molecular Systems Biology*, 17(6):e10207, 2021.
- [161] B. A. Blount, T. Weenink, and T. Ellis. Construction of synthetic regulatory networks in yeast. *FEBS letters*, 586(15):2112–2121, 2012.
- [162] T. S. Moon, C. Lou, A. Tamsir, B. C. Stanton, and C. A. Voigt. Genetic programs constructed from layered logic gates in single cells. *Nature*, 491(7423):249–253, 2012.
- [163] H. Redden, N. Morse, and H. S. Alper. The synthetic biology toolbox for tuning gene expression in yeast. *FEMS Yeast Research*, 15(1):fov012, 2015.
- [164] M. Tominaga, K. Nozaki, D. Umeno, J. Ishii, and A. Kondo. Robust and flexible platform for directed evolution of yeast genetic switches. *Nature Communications*, 12(1):1846, 2021.
- [165] Y. Chen, S. Zhang, E. M. Young, T. S. Jones, D. Densmore, and C. A. Voigt. Genetic circuit design automation for yeast. *Nat Microbiol*, 5(11):1349–1360, 2020.
- [166] S. Ikushima and J. D. Boeke. New orthogonal transcriptional switches derived from tet repressor homologues for saccharomyces cerevisiae regulated by 2,4-diacetylphloroglucinol and other ligands. *ACS Synth Biol*, 6(3):497–506, 2017.
- [167] A. Aranda-Diaz, K. Mace, I. Zuleta, P. Harrigan, and H. El-Samad. Robust synthetic circuits for two-dimensional control of gene expression in yeast. *ACS Synth Biol*, 6(3):545–554, 2017.
- [168] R. S. McIsaac, B. L. Oakes, X. Wang, K. A. Dummit, D. Botstein, and M. B. Noyes. Synthetic gene expression perturbation systems with rapid, tunable, single-gene specificity in yeast. *Nucleic Acids Res*, 41(4):e57, 2013.
- [169] R. S. McIsaac, S. J. Silverman, M. N. McClean, P. A. Gibney, J. Macinskas, M. J. Hickman, A. A. Petti, and D. Botstein. Fast-acting and nearly gratuitous induction of gene expression and protein depletion in saccharomyces cerevisiae. *Mol Biol Cell*, 22(22):4447–4459, 2011.
- [170] Edward Giniger, Susan M Varnum, and Mark Ptashne. Specific dna binding of gal4, a positive regulatory protein of yeast. *Cell*, 40(4):767–774, 1985.

- [171] Simon Labbe and Dennis J Thiele. Copper ion inducible and repressible promoter systems in yeast. *Methods Enzymol*, 306:145–153, 1999.
- [172] Elke Nevoigt, Janine Kohnke, Christopher R Fischer, Hal Alper, Ulf Stahl, and Gregory Stephanopoulos. Engineering of promoter replacement cassettes for fine-tuning of gene expression in *saccharomyces cerevisiae*. *Appl Environ Microbiol*, 72(8):5266–5273, 2006.
- [173] Gilles Charvin, Frederick RM Cross, and Eric D Siggia. A microfluidic device for temporally controlled gene expression and long-term fluorescent imaging in unperturbed dividing yeast cells. *PLoS One*, 3(1):e1468, 2008.
- [174] Ulrich Deuschle, R Stephen Hipskind, and Hermann Bujard. Rna polymerase ii transcription blocked by *escherichia coli* lac repressor. *Science*, 248(4954):480–483, 1990.
- [175] Bryn C Stanton, Vincenzo Siciliano, Amar Ghodasara, Liliana Wroblewska, Kevin Clancy, Axel C Trefzer, Jonathan D Chesnut, Ron Weiss, and Christopher A Voigt. Systematic transfer of prokaryotic sensors and circuits to mammalian cells. *ACS Synth Biol*, 3(12):880–891, 2014.
- [176] A.T. Das, L. Tenenbaum, and B. Berkhout. Tet-on systems for doxycycline-inducible gene expression. *Curr Gene Ther*, 16(3):156–167, 2016.
- [177] M. Gossen and H. Bujard. Tight control of gene expression in mammalian cells by tetracycline-responsive promoters. *Proc Natl Acad Sci U S A*, 89(12):5547–5551, 1992.
- [178] M. Gossen, S. Freundlieb, G. Bender, G. Muller, W. Hillen, and H. Bujard. Transcriptional activation by tetracyclines in mammalian cells. *Science*, 268(5218):1766–1769, 1995.
- [179] J.F. Louvion, B. Havaux-Copf, and D. Picard. Fusion of gal4-vp16 to a steroid-binding domain provides a tool for gratuitous induction of galactose-responsive genes in yeast. *Gene*, 131(1):129–134, 1993.
- [180] William M Shaw, Hitoshi Yamauchi, Jack Mead, Glen-Oliver F Gowers, David J Bell, David Öling, Niklas Larsson, Mark Wigglesworth, Graham Ladds, and Tom Ellis. Engineering a model cell for rational tuning of gpcr signaling. *Cell*, 177(3):782–796, 2019.
- [181] C.J. Bashor, N. Patel, S. Choubey, A. Beyzavi, J. Kondev, J.J. Collins, and A.S. Khalil. Complex signal processing in synthetic gene circuits using cooperative regulatory assemblies. *Science*, 364(6440):593–597, 2019.
- [182] Guoping Ren, Aijing Ma, Weijie Liu, Xiaohong Zhuang, and Guoqiang Zhuang. Bacterial signals n-acyl homoserine lactones induce the changes of morphology and ethanol tolerance in *saccharomyces cerevisiae*. *AMB Express*, 6(1):117, 2016.
- [183] Dominik M Troppens, Ruslan I Dmitriev, Dmitry B Papkovsky, Fergal O’Gara, and John P Morrissey. Genome-wide investigation of cellular targets and mode of action of the antifungal bacterial metabolite 2,4-diacetylphloroglucinol in *saccharomyces cerevisiae*. *FEMS yeast research*, 13(3):322–334, 2013.

- [184] Norman Moullan, Laurent Mouchiroud, Xiaoling Wang, Dongryeol Ryu, Evan G Williams, Adrienne Mottis, Virginija Jovaisaite, Michael V Frochoux, Pedro M Quiros, Bart Deplancke, et al. Tetracyclines disturb mitochondrial function across eukaryotic models: A call for caution in biomedical research. *Cell reports*, 10(10):1681–1691, 2015.
- [185] Kimberly J Regehr, Mireia Domenech, Joel T Koepsel, Kyle C Carver, Spencer J Ellison-Zelski, William L Murphy, Linda A Schuler, Elizabeth T Alarid, and David J Beebe. Biological implications of polydimethylsiloxane-based microfluidic cell culture. *Lab on a Chip*, 9(15):2132–2139, 2009.
- [186] Adam J Meyer, Thomas H Segall-Shapiro, Emma Glassey, Jun Zhang, and Christopher A Voigt. *Escherichia coli* "marionette" strains with 12 highly optimized small-molecule sensors. *Nature chemical biology*, 15(2):196–204, 2019.
- [187] Drew Endy. Foundations for engineering biology. *Nature*, 438(7067):449–453, 2005.
- [188] Ming Ming Chang, Leonid Gaidukov, George Jung, Wei-An Tseng, John J Scarcelli, Rachel Cornell, Jason K Marshall, Jared L Lyles, Paul Sakorafas, Angela A Chu, et al. Small-molecule control of antibody n-glycosylation in engineered mammalian cells. *Nature chemical biology*, 15(7):730–736, 2019.
- [189] Dharendra V Israni, Hongxia Li, Keith A Gagnon, Jeffrey D Sander, Kole T Roybal, J Keith Joung, Wing Hung Wong, and Ahmad S Khalil. Clinically-driven design of synthetic gene regulatory programs in human cells. *bioRxiv*, 2021.
- [190] Yinqing Gao, Xiong Xiong, Spencer Wong, Eliza J Charles, Wendell A Lim, and Lei S Qi. Complex transcriptional modulation with orthogonal and inducible *dcas9* regulators. *Nature methods*, 13(12):1043–1049, 2016.
- [191] Daniel Bojar, Leo Scheller, Ghislaine Charpin-El Hamri, Mingqi Xie, and Martin Fussenegger. Caffeine-inducible gene switches controlling experimental diabetes. *Nature communications*, 9(1):2318, 2018.
- [192] Patrick S Donahue, Jessica W Draut, John J Muldoon, Heather I Edelstein, Neda Bagheri, and Joshua N Leonard. The comet toolkit for composing customizable genetic programs in mammalian cells. *Nature communications*, 11(1):779, 2020.
- [193] Elizabeth P Tague, Heather L Dotson, Shane N Tunney, David C Sloas, and John T Ngo. Chemogenetic control of gene expression and cell signaling with antiviral drugs. *Nature Methods*, 15(7):519–522, 2018.
- [194] Volker Wanke, Elisabetta Cameroni, Airi Uotila, Marco Piccolis, Jiri Urban, Robbie Loewith, and Claudio De Virgilio. Caffeine extends yeast lifespan by targeting *torc1*. *Molecular Microbiology*, 69(1):277–285, 2008.

- [195] Ian J Roney, Adam D Rudner, Jean-Francois Couture, and Mads Kaern. Improvement of the reverse tetracycline transactivator by single amino acid substitutions that reduce leaky target gene expression to undetectable levels. *Scientific Reports*, 6:27697, 2016.
- [196] Stefanie Urlinger, Ulrich Baron, Matthias Thellmann, Mazhar T Hasan, Hermann Bujard, and Wolfgang Hillen. Exploring the sequence space for tetracycline-dependent transcriptional activators: novel mutations yield expanded range and sensitivity. *Proceedings of the National Academy of Sciences*, 97(14):7963–7968, 2000.
- [197] AT Das, X Zhou, M Vink, B Klaver, K Verhoef, G Marzio, and B Berkhout. Viral evolution as a tool to improve the tetracycline-regulated gene expression system. *Journal of Biological Chemistry*, 279(18):18776–18782, 2004.
- [198] Xiaozhong Zhou, Martin Vink, Bauke Klaver, Ben Berkhout, and Atze T Das. Optimization of the tet-on system for regulated gene expression through viral evolution. *Gene therapy*, 13(19):1382–1390, 2006.
- [199] Yunfei Li, Yi Jiang, Jonathan Paxman, Ryan O’Laughlin, Steven Klepin, Yuelin Zhu, Lorraine Pillus, Lev S Tsimring, Jeff Hasty, and Nan Hao. A programmable fate decision landscape underlies single-cell aging in yeast. *Science*, 369(6501):325–329, 2020.
- [200] Albert W Cheng, Hui Wang, Haoquan Yang, Lei Shi, Yonatan Katz, Thorold W Theunissen, Shaam Rangarajan, Chikdu S Shivalila, David B Dadon, and Rudolf Jaenisch. Multiplexed activation of endogenous genes by crispr-on, an rna-guided transcriptional activator system. *Cell research*, 23(10):1163–1171, 2013.
- [201] Adrian L Sanborn, Benjamin T Yeh, Jason T Feigerle, Chenling V Hao, Ryan J Townshend, Erez Lieberman Aiden, Ron O Dror, and Roger D Kornberg. Simple biochemical features underlie transcriptional activation domain diversity and dynamic, fuzzy binding to mediator. *eLife*, 10, 2021.
- [202] U. Baumgartner, B. Hamilton, M. Piskacek, H. Ruis, and H. Rottensteiner. Functional analysis of the zn(2)cys(6) transcription factors oaf1p and pip2p. different roles in fatty acid induction of beta-oxidation in *saccharomyces cerevisiae*. *J Biol Chem*, 274(32):22208–22216, 1999.
- [203] Simona Piskacek, Martin Gregor, Maria Nemethova, Martin Grabner, Pavel Kovarik, and Martin Piskacek. Nine-amino-acid transactivation domain: establishment and prediction utilities. *Genomics*, 89(6):756–768, 2007.
- [204] R. Bartenschlager, L. Ahlborn-Laake, J. Mous, and H. Jacobsen. Nonstructural protein 3 of the hepatitis c virus encodes a serine-type proteinase required for cleavage at the ns3/4 and ns4/5 junctions. *J Virol*, 67(7):3835–3844, 1993.
- [205] M. Z. Lin, J. S. Glenn, and R. Y. Tsien. A drug-controllable tag for visualizing newly synthesized proteins in cells and whole animals. *Proc Natl Acad Sci U S A*, 105(22):7744–7749, 2008.

- [206] H. K. Chung, C. L. Jacobs, Y. Huo, J. Yang, S. A. Krumm, R. K. Plemper, R. Y. Tsien, and M. Z. Lin. Tunable and reversible drug control of protein production via a self-excising degenon. *Nat Chem Biol*, 11(9):713–720, 2015.
- [207] Lu Xu, Peng Liu, Zhong Dai, Fei Fan, and Xi Zhang. Fine-tuning the expression of pathway gene in yeast using a regulatory library formed by fusing a synthetic minimal promoter with different kozak variants. *Microbial Cell Factories*, 20(1):148, 2021.
- [208] Markus Otto, Christos Skrekas, Manuel Gossing, Claes Gustafsson, Verena Siewers, and Florian David. Expansion of the yeast modular cloning toolkit for crispr-based applications, genomic integrations and combinatorial libraries. *ACS Synthetic Biology*, 10(12):3461–3474, 2021.
- [209] Janet M An-Adirekkun, C Neal Stewart, Spencer H Geller, Manali T Patel, Jose Melendez, Benjamin L Oakes, Marcus B Noyes, and Megan N McClean. A yeast optogenetic toolkit (yotk) for gene expression control in *saccharomyces cerevisiae*. *Biotechnology and bioengineering*, 117(3):886–893, 2020.
- [210] Arjun Khakhar, Nicholas J Bolten, Jennifer Nemhauser, and Eric Klavins. Cell-cell communication in yeast using auxin biosynthesis and auxin responsive crispr transcription factors. *ACS synthetic biology*, 5(4):279–286, 2016.
- [211] Xueliang John Gao, Shaorong Chong, Moonsoo Kim, and Michael B Elowitz. Programmable protein circuits in living cells. *Science*, 361(6408):1252–1258, 2018.
- [212] Christian Ritz, Florent Baty, Jens C Streibig, and Daniel Gerhard. Dose-response analysis using r. *PLoS ONE*, 10(12):e0146021, 2015.